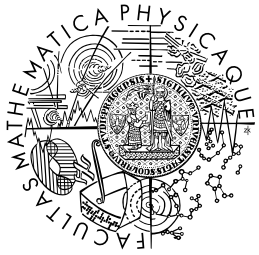

FACULTY
OF MATHEMATICS
AND PHYSICS
Charles University

MASTER THESIS

Bc. Emil Lelák

Study of jet suppression in heavy-ion collisions with the ATLAS experiment

Institute of Particle and Nuclear Physics

Supervisor of the master thesis: Mgr. Martin Rybář, PhD.
Study programme: Particle and Nuclear Physics
Study branch: Particle and Nuclear Physics

Prague 2024

I declare that I carried out this master thesis independently, and only with the cited sources, literature and other professional sources. It has not been used to obtain another or the same degree.

I understand that my work relates to the rights and obligations under the Act No. 121/2000 Sb., the Copyright Act, as amended, in particular the fact that the Charles University has the right to conclude a license agreement on the use of this work as a school work pursuant to Section 60 subsection 1 of the Copyright Act.

In ..... date ....

Author's signature

First of all, I would like to express gratitude to my supervisor, Martin Rybář, for his invaluable guidance, mentorship, patience, and time he devoted to me. Secondly, I thank Daniel Schreirich and Vojtěch Pleskot who showed me how to work on the computational cluster Chimera. I am also thankful to my professors from the IPNP who taught me skills that I utilized in this thesis. Last but not least, I am grateful to my family whose love and support have been my greatest strength.

Title: Study of jet suppression in heavy-ion collisions with the ATLAS experiment

Author: Bc. Emil Lelák

Institute: Institute of Particle and Nuclear Physics

Supervisor: Mgr. Martin Rybář, PhD., Institute of Particle and Nuclear Physics

Abstract: Ultra-relativistic heavy-ion collisions are performed to generate and examine QCD matter at high temperatures, known as the quark-gluon plasma. This extraordinary state of matter is theorized to have been present in the initial microseconds following the Big Bang. Exploring the quark-gluon plasma and the characteristics of the strong force involves analyzing particle showers, referred to as jets, originating from scattered quarks and gluons.
Recent results from the measurement of the suppression of jet production in dependence on jet size in lead-lead collisions with the ATLAS, ALICE, and CMS experiments are inconsistent with each other. The motivation for this thesis is to clarify the inconsistencies. The thesis deals with the systematical study of track-jet production as a function of their size and minimum transverse momentum of their constituents using data from the ATLAS experiment. The correlations between calorimetric and track jets are also investigated. Furthermore, the thesis includes the correction of track-jet spectra for various detector effects and background using Monte Carlo (MC) simulations (so-called bin-by-bin unfolding). The last part is the application of the Iterative Constituent Subtraction (ICS) method to subtract the background, which is dominated by soft (low-p_{T}) particles.
Even though the results of the thesis do not fully clarify the inconsistency between the experiments, they provide a certain degree of understanding of track-jet suppression in the QGP. Further analysis which would include better unfolding and parameter tuning within the ICS should help to clarify the inconsistency between the experiments.

Keywords: jet, jet quenching, CERN, ATLAS, LHC.

Názov práce: Štúdium potlačenia jetov v zrážkach ťažkých iónov na experimente ATLAS

Autor: Emil Lelák

Ústav: Ústav časticovej a jadrovej fyziky

Vedúci práce: Mgr. Martin Rybář, Ph.D., Ústav časticovej a jadrovej fyziky

Abstrakt: Ultra-relativistické zrážky ťažkých iónov sú vykonávané za účelom produkcie a štúdia QCD hmoty s vysokou teplotou, tzv. kvark-gluónovej plazmy. Predpokladá sa, že takýto extrémny stav hmoty existoval počas prvých mikrosekúnd po Veľkom tresku. Skúmanie vlastností kvark-gluónovej plazmy a silnej interakcie zahŕňa analýzu kolimovaných spŕšok častíc, tzv. jetov, ktoré pochádzajú z rozptýlených kvarkov a gluónov.
Nedávne výsledky z merania potlačenia jetov v závislosti na ich veľkosti v zrážkach olovo-olovo z experimentov ATLAS, ALICE a CMS sú vo vzájomnom nesúlade. Motiváciou tejto práce je objasniť nesúlad medzi výsledkami experimentov. Práca sa zaoberá systematickým štúdiom produkcie jetov konštruovaných z nabitých častíc v závislosti na veľkosti jetov a výbere nabitých častíc podľa ich priečnej hybnosti. Tieto jety sú tiež porovnávané s kalorimetrickými jetmi. Ďalej práca zahŕňa opravu spektier jetov konštruovaných z nabitých častíc o rôzne detektorové efekty a efekty pozadia pomocou Monte Carlo simulácií (tzv. bin-by-bin unfolding). Poslednou časťou je aplikácia tzv. Iterative Constituent Subtraction (ICS) metódy na odčítavanie pozadia, ktoré je dominované časticami s nízkou priečnou hybnosťou.
Napriek tomu, že z výsledkov práce nemožno celkom objasniť nesúlad medzi výsledkami experimentov, práca vykazuje určitý stupeň pochopenia potlačenia jetov konštruovaných z nabitých častíc v kvark-gluónovej plazme. Ďalšia analýza, ktorá by zahŕňala lepší unfolding a ladenie parametrov v ICS metóde, by mohla pomôcť k objasneniu nesúladu medzi výsledkami experimentov.

Kľúčové slová: jet, jet quenching, CERN, ATLAS, LHC.

Contents

Introduction

The main purpose of heavy-ion (HI) physics is to study QCD matter, called quark-gluon plasma (QGP) [1]. It can be produced at the Large Hadron Collider (LHC) in CERN when two ultra-relativistic heavy ions are collided. The QGP can be probed via collimated sprays of particles, referred to as jets. Jets are produced in both proton-proton (pp) and HI collisions. Whereas the jets created in pp collisions are not suppressed, in HI collisions they are. The explanation is that when jets penetrate through the QGP, which is the case of HI collisions, they interact with the matter, lose energy, and therefore are suppressed. Thanks to the jet suppression it is possible to probe QGP properties.

One of the purposes of the ATLAS, ALICE, and CMS experiments at the LHC is to study QGP. The recent results on the suppression of jet production in dependence on their size in lead-lead (PbPb) collisions from these experiments [2, 3, 4, 5] are inconsistent with each other. However, the measurements in the individual experiments were not performed in the same conditions. They differ in collision energy, quantity that describes jet suppression, jet constituents, and method for background subtraction. It seems that different collision energies at such high scales and different quantities that describe jet suppression do not play an important role in the results. Probably the most important fact is that jet constituents within ALICE are tracks, while the other experiments used calorimetric information for clustering. To remove this difference, track-jet spectra are constructed from ATLAS data within this thesis. It is the first time when the track jets are studied within the ATLAS experiment in more detail. As to different methods for background subtraction, ATLAS and CMS used a standard area-based method, while ALICE used a machine-learning-based (ML-based) method which allows to perform the analysis at lower transverse momentum p_{T}. On the other hand, the ML-based method implies larger systematic errors in the results.

In my data analysis, there appear some difficulties. The raw data include various unwanted detector effects, such as imperfect tracking efficiency and momentum resolution of the detector, and background dominated by soft particles (the raw data are folded), so some unfolding procedures must be applied to the data. All these effects can be seen in MC simulations, where one can investigate correlations between the reconstructed and truth jets. Within this thesis, a simple bin-by-bin unfolding is applied to the raw experimental data using the MC simulations. However, such a simple unfolding is the very first attempt to correct data, since it corrects them for a lot of effects simultaneously.

Since the background consists of soft particles, it can be removed by setting the minimum transverse momentum of clustered tracks $p_{\mathrm{T}}^{\mathrm{cut}}$. However, the low-energetic signals are also discarded along with the background, which means "bias of physics". Another possibility how to treat background is to use a method for background subtraction. Within this thesis, the ICS method is used. However, this method involves a couple of free parameters and it is challenging to find their optimal values.

1. Experimental Setup

1.1 The Large Hadron Collider

The Large Hadron Collider (LHC) [6] is the biggest and most powerful particle accelerator in the world. It is the last part of CERN's accelerator complex (see Fig.1.1). In each part of the complex, the energy of particles gradually increases. No accelerator in the world can give particles such high energy as the LHC.

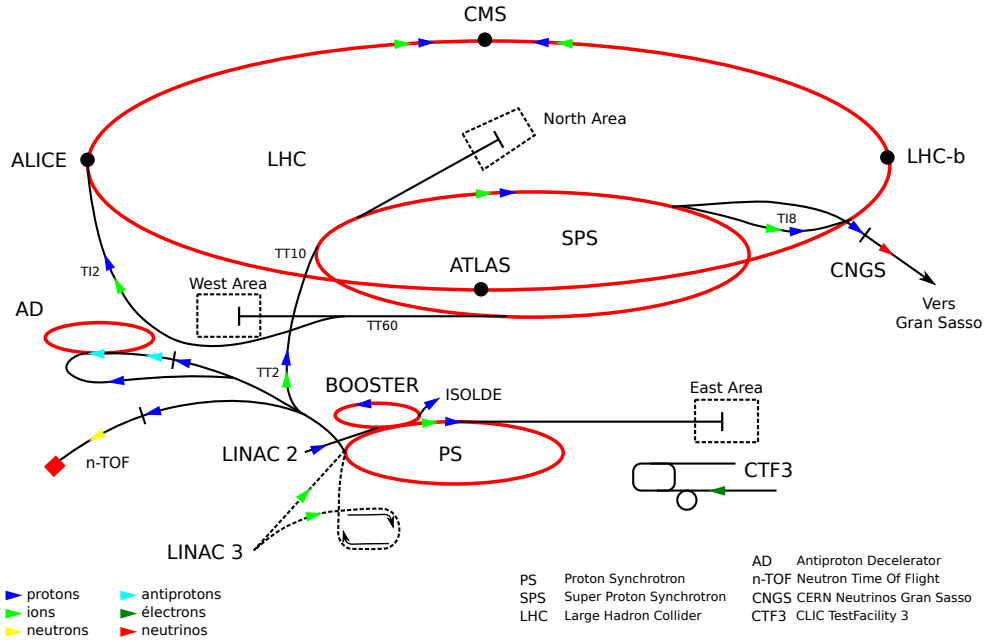

Figure 1.1: The CERN's accelerator complex. Taken from [7].

The LHC is a circular accelerator with a circumference of 27 km. It accelerates and bands charged particles using electromagnetic devices. The main devices are radiofrequency (RF) cavities boosting the particles, and magnets, which keep the particles on circular trajectories and squeeze them at so-called interaction points, where are head-on collided. There are four interaction points at the LHC corresponding to four big experiments: ATLAS, ALICE, CMS, and LHCb.

RF cavities are a little discussed in this paragraph. The RF cavities are metallic chambers containing an electromagnetic field, which give the particles an electrical impulse and accelerate them. The LHC contains 16 RF cavities placed in four cylindrical refrigerators called cryomodules that enable them to work in a superconducting state. Particle acceleration is based on the change of field polarity in the cavities when the particles pass through them. The change of field polarity is given by a frequency of 40 MHz. For this reason, the particles are sorted into bunches[1] with spacing 25 ns. The LHC cavities bring protons from the energy of 450 GeV to 6.5 TeV. At this energy, protons go around the LHC approximately 11 thousand times [6].

[1]Each proton beam contains about 3000 bunches and there are about 10^{11} protons in each bunch.

The LHC contains more than 50 types of electromagnets. Dipole magnets are used to bend the paths of the particles. The main dipoles generate a very strong magnetic field of 8.3 T. For such a strong magnetic field, the electromagnets use a current of 11 kA, so superconducting coils are used to avoid big energy losses. The LHC is also equipped with the magnets of higher multipolarity. The quadrupole magnets help to keep the particles in a tight beam. Four magnetic poles are placed symmetrically around the beam pipe and squeeze the beam horizontally and vertically. There are also inner quadrupole triplets at interaction points, which make the beams 12.5 times thinner, and the probability of the collision is increased. The sextupole, octupole, and decapole magnets correct the magnetic field for small imperfections and the extremities of the dipoles.

As to the type of particles, the LHC accelerates not only protons but also lead nuclei $^{208}_{82}$Pb. A particle collision is characterized by collision energy (center-of-mass energy) $\sqrt{s}$,

$$\sqrt{s} = \sqrt{(E_1 + E_2)^2 - (\mathbf{p}_1 + \mathbf{p}_2)^2}, \tag{1.1}$$

where E_1, E_2 are the energies and $\mathbf{p}_1$, $\mathbf{p}_2$ are the momenta of the first and the second particle, respectively. If the particles of the same type with the same energy are head-on collided, then $\sqrt{s} = 2E$. If the collided particles are heavy ions, the collision energy is rather expressed per nucleon and is denoted $\sqrt{s_{\mathrm{NN}}}$. The maximal collision energy of protons at LHC is $\sqrt{s} = 13.6$ TeV, whereas for lead nuclei[2] $\sqrt{s_{\mathrm{NN}}} = 5.36$ TeV.

An important quantity that characterizes the performance of an accelerator is luminosity. Luminosity expresses how many beam particles it is possible to squeeze through a given space in a given time. The conversion between luminosity L and collision rate N_{col} is through the cross-section of the collision σ,

$$N_{\mathrm{col}} = \sigma L. \tag{1.2}$$

The luminosity of the LHC for protons is about 10^{34} cm^{-2}.s^{-1} and for heavy ions it is in the order of 10^{27} cm^{-2}.s^{-1}. The rate of pp collisions is approximately 10^{12} s^{-1} [6] and the rate of inelastic PbPb collisions is about 50 kHz.

1.2 The ATLAS Detector

ATLAS (A Toroidal LHC ApparatuS) [8] is a general-purpose detector designed to investigate a wide range of physics, from the Higgs boson to extra dimensions and particles that could make up dark matter. The ATLAS detector is the largest particle detector ever built. It is 46 m long, 25 m high, 25 m wide and its mass is approximately seven thousand tonnes.

1.2.1 ATLAS Coordinate System and Kinematics

ATLAS coordinate system (see Fig. 1.2) is introduced in this part. The center of the coordinate system is at the interaction point. The z-axis has the direction of

[2] A lead nucleus consists of 82 protons and 126 neutrons (208 nucleons). Maximal collision energy in pp collisions is 13.6 TeV, so in PbPb collisions, $\sqrt{s_{\mathrm{NN}}} = (82/208) \times 13.6$ TeV $\approx$ 5.36 TeV.

the beam pipe, the x-axis directs to the center of the LHC ring, and the y-axis upwards. Polar angle θ is the angle between a given vector and the z-axis, and azimuthal angle ϕ is the angle between the projection of the given vector to the x-y plane and the x-axis.

Important kinematic quantities are the projections of momentum and energy to the x-y plane, referred to as transverse momentum p_{T} and transverse energy E_{T}, which are given by the formula

$$\begin{aligned} p_{\mathrm{T}} &= p \sin\theta, \\ E_{\mathrm{T}} &= E \sin\theta. \end{aligned} \tag{1.3}$$

The great advantage of transverse quantities is that they are invariant under Lorentz boost along the z-axis.

Another important quantities are rapidity y and pseudorapidity η. They can be expressed as

$$\begin{aligned} y &= \frac{1}{2} \ln\left(\frac{E + p\cos\theta}{E - p\cos\theta}\right), \\ \eta &= -\ln\left(\tan\frac{\theta}{2}\right). \end{aligned} \tag{1.4}$$

One can see that η depends only on θ, and is obtained from rapidity in the limit case $E \approx p$.

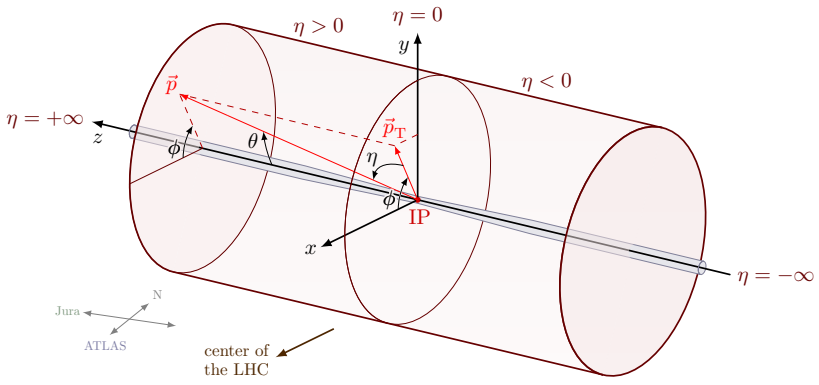

Figure 1.2: ATLAS coordinate system. Taken from [9].

1.2.2 ATLAS Subdetectors

The ATLAS detector [10] consists of three main subdetectors: the Inner Detector, the calorimeter, and the Muon Spectrometer. All of these subdetectors are discussed in the following paragraphs.

Inner Detector

The Inner Detector (ID) is the innermost part of the ATLAS detector. The ID measures properties of electrically charged particles only – their charge, direction,

and momentum. The ID's diameter is 2.1 m and its length is 6.2 m. The detector can measure the tracks with pseudorapidity $|\eta| < 2.5$. It consists of three different systems of sensors all immersed in a solenoidal magnetic field of magnitude 2 T parallel to the beam axis: Pixel Detector, Semiconductor Tracker (SCT), and Transition Radiation Tracker (TRT). The structure of the ID is shown in Fig. 1.3.

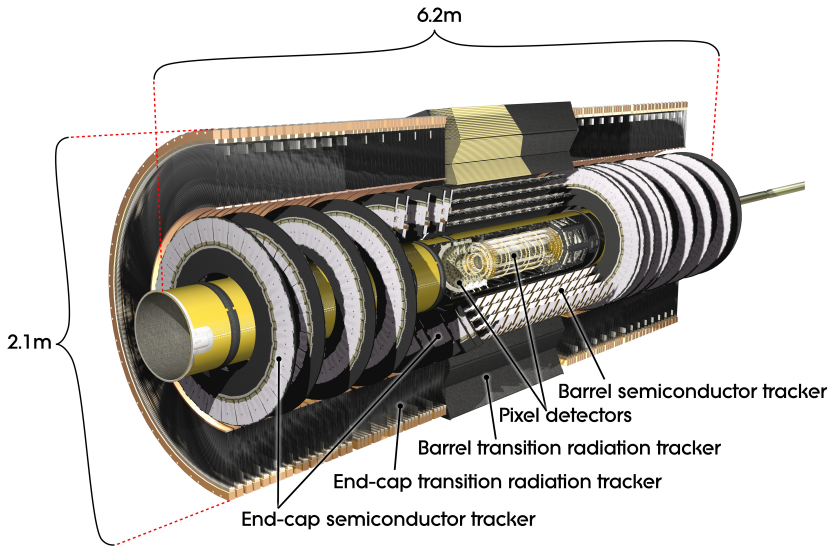

Figure 1.3: Scheme of the Inner Detector. Taken from [10].

The Pixel Detector is the first point of detection in the ATLAS experiment. It consists of four layers of silicon pixels. Charged particles leave a small amount of energy in the Pixel Detector that is converted to signal. The signal is used to determine the origin and momentum of the particle. The Pixel Detector contains over 92 million pixels and almost 2000 detector elements.

The SCT surrounds the Pixel Detector and it is used for the track reconstruction. It contains over 4000 modules of 6 million double-sided micro-strips of silicon sensors. It is designed in a way that a particle crosses through at least four silicon layers, which enables the measurement of particle tracks with a precision of up to 25 μm.

The outermost part of the Inner Detector is the TRT. It contains three hundred thousand straws filled with a gas mixture. Passing particles ionize the gas and create an electric signal that is used to reconstruct their tracks and get information about the particle type [10].

Calorimeter

The ATLAS Calorimeter is the next part of the ATLAS Detector. It measures the energy of electrons, photons, and hadrons. Most of all these particles are stopped there. The ATLAS Calorimeter consists of two calorimeters: the Liquid Argon (LAr) Calorimeter and the Tile Hadronic Calorimeter. The scheme of the ATLAS Calorimeter is introduced in Fig. 1.4. The pseudorapidity range of the calorimeter is $|\eta| < 4.9$.

The LAr Calorimeter contains both electromagnetic and hadronic calorimeters. It incorporates multiple layers of metal, such as tungsten, copper, or lead,

designed to absorb incoming particles and transform them into a cascade of new particles with lower energy. Within these layers, liquid argon is sandwiched and gets ionized by the produced particles, generating an electric current that can be quantified. By gathering the measured currents, physicists can ascertain the energy of the initial particle that interacted with the detector. To keep the argon in liquid form, the LAr Calorimeter is kept at -184°C.

In addition, it is important to mention that the LAr Forward Calorimeter (FCal, see Fig. 1.4) is used to determine the centrality of a PbPb collision by measuring the total transverse energy E_{T} from the collision. The concept of centrality is introduced in Sec. 2.2. The pseudorapidity range of the FCal is $3.1 < |\eta| < 4.9$.

The Tile Calorimeter surrounds the LAr Calorimeter and provides the calorimetry of hadrons in the range $|\eta| < 1.7$. It is composed of steel layers and plastic scintillating tiles. When particles hit the steel layers, they create a cascade of new particles. Subsequently, the plastic scintillators emit photons, which are then transformed into an electric current. The intensity of this current is directly proportional to the energy of the initial particle.

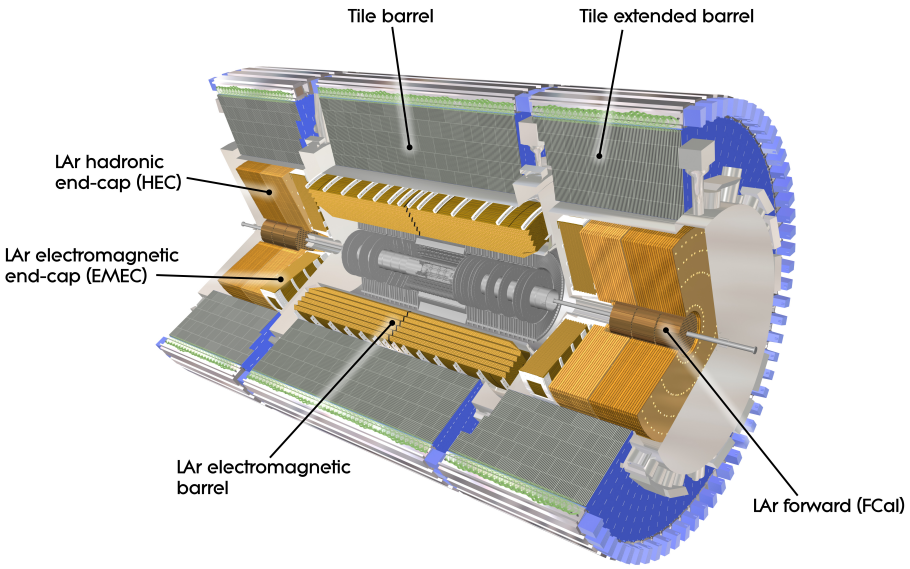

Figure 1.4: Scheme of the ATLAS Calorimeter. Taken from [10].

Muon Spectrometer

The outermost part of the ATLAS Detector is the Muon Spectrometer, which identifies and measures the momenta of muons. Five different detector technologies are used: Thin Gap Chambers, Resistive Plate Chambers, Monitored Drift Tubes, Small-Strip Thin-Gap Chambers, and Micromegas. However, these technologies will not be discussed in more detail in this thesis. More information about these technologies can be found here [10].

1.2.3 Magnet System

The measurement of the charge and momentum of charged particles requires a magnetic field. ATLAS Detector uses two magnet systems – solenoidal and toroidal. These systems create a strong magnetic field, which requires high electric current. For this reason, they are cooled to about 4.5 K. The main parts of the magnet system are: Central Solenoid Magnet, Barrel Toroid, and End-cap Toroids. The Central Solenoid Magnet envelops the ID and provides a magnetic field of magnitude 2 T. Toroid magnets generate a magnetic field of up to 3.5 T and they are used to measure the momenta of muons. The Barrel Toroid surrounds the center of the experiment and two end-cap toroids are at the ends of the experiment [10].

1.2.4 Trigger System

At ATLAS, beam collisions occur at a frequency of 40 MHz. Handling and storing the resulting data at this scale poses significant challenges. Furthermore, many of the recorded events involve processes that have already been studied and understood. Thus, it becomes imperative to selectively prioritize the recording of events that align with our research interests.

The ATLAS detector has a two-level trigger system [11]. The Level-1 (L1) trigger is the initial stage of event selection implemented in hardware. It utilizes a subset of detector information to limit the acceptance rate of events from a maximum input rate of 40 MHz to no more than 100 kHz. It can identify jets, electrons, photons, muons, and some event properties as the total (missing) transverse energy E_{T}.

Subsequently, a software-driven trigger known as the high-level trigger (HLT) further reduces the rate of recorded events. On average, a few kHz of events are stored for subsequent physics analysis. The HLT selectively reconstructs objects such as leptons or jets based on specific L1 triggers that have endorsed the event for further processing. Some examples of L1 and HLT triggers used in pp and PbPb collisions are introduced in Sec. 3.3 or in [11].

2. Physics Background

2.1 Introduction to Quantum Chromodynamics

The main purpose of heavy-ion physics is to study quantum chromodynamics (QCD) at extremely high temperatures [1]. QCD is a theory of strong force and the main properties of the QCD are color confinement and asymptotic freedom [12].

Color confinement means that particles carrying color charge (quarks and gluons) cannot exist separately at normal conditions, so quarks and gluons (together so-called partons) are bound in composite particles – hadrons. It is a consequence of the fact, that the further the partons are from each other, the stronger they attract each other. The phenomenological potential of strong interaction between two partons is given by the formula

$$V_{\mathrm{S}}(r) = -\frac{4}{3}\frac{\alpha_{\mathrm{S}}}{r} + kr, \tag{2.1}$$

where r is a distance between the partons, α_{S} is a strong coupling constant and k is the color string tension.

However, at sufficiently high temperatures and densities, the partons can be deconfined. This phenomenon is called asymptotic freedom. The matter where partons are deconfined is called quark-gluon plasma (QGP). Asymptotic freedom is the consequence of the fact that strong coupling α_{S} depends on transferred momentum Q^2 and can be expressed as

$$\alpha_{\mathrm{S}}(Q^2) \approx \frac{12\pi}{(33 - 2N_f)\ln\frac{Q^2}{\Lambda^2}}, \tag{2.2}$$

where $\Lambda \approx 200$ MeV is the momentum scale at which the perturbation calculation is meaningless, and N_f is the number of quark flavors that can be created in such interaction. One can see that for big values of Q the strong coupling is very small. The QCD theory is discussed in more detail in [12].

2.2 Concept of Centrality

An important property of a HI collision is the centrality of the collision. It is a quantity that describes a degree of heavy ions overlap. Centrality is directly connected to an impact parameter, denoted b, which is a transversal distance between the centers of colliding nuclei. One can see a graphical representation of the HI collision in Fig. 2.1. The connection between the collision geometry and centrality is described by the Glauber model [13].

Mathematically, centrality c can be expressed as

$$c = \frac{\int_0^b \frac{\mathrm{d}\sigma}{\mathrm{d}b'}\mathrm{d}b'}{\int_0^\infty \frac{\mathrm{d}\sigma}{\mathrm{d}b'}\mathrm{d}b'}, \tag{2.3}$$

where $\frac{\mathrm{d}\sigma}{\mathrm{d}b'}$ is the differential cross-section of the collision with respect to the impact parameter.

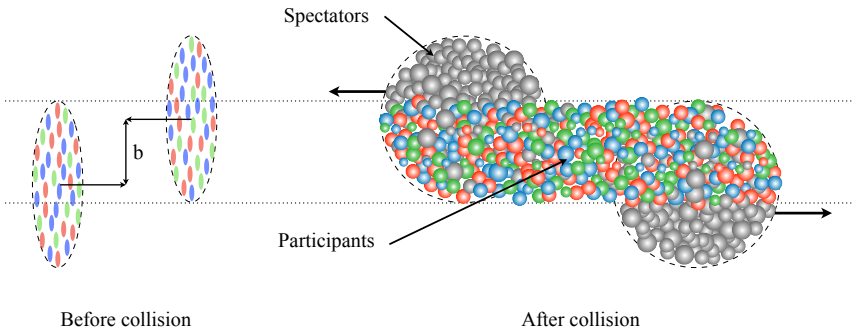

Figure 2.1: Scheme of a HI collision. Taken from [14].

As mentioned in Sec. 1.2.2, the determination of centrality at ATLAS involves measuring the total transverse energy E_{T} deposited in the FCal, as illustrated in Fig. 2.2. The acquired data are organized into equal cross-section bins, with each bin corresponding to a specific centrality percentile. The centrality interval of 0-10% involves the most central collisions characterized by small impact parameter b. Conversely, peripheral collisions, where only a few nucleons interact, are categorized within the centrality interval of 60-80%.

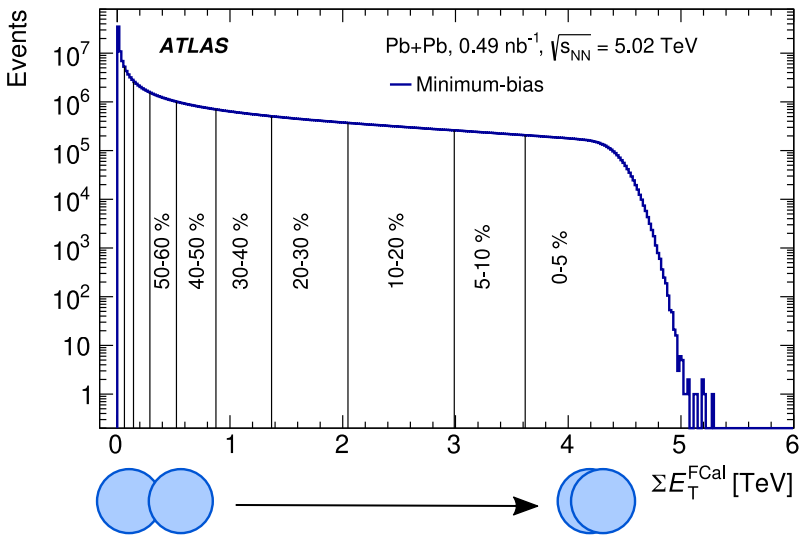

Figure 2.2: Total transverse energy E_{T} measured with the ATLAS Forward Calorimater in PbPb collisions. Centrality is divided into percentile intervals by vertical lines. Taken from [15].

2.3 Jet Physics

Jets are collimated sprays of particles that emerge from high-energy collisions. They are fundamental objects in particle physics research and play a crucial role

in our understanding of the strong force and the structure of hadrons.

The mechanism of jet creation can be described by a situation when two partons are created in the initial hard scattering. Such partons can radiate gluons, which leads to a parton shower creation. In addition, when two quarks are getting further from each other, the potential energy between them increases thanks to the character of strong interaction. When the potential energy is high enough for the creation of a pair quark-antiquark ($q\bar{q}$), such a pair emerges from the vacuum, see Fig. 2.3. This process of quark creation and gluon radiation continues as long as partons have enough energy. The final result is a collimated shower of particles – jet.

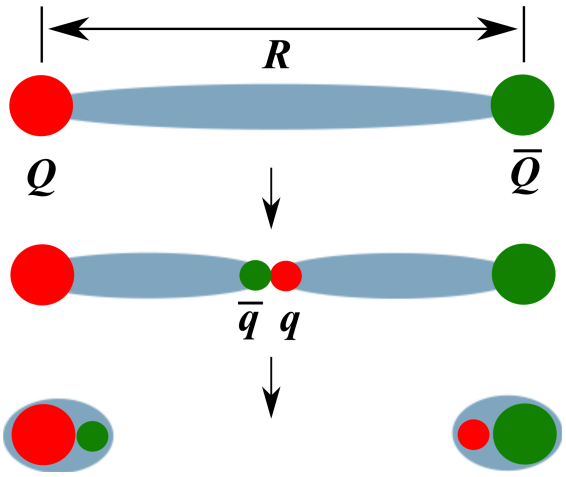

Figure 2.3: Creation of a pair $q\bar{q}$ from intial quarks. Taken from [16].

Jets carry information about the properties of the quarks and gluons from which they originated, as well as insights into the underlying physics processes occurring during the collision. Studying jets allows physicists to probe the dynamics of the strong force, test predictions from QCD, and search for new particles or phenomena beyond the Standard Model of particle physics.

2.3.1 Jet Reconstruction Algorithms

Jet reconstruction algorithms are used to define jets. Jet constituents can be either final-state particles, calorimetric towers, tracks, or jets. Detectors have limited precision of measurement, so the information about particle kinematics is given by calorimetric towers or clusters measured with calorimeters, or reconstructed tracks. So in the case of measured data jets consist of either calorimetric towers or tracks. The jets can be further clustered to form larger jets if an analysis requires that. However, from MC simulations one has also precise information about the particle kinematics, so in this case, the jet constituents can be final-state particles.

Some aspects of an algorithm that need to be considered are the jet radius and whether the algorithm is infrared and collinear (IRC) safe. Infrared safety means that by adding infinitely soft particles the jet definition remains the same. Collinear safety means that by splitting one jet constituent into two the jet definition does not change. If an algorithm is IRC unsafe, the perturbative QCD calculations will be affected [12].

A very important parameter that must be considered by a jet reconstruction algorithm is jet radius R. It describes the size of a jet in $\eta-\phi$ space. The distance between i-th and j-th particle in the $\eta-\phi$ space is given by the formula

$$\Delta R_{ij} = \sqrt{(\eta_i - \eta_j)^2 + (\phi_i - \phi_j)^2}. \tag{2.4}$$

There are two classes of jet algorithms: cone and sequential clustering algorithms. Cone algorithms operate under the assumption that particles within jets will predominantly appear within conical regions. Consequently, they cluster particles based on their $\eta-\phi$ space coordinates, leading to jets characterized by fixed circular boundaries. While cone algorithms have historically been favored by experimentalists due to their ease of implementation, they are not as popular among theorists, primarily due to their reliance on non-physical constants. Moreover, cone algorithms are generally considered to be IRC unsafe. The most known cone algorithms are IC-PR, IC-SM, and IRC safe. More information about these algorithms can be found here [17].

Sequential clustering algorithms operate under the assumption that particles within jets exhibit minor differences in transverse momenta. Consequently, these algorithms group particles based on momentum space, leading to jets characterized by varying areas in $\eta-\phi$ space. While sequential clustering algorithms have traditionally been preferred by theorists, experimentalists were less inclined to use them due to their historically slow computational performance. However, with the advent of the FastJet package, clustering algorithms have significantly improved in speed, making them more appealing to experimentalists as well. Additionally, sequential clustering algorithms adhere to the IRC safety criteria. The most known sequential algorithms are k_t, anti-k_t, and Cambridge Aachen (C/A) [17].

The clustering process for sequential clustering algorithms follows this procedure: Initially, the algorithm calculates all distances d_{ij} and $d_{i\mathrm{B}}$ (see Table 2.1) and identifies the smallest one. If d_{ij} is the smallest distance, it merges the i-th and j-th particle into a single entity. Conversely, if the smallest distance is $d_{i\mathrm{B}}$, the algorithm isolates the i-th particle and designates it as a jet. This iterative process continues until all particles are clustered into jets.

The performance of the mentioned sequential algorithms and the SIScone algorithm (which is a cone algorithm) is shown in Fig. 2.4.

algorithm	d_{ij}	$d_{i\mathrm{B}}$
k_t	$\min\left(p_{\mathrm{T}i}^2, p_{\mathrm{T}j}^2\right)\frac{\Delta R_{ij}^2}{R}$	$p_{\mathrm{T}i}^2$
anti-k_t	$\min\left(\frac{1}{p_{\mathrm{T}i}^2}, \frac{1}{p_{\mathrm{T}j}^2}\right)\frac{\Delta R_{ij}^2}{R}$	$\frac{1}{p_{\mathrm{T}i}^2}$
C/A	$\frac{\Delta R_{ij}^2}{R}$	1

Table 2.1: Definitions of d_{ij} and $d_{i\mathrm{B}}$ for the sequential clustering algorithms. $p_{\mathrm{T}i}$ and $p_{\mathrm{T}j}$ are the transverse momenta of i-th and j-th particle, respectively. ΔR_{ij} is their mutual distance in the $\eta-\phi$ space, and R is jet radius.

A jet reconstruction algorithm determines also jet kinematics. Kinematics of a jet is characterized by jet energy E, momentum p, rapidity y, pseudorapidity η (which is the same as rapidity in most cases), etc. However, the crucial property of a jet is transverse momentum $p_{\mathrm{T}}^{\mathrm{jet}}$, because as mentioned in Section 1.2.1, p_{T} is Lorentz invariant quantity along the z-axis. Thus, jet spectra are measured in terms of $p_{\mathrm{T}}^{\mathrm{jet}}$.

In the analysis performed within this thesis, the anti-k_t algorithm was used. The definition of d_{ij} for the anti-k_t algorithm implies that the algorithm prefers to cluster hard[1] particles first. Consequently, the fluctuation in the area in the $\eta - \phi$ space is minimal. The anti-k_t algorithm's preference for clustering results in superior jet resolution capabilities; however, its suboptimal de-clustering performance makes it less suitable for studying jet substructure [17].

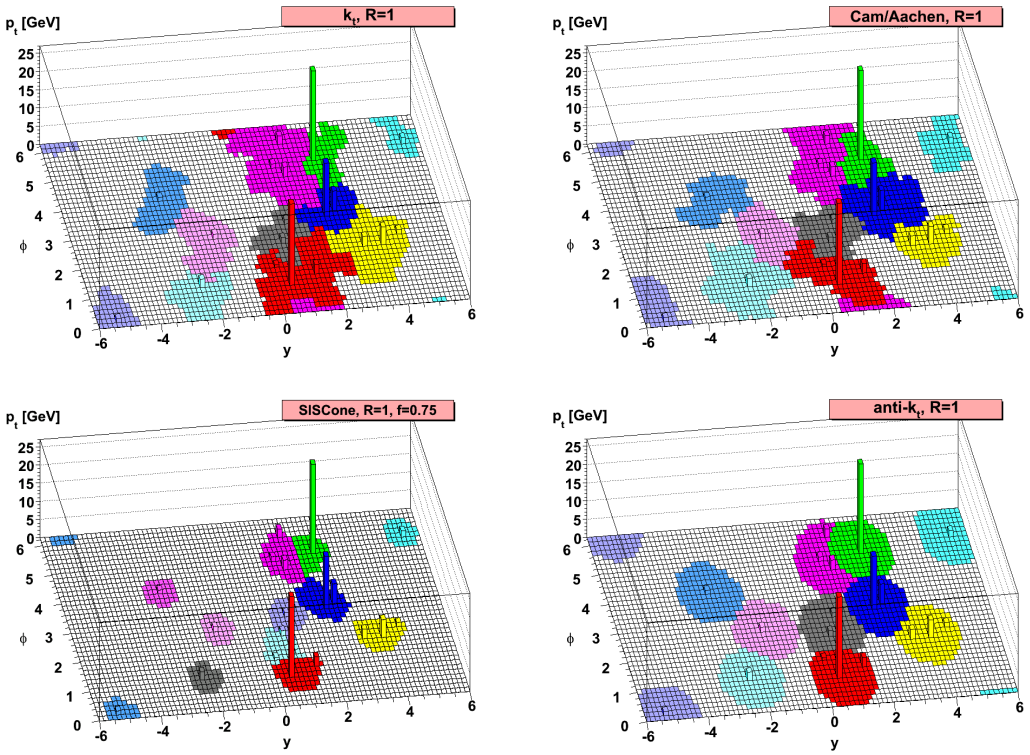

Figure 2.4: Comparison of the performance of four distinct jet reconstruction algorithms operating on calorimetric tower data in the $\eta - \phi$ space within the same event. The event includes a background of soft particles. Taken from [18].

2.3.2 QGP and Jet Quenching

QGP can be produced at the LHC on an extremely short time scale when two relativistic heavy ions are collided. As the nuclei pass through each other, a region of extremely large energy density is formed (greater than 12 GeV/fm^3) [1]. It is believed that QGP existed for a few millionths of a second after the Big Bang. It means that physicists recreate the conditions of the early Universe by relativistic HI collisions. The temperature of QGP is estimated above 10^{12} K

[1] Hard particles are the particles with high p_{T}.

(see phase diagram in Fig. 2.5). However, after a very short time, the partons recombine into hadrons – mainly pions and kaons.

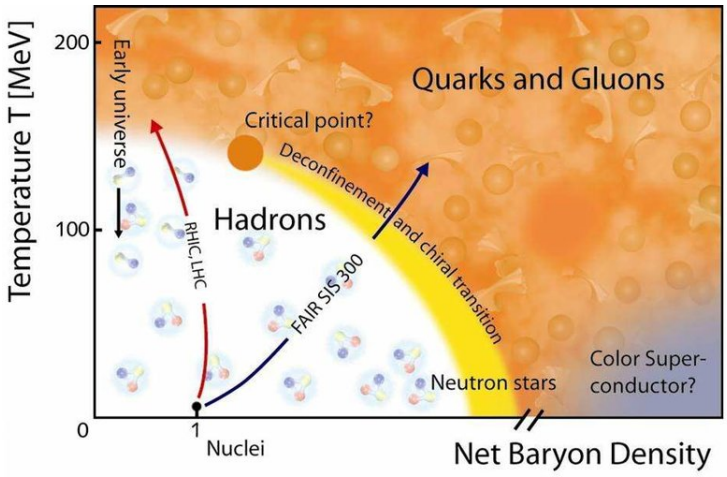

Figure 2.5: Phase diagram of QGP. Note: 1 MeV $\approx 10^{10}$ K. Taken from [19].

In HI collisions, the first indications of QGP existence were observed in 2003 in the STAR and PHENIX experiments at accelerator RHIC in the US [20]. There were measured different angular distributions of particles coming from pp and HI collisions. Later, there was observed unexpected behavior of jets produced in HI collisions at the LHC. One of the two back-to-back jets was significantly suppressed. Such unexpected behavior can be explained by the existence of QGP. A jet penetrating through the QGP deposits some amount of energy in the QGP, so one of the jets lost more energy than the other one. This phenomenon is called jet quenching. Thus, jet measurements in HI collisions are of great interest to study the microscopic structure of the QGP liquid [1]. While jets are well-defined entities in QCD and are effectively understood in pp collisions, their dynamics in HI collisions exhibit distinct characteristics. The initial, hard scatterings responsible for jet production occur in the early phases of the collision. The subsequent evolution of the scattered parton, transitioning towards hadronization, unfolds within the evolving QGP medium. This intricate process introduces modifications compared to the well-understood dynamics observed in pp collisions.

Jet quenching can be quantified by the measurement of several quantities. Here we will discuss nuclear modification factor R_{AA} and central-to-peripheral collision yield ratio R_{CP}. While R_{AA} is defined as the ratio of jet spectra in central HI and pp collisions, R_{CP} is the ratio of jet spectra in central and peripheral HI collisions. These quantities are given by formulae [1]

$$R_{\mathrm{AA}} = \frac{\frac{1}{\langle T_{\mathrm{AA}} \rangle} \frac{1}{N_{\mathrm{evt}}} \frac{\mathrm{d}^2 N_{\mathrm{jet}}}{\mathrm{d}p_{\mathrm{T}} \mathrm{d}y}\Big|_{\mathrm{cent}}}{\frac{\mathrm{d}^2 \sigma_{\mathrm{jet}}}{\mathrm{d}p_{\mathrm{T}} \mathrm{d}y}\Big|_{\mathrm{pp}}},$$

$$R_{\mathrm{CP}} = \frac{\frac{1}{\langle T_{\mathrm{AA}} \rangle} \frac{1}{N_{\mathrm{evt}}} \frac{\mathrm{d}^2 N_{\mathrm{jet}}}{\mathrm{d}p_{\mathrm{T}} \mathrm{d}y}\Big|_{\mathrm{cent}}}{\frac{1}{\langle T_{\mathrm{AA}} \rangle} \frac{1}{N_{\mathrm{evt}}} \frac{\mathrm{d}^2 N_{\mathrm{jet}}}{\mathrm{d}p_{\mathrm{T}} \mathrm{d}y}\Big|_{\mathrm{per}}}, \tag{2.5}$$

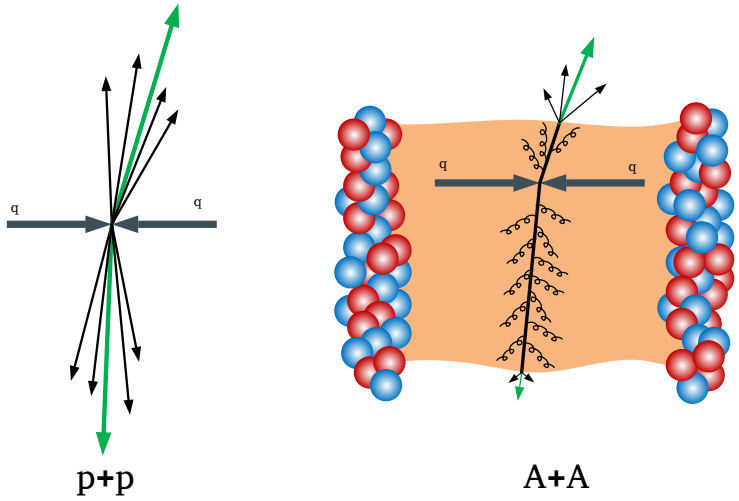

Figure 2.6: Left: jets in pp collisions. Right: jet quenching in QGP. Taken from [21].

where N_{evt} is the number of events, $\frac{\mathrm{d}^2 N_{\text{jet}}}{\mathrm{d}p_{\text{T}}\mathrm{d}y}$ is the number of jets with respect to p_{T} and y, $\frac{\mathrm{d}^2\sigma_{\text{jet}}}{\mathrm{d}p_{\text{T}}\mathrm{d}y}$ is a differential cross section of jets with respect to p_{T} and y, and $\langle T_{\text{AA}}\rangle$ is the nuclear thickness function. The type of collision is set behind the vertical line: cent = central PbPb collisions, per = peripheral PbPb collisions, and pp serves for proton-proton collisions.

In short, the nuclear thickness function accounts for an enhancement of the hard-scattering rate due to the larger geometric overlap between the colliding nuclei. In both cases, $\langle T_{\text{AA}}\rangle$ is calculated via the Glauber model [13]. It is important to mention that the measured values of R_{AA} and R_{CP} are less than 1 since in central PbPb collisions the jets are quenched the most.

Additionally, one can look at how the jet structure is modified in the QGP [22]. This can be addressed by measuring of charged-particle p_{T} distribution at a distance r around the jet axis $D(p_{\text{T}}, r)$ which is given by the formula

$$D(p_{\text{T}}, r) = \frac{1}{N_{\text{jet}}} \frac{1}{2\pi r \mathrm{d}r} \frac{\mathrm{d}n_{\text{ch}}(p_{\text{T}}, r)}{\mathrm{d}p_{\text{T}}}, \tag{2.6}$$

where N_{jet} is the number of jets in consideration and $n_{\text{ch}}(p_{\text{T}}, r)$ is the number of charged particles with a given p_{T} at a distance r from the jet axis. The ratio of the charged-particle yields measured in HI and pp collisions $R_{D(p_{\text{T}},r)}$ is then

$$R_{D(p_{\text{T}},r)} = \frac{D(p_{\text{T}}, r)_{\text{HI}}}{D(p_{\text{T}}, r)_{\text{pp}}}. \tag{2.7}$$

The ratio $R_{D(p_{\text{T}},r)}$ quantifies the modifications of the yields due to the QGP medium. The modification of charged-particle yields associated with the calorimetric jets, sorted according to the charged-particle p_{T} is shown in Fig. 2.7. Since the values of $R_{D(p_{\text{T}},r)}$ for the charged particles with $p_{\text{T}} < 4$ GeV are greater than 1, exclusion of these particles from a track jet would lead to the accidental suppression of R_{AA}.

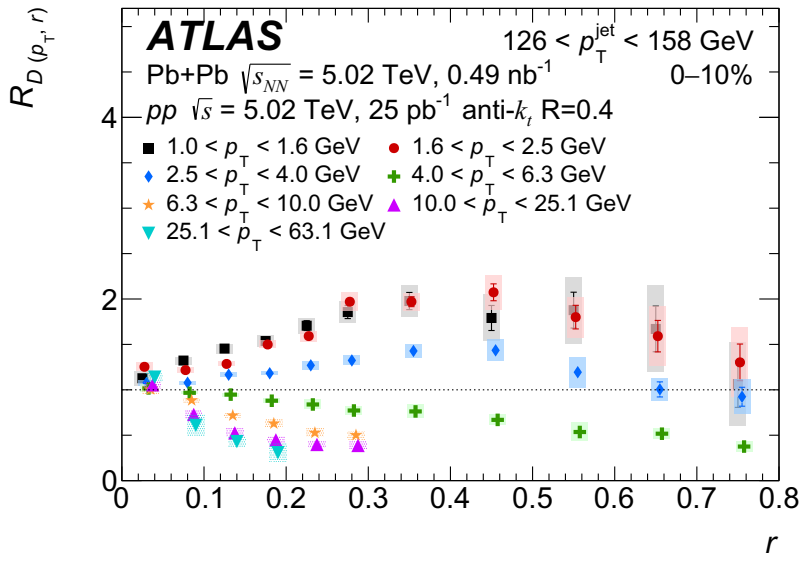

Figure 2.7: $R_{D(p_{\mathrm{T}},r)}$ as a function of angular distance r for $126 < p_{\mathrm{T}}^{\mathrm{jet}} < 158$ GeV and jet radius $R = 0.4$ for seven p_{T} selections of charged particles involved in the calorimetric-jet area in central PbPb collisions. The vertical bars on the data points indicate statistical uncertainties, while the shaded boxes indicate systematic uncertainties. Taken from [22].

2.4 Motivation for the Thesis

The motivation for this work is the following. The ATLAS, ALICE, and CMS experiments obtained results from the measurement of jet suppression in PbPb collisions for various jet radii [2, 3, 4, 5]. The results from individual experiments are displayed namely in Figures 2.8, 2.9, and 2.10. The common plot of the ratio of R_{AA} for jet radii $R = 0.4$ and $R = 0.2$ was also made, see Fig. 2.11.

Whereas for ATLAS measurement the values of the R_{CP} double ratio are above the unity for low $p_{\mathrm{T}}^{\mathrm{jet}}$, for ALICE measurement the values are below the unity. However, the dependence of R_{AA} on R is not theoretically described qualitatively. There exist some models predicting that the suppression is smaller with increasing R, while the other models predict the opposite behavior, see Figures 2.9 and 2.12. More information about the models from the figures can be found here [5, 23, 24, 25].

2.4.1 Differences in Measurements

Fig. 2.11 shows that results from the experiments are inconsistent with each other. However, the measurements in the individual experiments were not performed in the same conditions. In this subsection, the impacts of differences in the measurements on the results are discussed.

Collision energy

ATLAS measurement from 2013 (light green in Fig. 2.11) was performed at collision energy $\sqrt{s_{\mathrm{NN}}} = 2.76$ TeV [2], while the collision energy in the other mea-

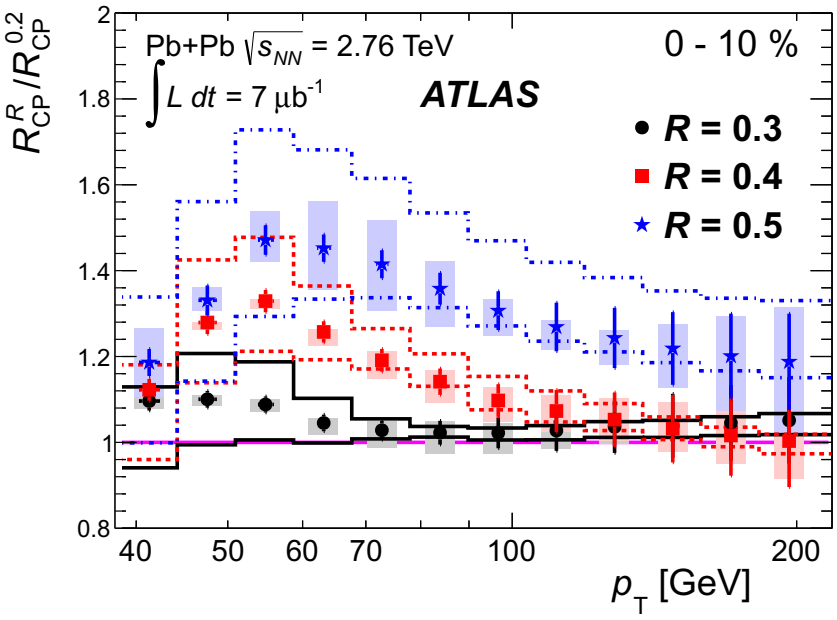

Figure 2.8: Ratios of R_{CP} values between $R = 0.3, 0.4$, and 0.5 jets and the reference $R = 0.2$ jets as a function of $p_{\mathrm{T}}^{\mathrm{jet}}$ in the 0–10% centrality bin from the ATLAS experiment. The error bars show statistical uncertainties. The shaded boxes indicate partially correlated systematic errors. The lines indicate systematic errors that are fully correlated between different p_{T} bins. Taken from [2].

surements is $\sqrt{s_{\mathrm{NN}}} = 5.02$ TeV. This affects R_{AA} through the different straight of quenching and spectra shape. A comparison of R_{AA} (see Eqn. 2.5) for collision energies of 5.02 TeV and 2.76 TeV for two centrality bins and jet radius 0.4 can be seen in Fig. 2.13. Additionally, a comparison of $R_{D(p_{\mathrm{T}})}$ (see Eqn. 2.7) for the same two collision energies for p_{T} interval 126–158 GeV and jet radius 0.4 is displayed in Fig. 2.14. It seems that the impact of collision energy on such scales has only minimal impact on jet quenching.

R_{AA} vs R_{CP}

The jet-quenching measurement from ALICE, ATLAS, and CMS experiments at $\sqrt{s_{\mathrm{NN}}} = 5.02$ TeV is expressed in terms of R_{AA}. In contrast, the measurement of jet quenching from the ATLAS experiment at $\sqrt{s_{\mathrm{NN}}} = 2.76$ TeV is expressed in terms of R_{CP}, where as peripheral collisions are considered those with centrality 60–80%. The reason is that data within this measurement were collected in 2010, and there was not sufficient available statistics in pp collisions. The conversion from the double ratio of R_{CP} to R_{AA} for any centrality interval can be made by multiplication of the R_{CP} double ratio for given centrality bin by the R_{AA} double ratio for centrality bin 60–80%. The values of this double ratio are supposed to be slightly below the unity, so this effect would have only a small impact on the results. For example, one can see in Fig. 2.10 in the upper row that the values of the R_{AA} double ratio for $R = 0.4$, centrality bin 50–90% (green color), and $p_{\mathrm{T}}^{\mathrm{jet}}$ from 200 to 400 GeV are close to 1.

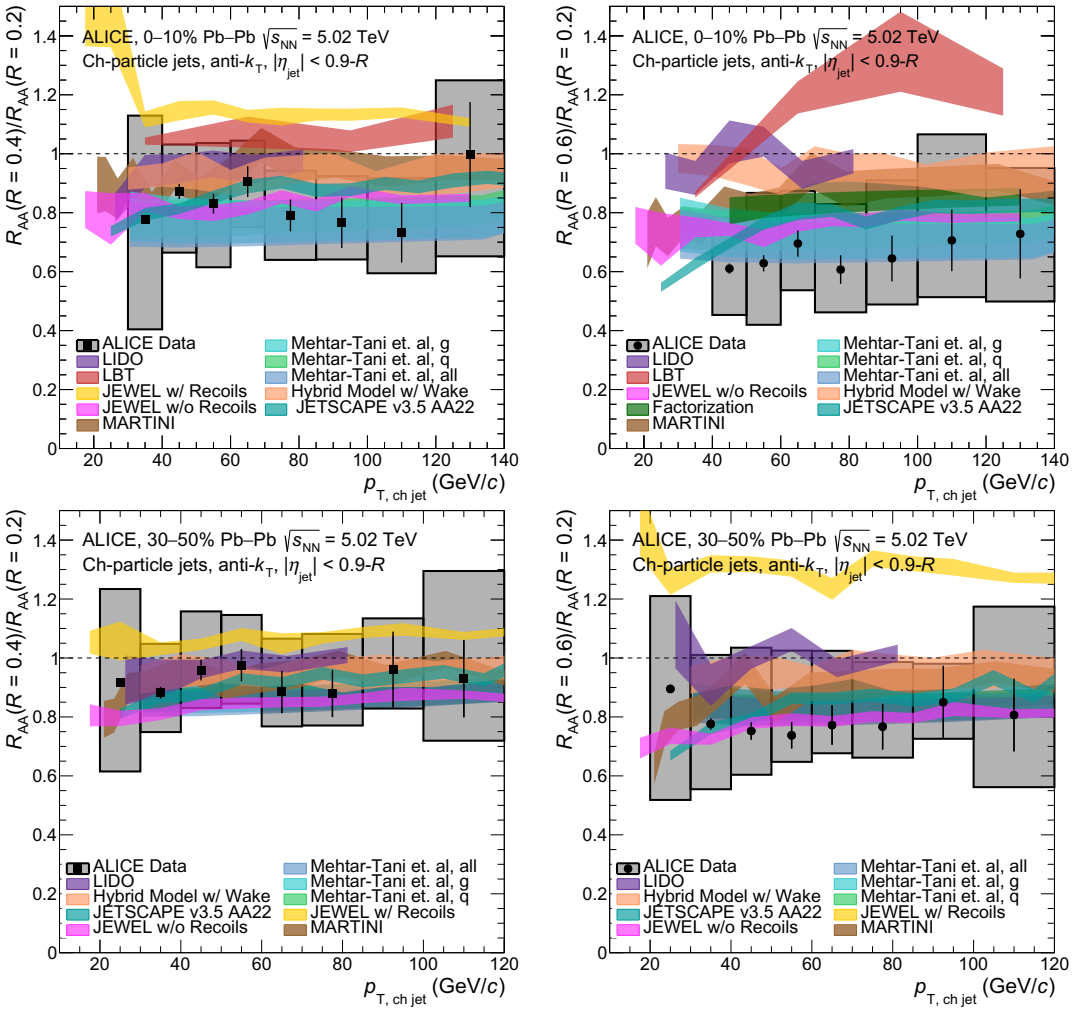

Figure 2.9: Double ratio of jet nuclear modification factors using $R_{\mathrm{AA}}^{R=0.2}$ as the denominator and using $R = 0.4$ (left) and $R = 0.6$ (right) as the numerator from the ALICE experiment compared to model predictions for central (top row) and semi-central (bottom row) collisions. The statistical uncertainties of data are shown as vertical lines, whereas the systematic uncertainties are shown as shaded boxes. Taken from [4].

Jet Constituents

Another difference between the measurements is the type of jet constituents. Jets measured by ALICE are created from tracks – charged particles only. On the other hand, jet constituents in ATLAS are calorimetric towers, whereas CMS exploits information from both calorimetric and tracking detectors for jet reconstruction. Thus, within the analysis included in this thesis, data from ATLAS are processed in the following way. The procedure that clusters tracks into jets is performed, and the dependence of charged-jet p_{T} spectrum and R_{AA} on jet radius R is investigated.

Background subtraction

In the analysis of HI collisions, a significant portion of the observed particle activity comes from the underlying event (UE) [29], which can obscure signals of

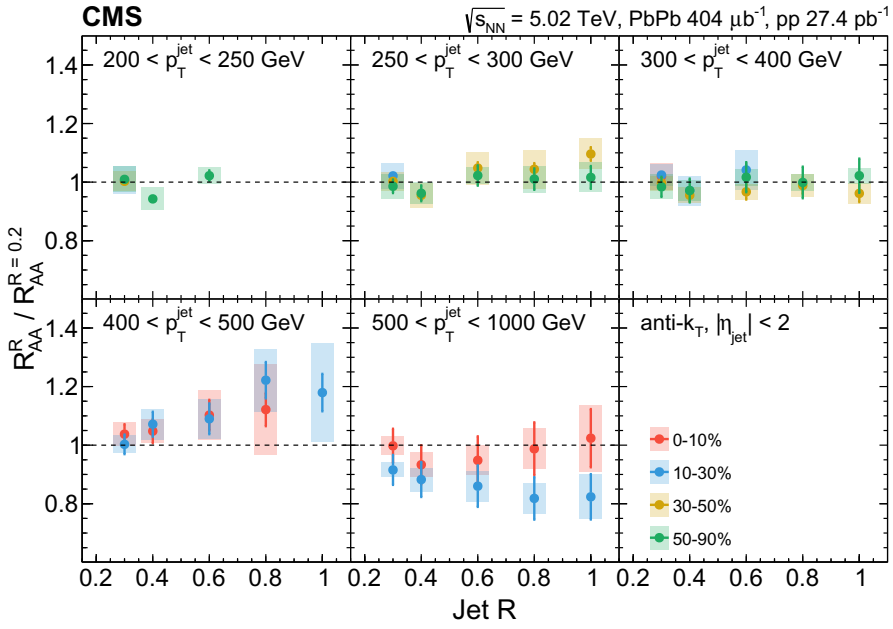

Figure 2.10: The R_{AA} double ratio as a function of jet radius R with respect to $R = 0.2$, in various event centrality bins and $p_{\mathrm{T}}^{\mathrm{jet}}$ ranges from the CMS experiment. The statistical uncertainties of data are shown as vertical lines, whereas the systematic uncertainties are shown as shaded boxes. Taken from [5].

interest. Briefly, the UE refers to additional particle activity apart from the primary hard scattering process of interest, such as multiple nucleon-nucleon interactions, multi-parton interactions, initial- and final-state radiation, and other secondary interactions within the collision environment. The UE presents challenges for data analysis and interpretation in high-energy physics experiments, and specialized methods are employed to mitigate their effects and extract meaningful physics results. It is also important to estimate systematic uncertainties depending on the used method to subtract UE. The most commonly used is the area-based method, which was applied to the data of interest in ATLAS and CMS experiments [2, 3, 5]. However, the machine-learning-based (ML) technique was applied to the data of interest within the ALICE experiment [4].

Another effect that contributes to the background is pile-up (PU), which refers to the occurrence of multiple simultaneous collisions within the same bunch crossing in collider experiments. The PU is the main source of background in pp collisions. However, the contribution of the PU to the background in HI collisions is negligible with respect to the UE (in the order of 10^{-3}).

The area-based method for background subtraction [30] starts with the computation of the average background momentum density ρ. The calculation of ρ differs for individual experiments. The corrected momentum $p_{\mathrm{T,\,jet}}^{\mathrm{corr}}$ of a certain jet (reconstructed with a jet algorithm and parameters set within the analysis) is then computed as

$$p_{\mathrm{T,\,jet}}^{\mathrm{corr}} = p_{\mathrm{T,\,jet}}^{\mathrm{raw}} - \rho A_{\mathrm{jet}}, \tag{2.8}$$

where $p_{\mathrm{T,\,jet}}^{\mathrm{raw}}$ is the transverse momentum of the reconstructed jet before background subtraction, and A_{jet} is the jet area [31]. This procedure is applied

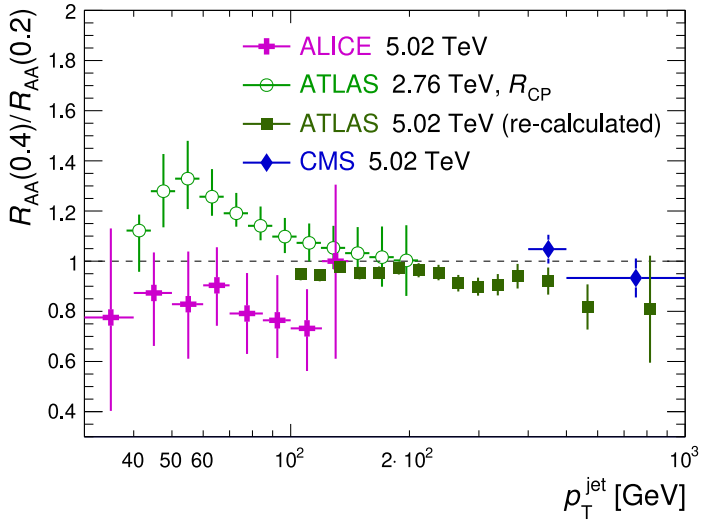

Figure 2.11: Comparison of jet suppression for jet radii $R = 0.4$ and $R = 0.2$ measured with experiments ATLAS, ALICE, and CMS in central PbPb collisions. There is also introduced the collision energy per nucleon for each experiment in the plot. Re-calculated (dark green) means that the ratio was made additionally, it is not officially published. Plot made by Yeonju Go.

event-by-event. Finally, systematic uncertainties associated with the background estimation should be carefully evaluated and accounted for in the final results.

The ML-based method for background subtraction used by ALICE is described in the steps [32] displayed in Fig. 2.15. The neural network is trained and tested on data from MC simulations. First of all, the toy model data are created. To create events with particle jets in a HI background, events generated by PYTHIA [33] at $\sqrt{s} = 5.02$ TeV are embedded in a thermal background. The thermal background is created by randomly distributing charged particles according to realistic particle multiplicity and momentum distributions. The multiplicity distribution is modeled with a Gaussian function with a mean of 1800 and a width of 200, which roughly reproduces the multiplicity in central PbPb events at $\sqrt{s_{\mathrm{NN}}} = 5.02$ TeV. The second step is the training of the ML-based estimators and their evaluation on the toy model. However, since jet quenching is not described properly by the toy model, the background estimators trained on this toy model serve for a significant systematic uncertainty analysis on real data (see shaded boxes in Fig. 2.9). In the third phase, the trained and verified estimator is utilized on HI data to derive background-corrected spectra. In addition, a response matrix is created to account for detector effects. The final step entails the unfolding process to obtain the final spectra.

Another approach to massively reduce the background effects is to set a higher $p_{\mathrm{T}}^{\mathrm{cut}}$ on jet constituents since the background is dominated by low-p_{T} particles. However, a great disadvantage of this approach is that the low-p_{T} constituents of a jet are also discarded. Thus, the thesis deals also with the question of the impact of $p_{\mathrm{T}}^{\mathrm{cut}}$ to jet constituents on the charged-jet p_{T} spectra and R_{AA}. In addition, the ICS method [29] for background subtraction is implemented within the analysis, which enables setting the $p_{\mathrm{T}}^{\mathrm{cut}}$ to lower values. The ICS method is more discussed in Chap. 7.

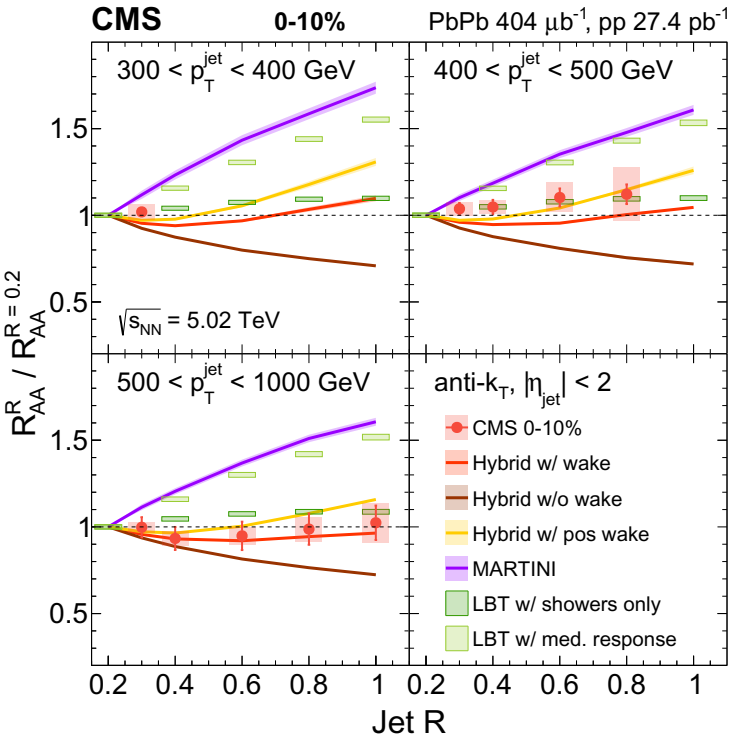

Figure 2.12: The ratio of R_{AA} for various jet radii R to the reference $R = 0.2$, in various $p_{\mathrm{T}}^{\mathrm{jet}}$ ranges for the 0-10% centrality interval. The statistical uncertainties of data are shown as vertical lines, whereas the systematic uncertainties are shown as shaded boxes. The predictions from the HYBRID (dark orange, brown, and yellow), MARTINI (purple), and LBT (lime and dark green) models are compared to the data as colored bands. Taken from [5].

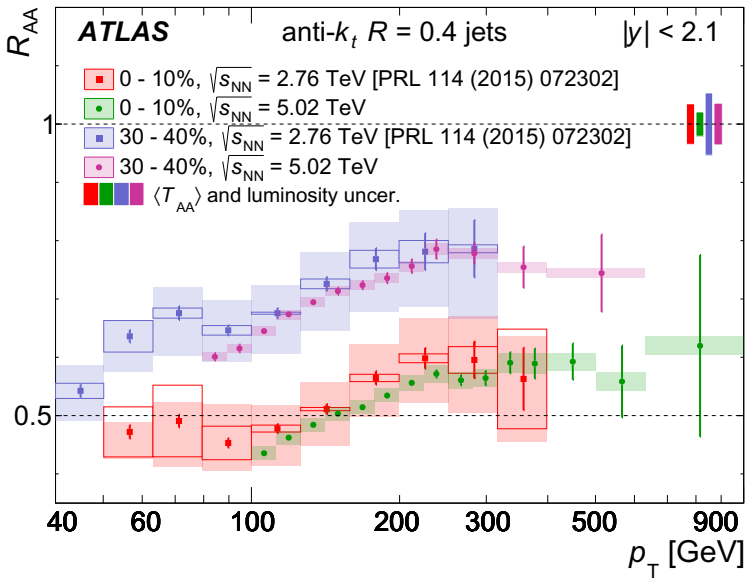

Figure 2.13: The R_{AA} as a function of $p_{\mathrm{T}}^{\mathrm{jet}}$ at collision energies 2.76 TeV and 5.02 TeV for two centrality bins 0–10% and 30–40%. The error bars represent statistical uncertainties, and the shaded boxes around the data points represent bin-wise correlated systematic uncertainties. Taken from [26].

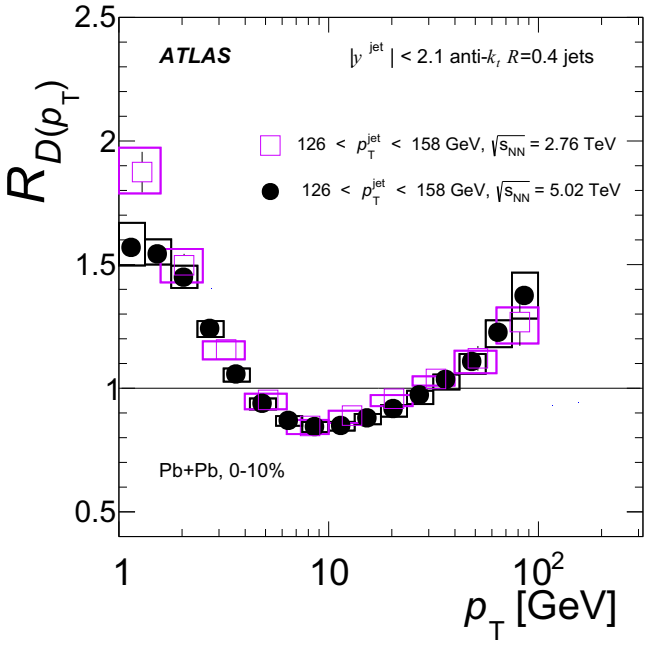

Figure 2.14: $R_{D(p_{\mathrm{T}})}$ for 126–158 GeV jets for collision energies of 5.02 TeV [27] and 2.76 TeV [28] in central PbPb collisions. The vertical bars on the data points indicate statistical uncertainties while the boxes indicate systematic uncertainties. Taken from [27].

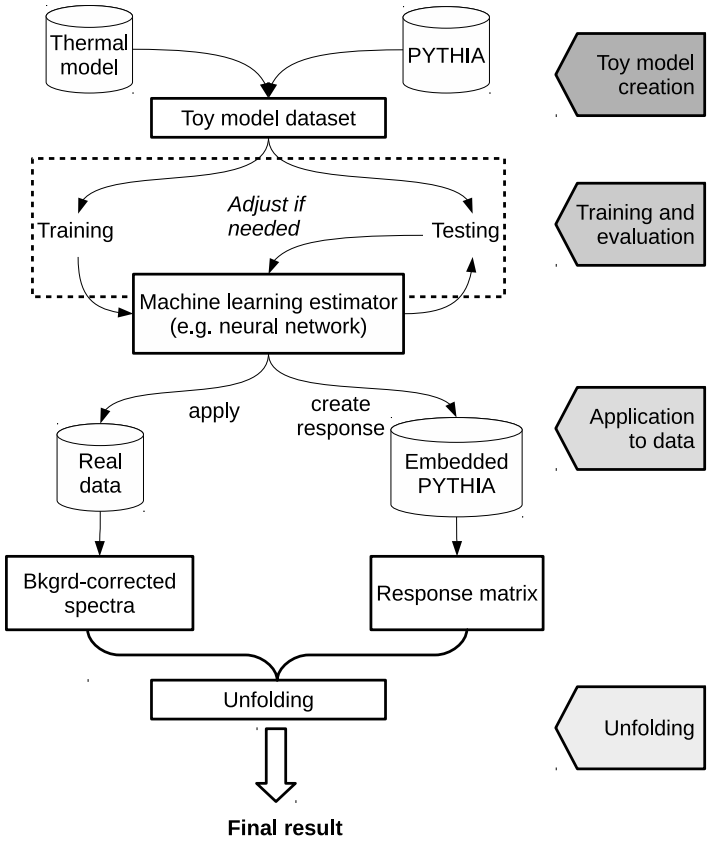

Figure 2.15: Illustration of the full proposed analysis strategy using the ML-based method for background subtraction by ALICE. Taken from [32].

3. Dataset

3.1 Data Samples

This analysis uses 1.72 nb^{-1} of PbPb data at $\sqrt{s_{\text{NN}}} = 5.02$ TeV recorded in 2018, and 257 pb^{-1} of pp data collected in 2017 at the same collision energy. Various hard probe triggers (high-p_{T} jets, muons, electrons, and photons) are grouped into a Hard Probe (HP) stream and the Main stream in PbPb and pp data-taking periods, respectively. Additionally to the jet-triggered data sample, pp collisions recorded by Minimum-Bias (MB) triggers grouped into the MB stream are utilized in this analysis. Mutually exclusive streams of peripheral events and central events are combined to obtain an MB PbPb data sample. The run numbers for each set are given in Appendix A.1.

3.2 Event Selection

The standard HI event quality requirements were applied for the event selection both for the pp and PbPb events.

- All the sub-detector systems were required to be fully functional: all the data were required to pass the official good run lists.
- All events are required to have a good reconstructed primary vertex.
- Additional event cleaning to remove additional detector imperfections (problematic events due to LAr, Tile, SCT, incomplete events).
- No PU removal is applied in pp collisions (typical μ is 2).
- In PbPb collisions, the out-of-time PU contribution is removed.
- In PbPb collisions, the in-time PU contribution is removed. The main motivation to remove the PU contribution in PbPb collisions is to not bias centrality estimation.

3.3 Trigger Selection

To maintain efficiency for events containing hard probes, specific jet triggers are used. As mentioned in Sec. 1.2.4, events are first identified at L1 by various L1 triggers. These L1 "seeds" are passed to the HLT, where the jet trigger algorithm with various thresholds on $p_{\text{T}}^{\text{jet}}$ was used for the final selection.

HLT jet triggers both in pp, and PbPb collisions were seeded by different L1 seeds: a) L1 jet triggers performing a simple sliding window algorithm to find jet candidates (`L1J`) with E_{T} threshold ranging from 15 to 30 GeV or b) total energy trigger requiring 20 GeV of total energy at the L1. The HLT jet trigger uses a jet reconstruction algorithm similar to that used in the offline analysis, and various E_{T} thresholds are applied to jet trigger collection at the HLT. The jet trigger uses anti-k_t $R = 0.4$ jets. The lists of used triggers for corresponding p_{T} bins are

given in Tab. 3.1 and 3.2 for pp and PbPb collisions, respectively. This analysis uses only jet triggers in the region of $p_{\mathrm{T}}^{\mathrm{jet}}$ for which the triggers are fully efficient[1]. A detailed description of the jet triggers in HI collisions can be found in [11].

trigger	$p_{\mathrm{T}}^{\mathrm{jet}}$ [GeV]
HLT_j40_0eta490_L1TE20	72-79
HLT_j50_L1J15	79-84
HLT_j60	84-102
HLT_j75_L1J20	102-112
HLT_j85	112-124
HLT_j100_L1J20	>124

Table 3.1: Triggers used in the analysis of 2017 pp data and the corresponding $p_{\mathrm{T}}^{\mathrm{jet}}$ ranges.

trigger	$p_{\mathrm{T}}^{\mathrm{jet}}$ [GeV]
HLT_j50_ion_L1J12	79-84
HLT_j60_ion_L1J15	84-102
HLT_j75_ion_L1J30	102-112
HLT_j85_ion_LIJ30	>112

Table 3.2: Triggers used in the analysis of 2018 PbPb data and the corresponding $p_{\mathrm{T}}^{\mathrm{jet}}$ ranges.

3.4 Monte Carlo Samples

This analysis utilizes MC16 PYTHIA8 pp jet events at $\sqrt{s} = 5.02$ TeV with the A14 ATLAS tune and the NNPDF23LO pdfs. The summary of the pp MC samples can be found in Tab. 3.3. The PbPb MC sample uses PYTHIA8 events with the same tune and pdfs as in pp MC samples that are overlayed on top of events from a dedicated sample of real MB PbPb collisions. The PYTHIA model is used since the theoretical model that would describe jet quenching well does not exist. The overlay procedure guarantees that the UE is perfectly described in the simulations. The overlayed samples (listed in Tab. 3.4) were recorded with a mixture of MB triggers and total energy triggers requiring 1.5 TeV or 6.5 TeV to enhance the number of central collisions. The samples were reweighted on an event-by-event basis for unfolding purposes and to evaluate measured distributions in the MC such that they have the same centrality distribution as the jet-triggered data sample. The reweighting factors are estimated as the ratio between normalized $E_{\mathrm{T}}^{\mathrm{FCal}}$ distributions and are discussed in more detail at the beginning of Chap. 5. The pp MC is generated with the PU contamination that matches the one in the data. No PU reweighting is performed in the analysis.

[1] Efficiency is better than 99%.

JZ	Q [GeV]	σ [nb] $\times$ ϵ	#events
1	20–60	$(6.8 \times 10^{7}) \times (2.9 \times 10^{-3})$	8 M
2	60–160	$(6.4 \times 10^{5}) \times (4.29 \times 10^{-3})$	8 M
3	160–400	$(4.7 \times 10^{3}) \times (5.30 \times 10^{-3})$	8 M
4	400–800	$(2.7 \times 10^{1}) \times (4.59 \times 10^{-3})$	8 M
5	800–1600	$(2.2\times 10^{-}1) \times (2.18 \times 10^{-3})$	8 M

Table 3.3: MC samples of pp collisions generated by PYTHIA8.

JZ	Q [GeV]	σ [nb] $\times$ ϵ	#events
1	20–60	$(6.8 \times 10^{7}) \times (2.8 \times 10^{-3})$	7.7 M
2	60–160	$(6.4 \times 10^{5}) \times (4.29 \times 10^{-3})$	7.7 M
3	160–400	$(4.7 \times 10^{3}) \times (5.30 \times 10^{-3})$	7.7 M
4	400–800	$(2.7 \times 10^{1}) \times (4.59 \times 10^{-3})$	7.5 M
5	800–1600	$(2.2\times 10^{-}1) \times (2.18 \times 10^{-3})$	7.7 M

Table 3.4: PbPb MC overlay datasets.

4. Experimental Data Processing

First of all, the data are organized in so-called trees. From the tree, one can obtain various observables for each event:

- Kinematic quantities of calorimetric jets: transverse momentum $p_{\mathrm{T}}^{\mathrm{jet}}$, pseudorapidity η^{jet}, azimuth angle ϕ^{jet}, and mass M^{jet}. These jets were reconstructed from calorimetric towers with the anti-k_t algorithm with a fixed radius $R = 0.4$.
- Kinematic quantities of tracks: transverse momentum $p_{\mathrm{T}}^{\mathrm{track}}$, pseudorapidity η^{track}, and azimuth angle ϕ^{track}. Since the most of tracks are charged pions, we suppose the mass of the tracks is 139.6 MeV in this analysis. Only tracks passing established track selection quality criteria are used.
- Event centrality in PbPb collisions (definition in Sec. 2.2). Centrality range 0–80% is divided into 8 equidistant bins, so each PbPb event is characterized by one of the centrality bins: 0 – 10%, 10 – 20%, ..., 70 – 80%.
- Event run number (listed in Sec. 3.1).
- Activated trigger, corresponding to the leading-jet p_{T} according to Tab. 3.1 and 3.2. Information about the activated trigger together with the event run number is used to obtain the trigger prescale correction accounting for the effect that some triggers sample only a fraction of total luminosity.

4.1 Calorimetric-Jet Spectra

The first step of the analysis is to construct calorimetric-jet spectra, which means the dependence of the differential cross-section $\frac{\mathrm{d}^2\sigma}{\mathrm{d}p_{\mathrm{T}}\mathrm{d}y}$ on $p_{\mathrm{T}}^{\mathrm{jet}}$. Kinematic quantities of the calorimetric jets are obtained directly from the tree. Only jets with pseudorapidity $|\eta^{\mathrm{jet}}| < 1.9$ are selected, since within the further analysis also tracks are clustered into jets with radius 0.6, and the pseudorapidity range of the ID is $|\eta| < 2.5$. The jet spectrum is constructed for both pp and PbPb collisions for various centralities. Jet-spectra histograms are corrected for the prescale computed from the activated trigger and the event run number as mentioned above. To get the differential cross-section, the spectra are then divided by corresponding luminosity (luminosity is different for pp and PbPb collisions) and normalized by the number of events corresponding to a given centrality interval, bin width, and the jet pseudorapidity range. The calorimetric-jet spectra are displayed in Fig. 4.1. The spectra have the shape of an exponentially decreasing function, which is expected. Furthermore, R_{AA} distributions are constructed for the calorimetric-jet spectra, which are shown in Fig. 4.2. As mentioned in Sec. 2.3, the measured values of R_{AA}should be less than 1 in HI collisions. However, the values of R_{AA} are greater than 1 for low $p_{\mathrm{T}}^{\mathrm{jet}}$ in central collisions (0 – 10%). The reason is that there is a contribution of fake jets due to the large UE fluctuations [2].

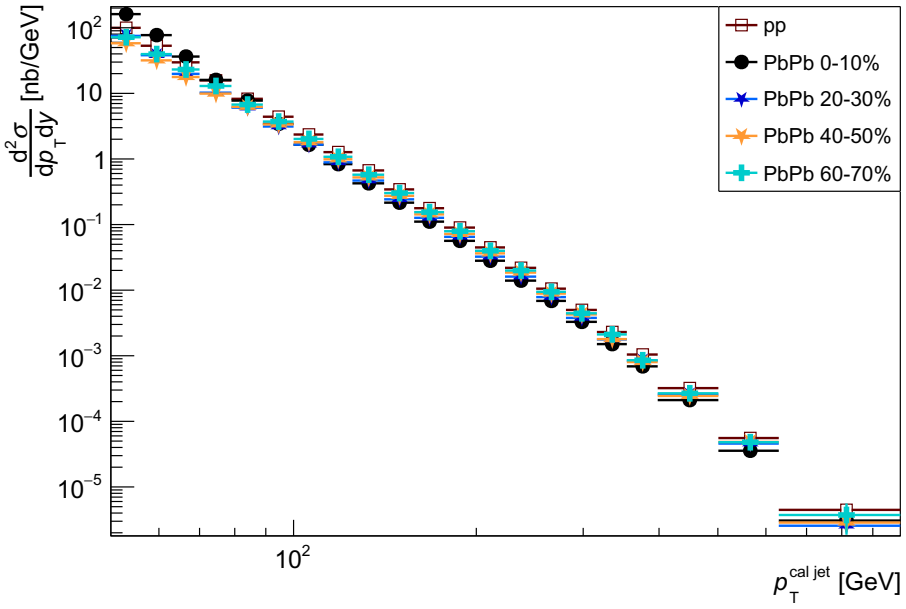

Figure 4.1: Spectrum of $R = 0.4$ anti-k_t calorimetric jets with $|\eta^{jet}| < 1.9$ for pp and PbPb collisions for centrality bins 0 – 10%, 20 – 30%, 40 – 50%, and 60 – 70%. Only statistical errors are presented.

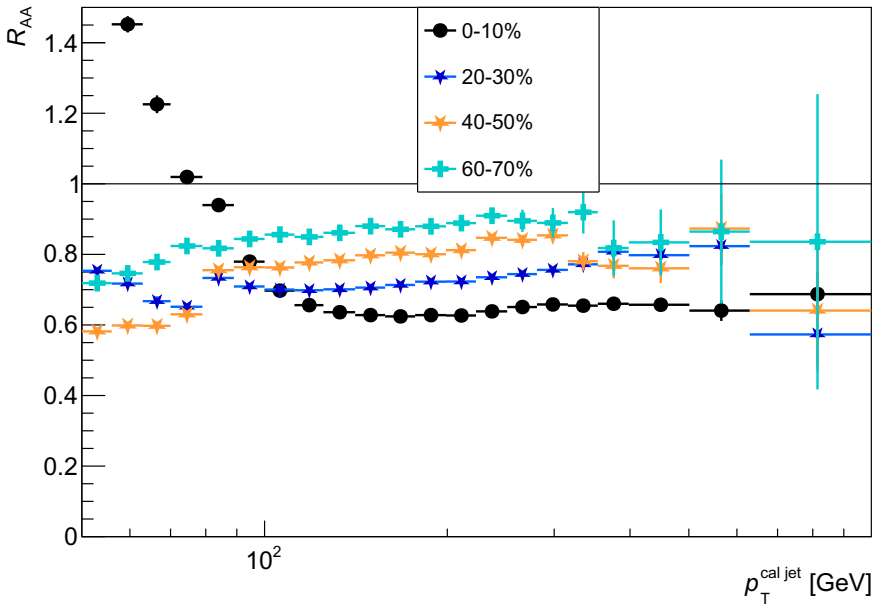

Figure 4.2: R_{AA} distribution of $R = 0.4$ anti-k_t calorimetric jets with $|\eta^{jet}| < 1.9$ for centrality bins 0 – 10%, 20 – 30%, 40 – 50%, and 60 – 70%. Only statistical errors are presented. The value of 1 is marked by a grey line.

4.2 Track-Jet Spectra

The next step is to cluster tracks into jets. Again, the anti-k_t algorithm is used. One of the aims of this thesis is to investigate track-jet spectra behavior for various jet radii. Thus, the clustering is performed for radii 0.2, 0.4, and 0.6. Another parameter that can be varied is p_T^{cut} on tracks, discussed in Sec. 2.4. The track-jet spectra are constructed for the values of p_T^{cut}: 1 GeV, 2 GeV, 3 GeV,

4 GeV, 5 GeV, and 6 GeV.

Before the clustering, track selection is performed. First of all, the tracks with $p_{\mathrm{T}}^{\mathrm{track}} > p_{\mathrm{T}}^{\mathrm{cut}}$ are selected. However, there is a residual contribution of fake tracks, so a fake-elimination procedure is needed to perform. If $p_{\mathrm{T}}^{\mathrm{track}} > 30$ GeV, the following two conditions have to be satisfied:

- The track must match to any calorimetric jet with $p_{\mathrm{T}}^{\mathrm{jet}} > p_{\mathrm{T}}^{\mathrm{cut}}$. In other words, the distance between the track and the calorimetric jet must be less than 0.4.

- Transverse momentum of the track must be less than the transverse momentum of a jet that the track matches to $p_{\mathrm{T}}^{\mathrm{jet\ match}}$ multiplied by a factor f, so $p_{\mathrm{T}}^{\mathrm{track}} < f p_{\mathrm{T}}^{\mathrm{jet\ match}}$. This factor is computed from the formula

$$f = 1 + \sqrt{(3\sigma_{\mathrm{JER}})^2 + (3\sigma_{\mathrm{TMR}})^2}, \tag{4.1}$$

  where $\sigma_{\mathrm{JER}} = 0.15$ and $\sigma_{\mathrm{TMR}} = 0.15$[1].

The tracks with $p_{\mathrm{T}}^{\mathrm{track}} > 30$ GeV that do not satisfy these conditions are excluded. After the fake-elimination procedure, the tracks are clustered with the anti-k_t algorithm for various jet radii. Again, only jets with pseudorapidity $|\eta^{\mathrm{jet}}| < 1.9$ are selected, and the jet spectra are corrected for the prescale and normalized in the same way as the calorimetric jets.

Track-jet spectra for pp and PbPb collisions for various centrality bins, various jet radii, and various $p_{\mathrm{T}}^{\mathrm{cut}}$ are displayed in Figures 4.3, 4.4, and 4.5. The corresponding R_{AA} distributions are shown in Figures 4.6, 4.7, and 4.8. Track-jet spectra are exponentially decreasing and most of them have similar shapes. However, there are some exceptions for those where $p_{\mathrm{T}}^{\mathrm{cut}}$ of 1 GeV and 2 GeV are used. The reason is that a significant portion of the background is also included in the clustering. More of the background is clustered, if: $p_{\mathrm{T}}^{\mathrm{cut}}$ decreases, or the jet radius increases, or $p_{\mathrm{T}}^{\mathrm{jet}}$ decreases, and the more central the PbPb collisions are. In most R_{AA} distributions one can see that the more central the collisions are, the values of R_{AA} are smaller, which means that the jets are suppressed more. For higher $p_{\mathrm{T}}^{\mathrm{jet}}$, statistical fluctuations occur mainly for peripheral collisions. As mentioned above, a significant portion of the background is clustered for lower values of $p_{\mathrm{T}}^{\mathrm{cut}}$, which is manifested as the divergence of R_{AA} distributions at low $p_{\mathrm{T}}^{\mathrm{jet}}$ for central PbPb collisions, see Figures 4.7a, 4.8a, and 4.8b. In general, one can see that the values of R_{AA} of track-jets (except for the cases with a significant UE contribution) are lower than in the case of calorimetric jets with corresponding centrality (Figures 4.7 and 4.2).

[1] The values of σ_{JER} and σ_{TMR} are the first guess.

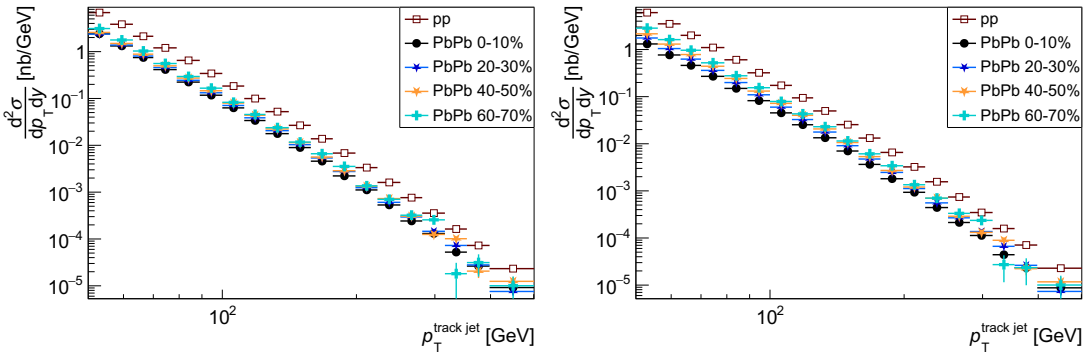

(a) $p_T^{cut} = 1$ GeV

(b) $p_T^{cut} = 2$ GeV

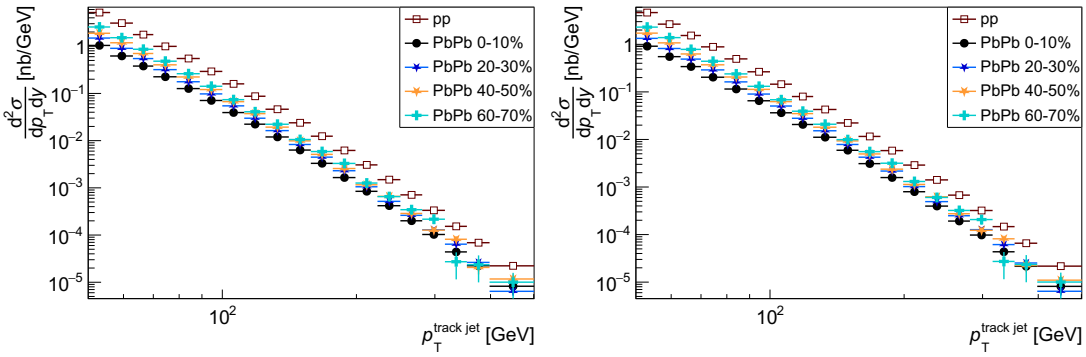

(c) $p_T^{cut} = 3$ GeV

(d) $p_T^{cut} = 4$ GeV

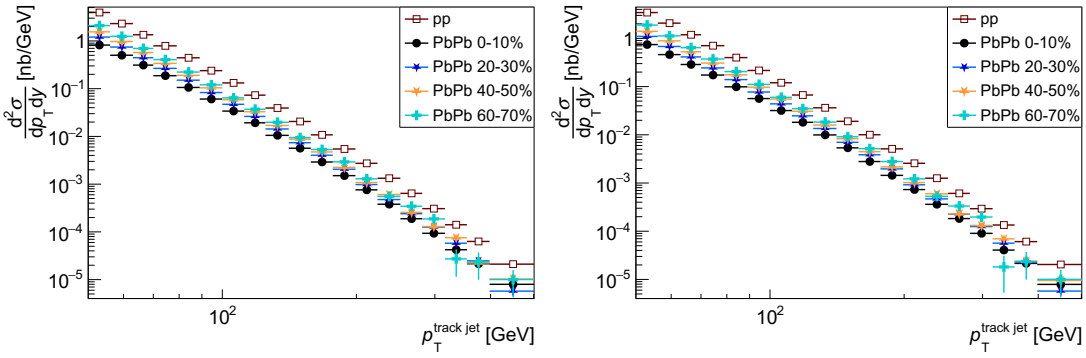

(e) $p_T^{cut} = 5$ GeV

(f) $p_T^{cut} = 6$ GeV

Figure 4.3: Track-jet spectra with $|\eta^{jet}| < 1.9$ and radius $R = 0.2$ for pp and PbPb collisions for centrality bins 0 – 10%, 20 – 30%, 40 – 50%, and 60 – 70%. The individual subplots are made for various p_T^{cut} on tracks. Only statistical errors are presented.

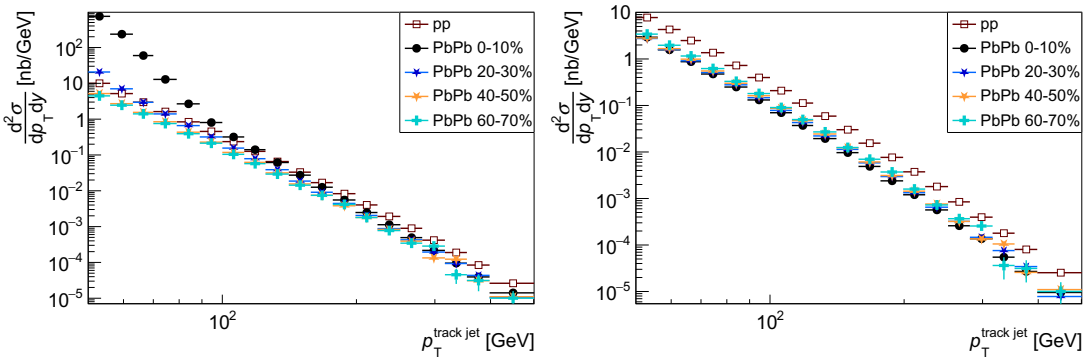

(a) $p_{\mathrm{T}}^{\mathrm{cut}} = 1$ GeV

(b) $p_{\mathrm{T}}^{\mathrm{cut}} = 2$ GeV

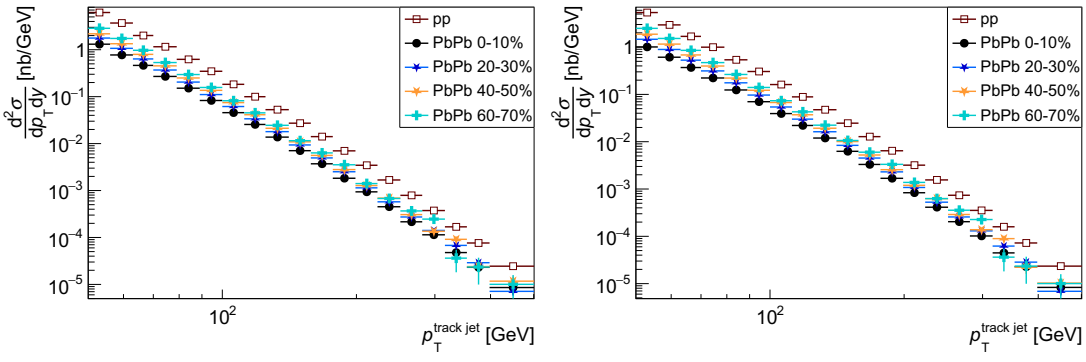

(c) $p_{\mathrm{T}}^{\mathrm{cut}} = 3$ GeV

(d) $p_{\mathrm{T}}^{\mathrm{cut}} = 4$ GeV

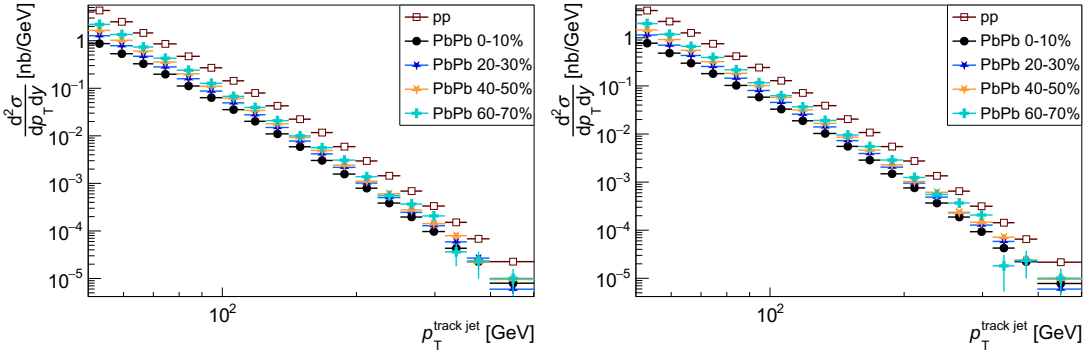

(e) $p_{\mathrm{T}}^{\mathrm{cut}} = 5$ GeV

(f) $p_{\mathrm{T}}^{\mathrm{cut}} = 6$ GeV

Figure 4.4: Track-jet spectra with $|\eta^{\mathrm{jet}}| < 1.9$ and radius $R = 0.4$ for pp and PbPb collisions for centrality bins 0 – 10%, 20 – 30%, 40 – 50%, and 60 – 70%. The individual subplots are made for various $p_{\mathrm{T}}^{\mathrm{cut}}$ on tracks. Only statistical errors are presented.

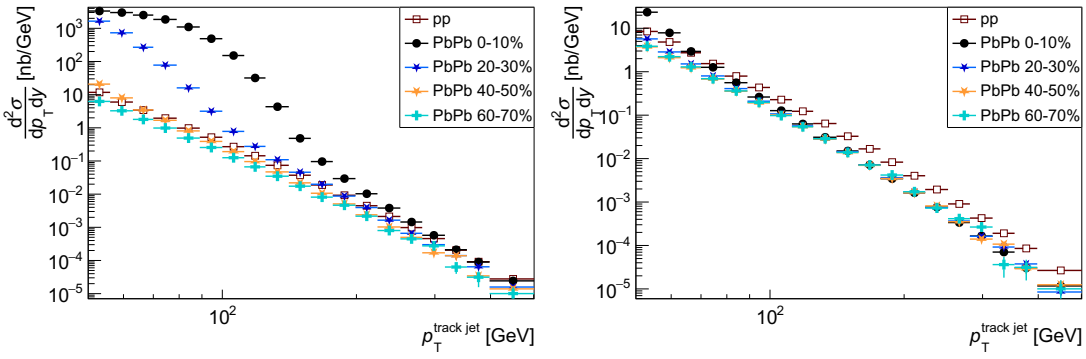

(a) $p_T^{cut} = 1$ GeV (b) $p_T^{cut} = 2$ GeV

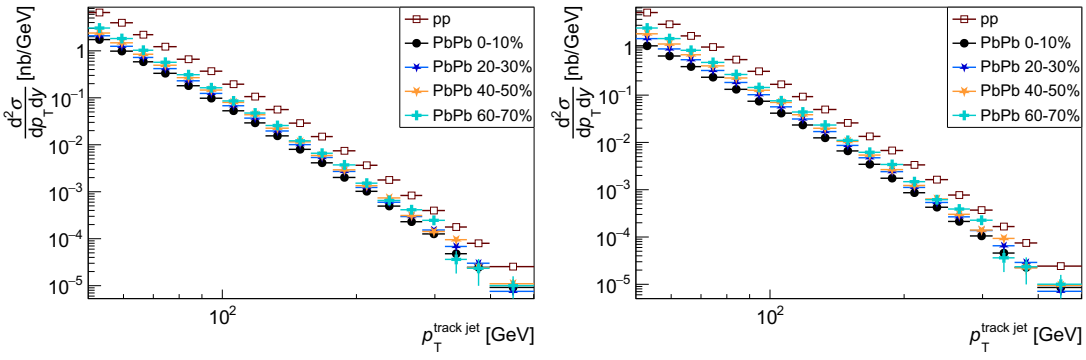

(c) $p_T^{cut} = 3$ GeV (d) $p_T^{cut} = 4$ GeV

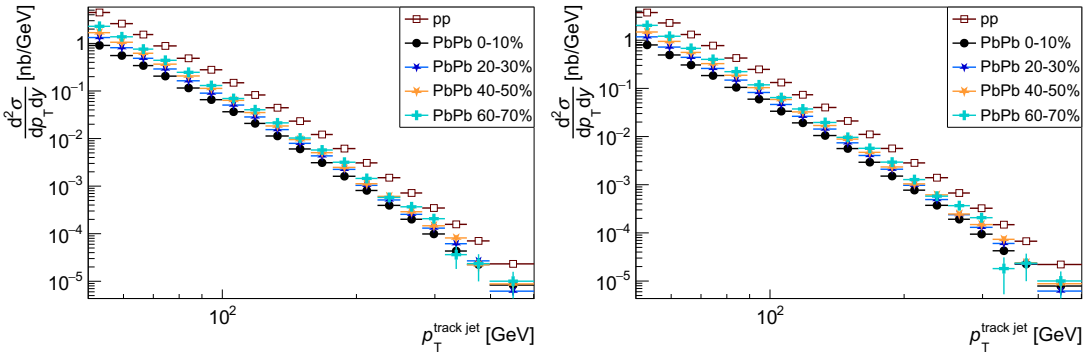

(e) $p_T^{cut} = 5$ GeV (f) $p_T^{cut} = 6$ GeV

Figure 4.5: Track-jet spectra with $|\eta^{jet}| < 1.9$ and radius $R = 0.6$ for pp and PbPb collisions for centrality bins 0 – 10%, 20 – 30%, 40 – 50%, and 60 – 70%. The individual subplots are made for various p_T^{cut} on tracks. Only statistical errors are presented.

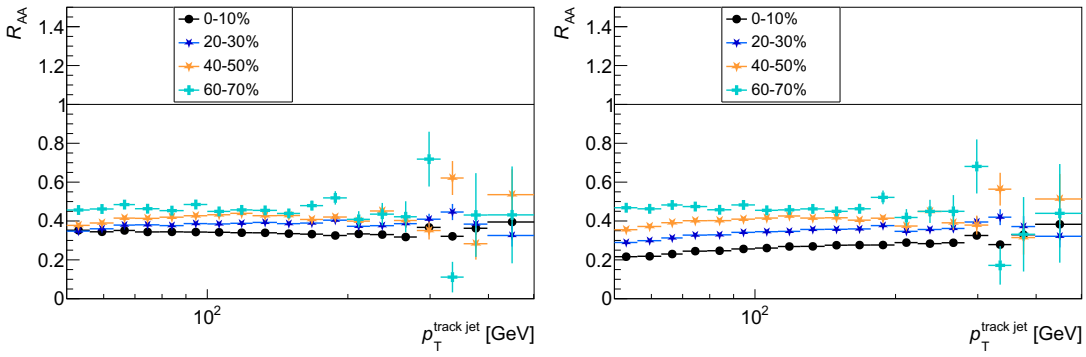

(a) $p_{\mathrm{T}}^{\mathrm{cut}} = 1$ GeV (b) $p_{\mathrm{T}}^{\mathrm{cut}} = 2$ GeV

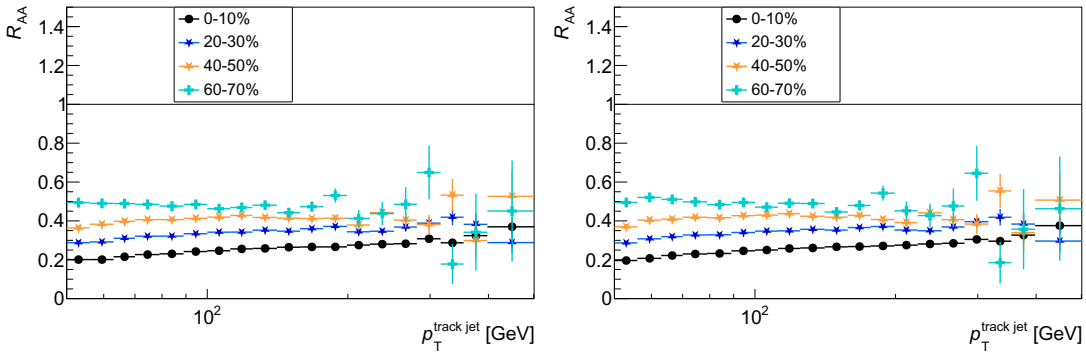

(c) $p_{\mathrm{T}}^{\mathrm{cut}} = 3$ GeV (d) $p_{\mathrm{T}}^{\mathrm{cut}} = 4$ GeV

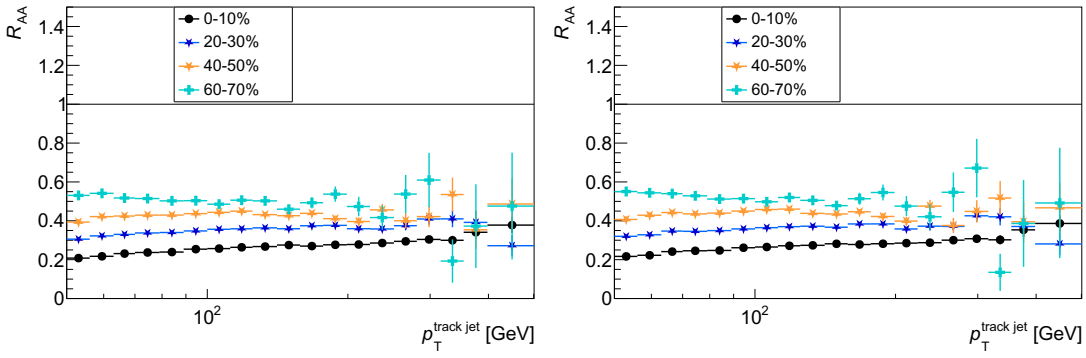

(e) $p_{\mathrm{T}}^{\mathrm{cut}} = 5$ GeV (f) $p_{\mathrm{T}}^{\mathrm{cut}} = 6$ GeV

Figure 4.6: R_{AA} distributions from track-jet spectra with $|\eta^{\mathrm{jet}}| < 1.9$ and radius $R = 0.2$ for centrality bins 0 – 10%, 20 – 30%, 40 – 50%, and 60 – 70%. The individual subplots are made for various $p_{\mathrm{T}}^{\mathrm{cut}}$ on tracks. Only statistical errors are presented. The value of 1 is marked by a grey line.

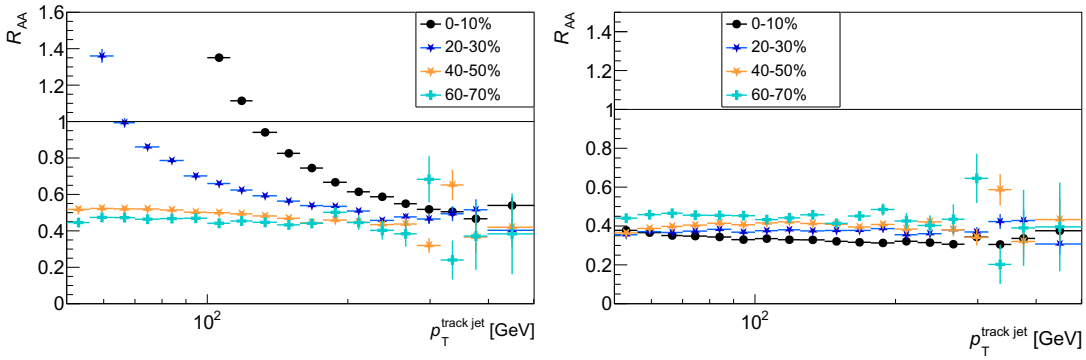

(a) $p_T^{cut} = 1$ GeV (b) $p_T^{cut} = 2$ GeV

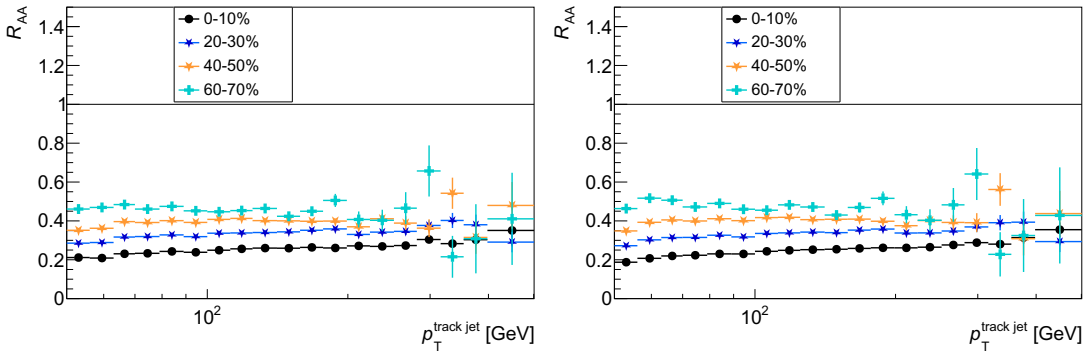

(c) $p_T^{cut} = 3$ GeV (d) $p_T^{cut} = 4$ GeV

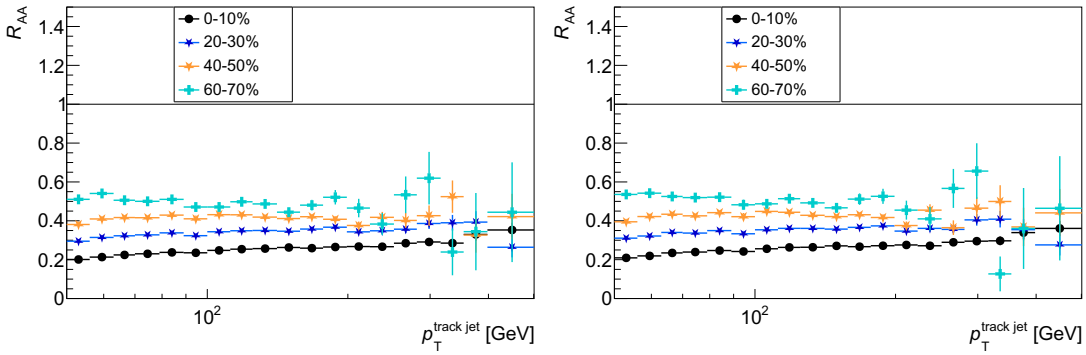

(e) $p_T^{cut} = 5$ GeV (f) $p_T^{cut} = 6$ GeV

Figure 4.7: R_{AA} distributions from track-jet spectra with $|\eta^{jet}| < 1.9$ and radius $R = 0.4$ for centrality bins 0 – 10%, 20 – 30%, 40 – 50%, and 60 – 70%. The individual subplots are made for various p_T^{cut} on tracks. Only statistical errors are presented. The value of 1 is marked by a grey line.

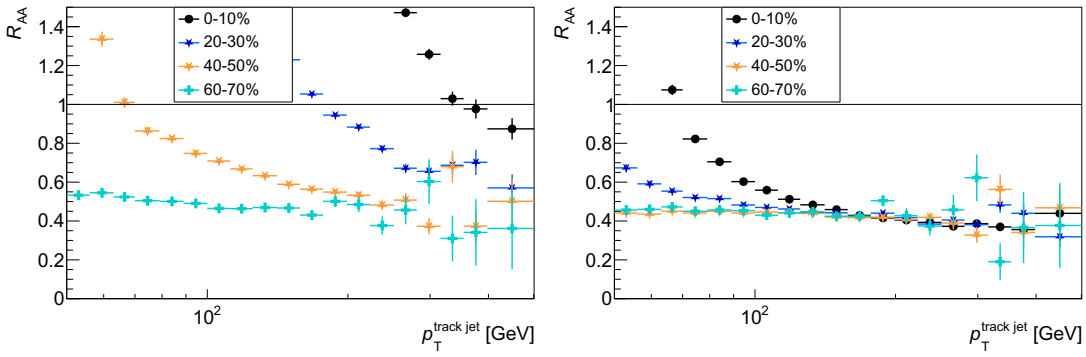

(a) $p_T^{cut} = 1$ GeV (b) $p_T^{cut} = 2$ GeV

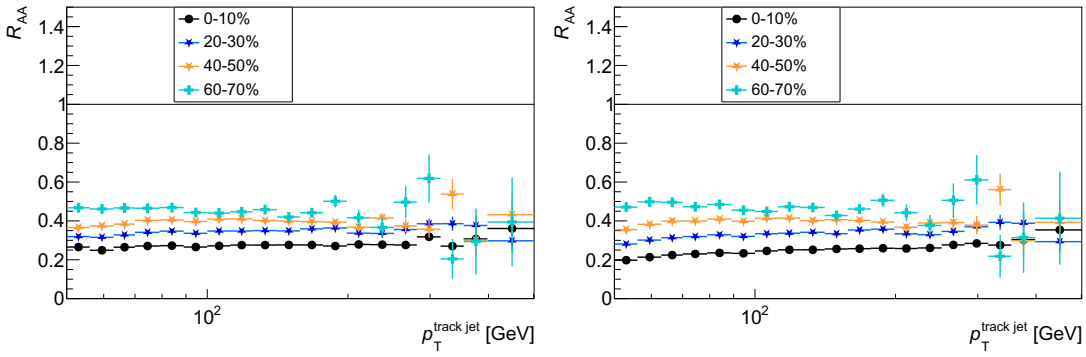

(c) $p_T^{cut} = 3$ GeV (d) $p_T^{cut} = 4$ GeV

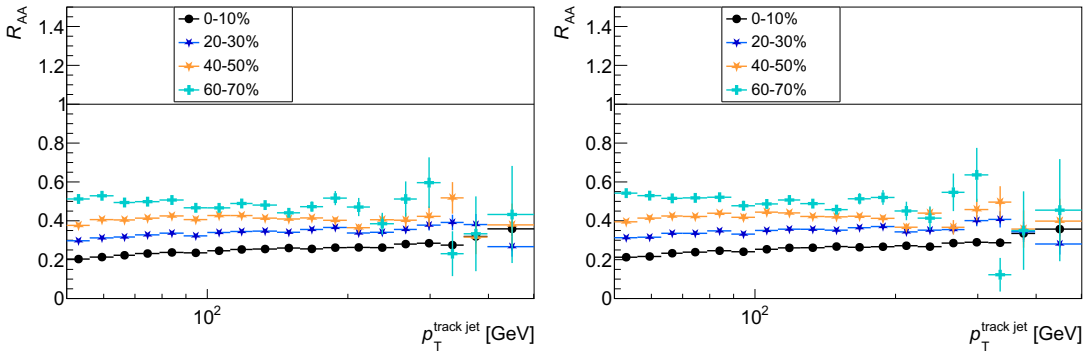

(e) $p_T^{cut} = 5$ GeV (f) $p_T^{cut} = 6$ GeV

Figure 4.8: R_{AA} distributions from track-jet spectra with $|\eta^{jet}| < 1.9$ and radius $R = 0.6$ for centrality bins 0 – 10%, 20 – 30%, 40 – 50%, and 60 – 70%. The individual subplots are made for various p_T^{cut} on tracks. Only statistical errors are presented. The value of 1 is marked by a grey line.

Consequently, the R_{AA} double ratio distributions are constructed, namely $\frac{R_{\mathrm{AA}}(0.4)}{R_{\mathrm{AA}}(0.2)}$ and $\frac{R_{\mathrm{AA}}(0.6)}{R_{\mathrm{AA}}(0.2)}$ for various values of $p_{\mathrm{T}}^{\mathrm{cut}}$ on tracks. The double ratios for central PbPb collisions (0 – 10%) are displayed in Fig. 4.9. In the individual subplots, $p_{\mathrm{T}}^{\mathrm{cut}}$ is fixed, but R in the numerator varies. For $p_{\mathrm{T}}^{\mathrm{cut}} = 1$ GeV and 2 GeV, the results are affected by large background. The background is present more in jets with $R = 0.6$ than those with $R = 0.4$. If $p_{\mathrm{T}}^{\mathrm{cut}} = 3$ GeV, the values in the plot are greater than 1 (up to 1.6 for $R = 0.6$) for lower $p_{\mathrm{T}}^{\mathrm{jet}}$. For the other values of $p_{\mathrm{T}}^{\mathrm{cut}}$, the values in the distribution are close to 1. Another option is to fix R in the numerator and vary the $p_{\mathrm{T}}^{\mathrm{cut}}$. Such an option is applied within the individual subplots in Fig. 4.10.

4.3 Correspondence between the Calorimetric and Track Jets

In the previous paragraphs, the construction of calorimetric and track-jet spectra, and their R_{AA} distributions was described. In the next step, the correlation between their transverse momenta is investigated. Namely, 2D histograms (correlation matrices) $p_{\mathrm{T}}^{\text{track jet}}$ versus $p_{\mathrm{T}}^{\text{cal jet}}$ for pp and PbPb collisions for various centralities, jet radii R of track jets (calorimetric jets have always $R = 0.4$), and $p_{\mathrm{T}}^{\mathrm{cut}}$ on tracks are constructed. From each event, a list of calorimetric and track jets with $|\eta^{\mathrm{jet}}| < 1.9$ is created. The algorithm matches the corresponding calorimetric and track jets as follows:

1. A list of all distances in the $\eta - \phi$ space between the i-th calorimetric and the j-th track jet ΔR_{ij} is created.
2. A minimal distance $\Delta R_{ij}^{\mathrm{min}}$ is calculated, and the corresponding indices i_{min} and j_{min} are stored.
3. The condition $\Delta R_{ij}^{\mathrm{min}} < 0.75R$ is checked.
4. If the condition is satisfied, the match is found. Consequently, this pair is removed from the list and the algorithm moves to step 1 and all procedure is repeated as long as the condition in step 3 holds.

In the ideal case, the correlation matrix between p_{T} of calorimetric and track jets would be perfectly diagonal. However, in reality, the following effects modify the correlation matrix:

- The calorimetric jets contain also neutral particles, whereas the track jets are formed by charged particles only. This effect decreases p_{T} of the track jet with respect to the matched calorimetric jet.
- The calorimetric jets are deprived of the UE, whereas the track jets are not. The UE increases p_{T} of track jets. This effect is significant mainly in central events for low values of $p_{\mathrm{T}}^{\mathrm{cut}}$ and large jet radius R.
- Imperfect tracking efficiency decreases p_{T} of track jets.
- Fake tracks increase p_{T} of track jets.

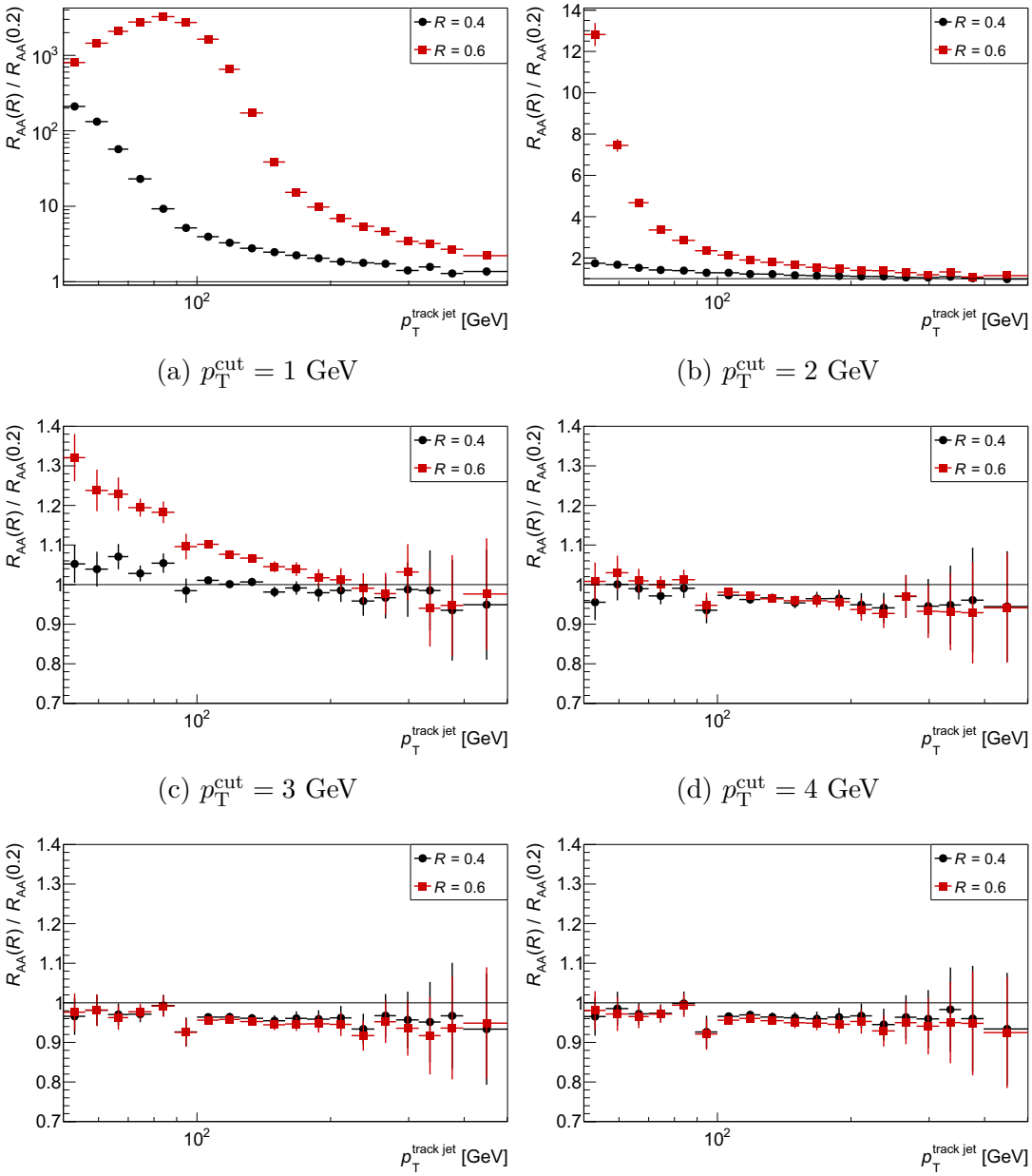

(a) $p_{\mathrm{T}}^{\mathrm{cut}} = 1$ GeV (b) $p_{\mathrm{T}}^{\mathrm{cut}} = 2$ GeV

(c) $p_{\mathrm{T}}^{\mathrm{cut}} = 3$ GeV (d) $p_{\mathrm{T}}^{\mathrm{cut}} = 4$ GeV

(e) $p_{\mathrm{T}}^{\mathrm{cut}} = 5$ GeV (f) $p_{\mathrm{T}}^{\mathrm{cut}} = 6$ GeV

Figure 4.9: R_{AA} double ratio distributions $\frac{R_{\mathrm{AA}}(0.4)}{R_{\mathrm{AA}}(0.2)}$ and $\frac{R_{\mathrm{AA}}(0.6)}{R_{\mathrm{AA}}(0.2)}$ from track-jet spectra with $|\eta^{\mathrm{jet}}| < 1.9$ and for centrality bin 0 – 10%. The individual subplots are made for various $p_{\mathrm{T}}^{\mathrm{cut}}$ on tracks. Only statistical errors are presented. The value of 1 is marked by a grey line.

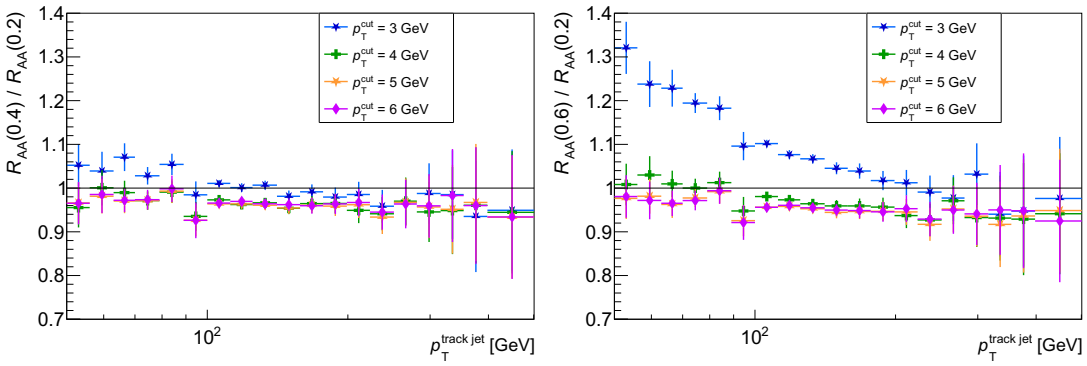

Figure 4.10: R_{AA} double ratio distributions $\frac{R_{\mathrm{AA}}(0.4)}{R_{\mathrm{AA}}(0.2)}$ (left) and $\frac{R_{\mathrm{AA}}(0.6)}{R_{\mathrm{AA}}(0.2)}$ (right) from track-jet spectra with $|\eta^{\mathrm{jet}}| < 1.9$ and for centrality bin 0 – 10% for the values of $p_{\mathrm{T}}^{\mathrm{cut}}$ on tracks 3 GeV, 4 GeV, 5 GeV, and 6 GeV. Only statistical errors are presented. The value of 1 is marked by a grey line.

- Momentum resolution is different for calorimetric and track jets.

The above effects can be seen in the correlation matrices in Figures 4.11 and 4.12. The figures contain two sets of the correlation matrices for track-jet radii and $p_{\mathrm{T}}^{\mathrm{cut}}$ on tracks: $R = 0.2$ with $p_{\mathrm{T}}^{\mathrm{cut}} = 6$ GeV (small jets with large $p_{\mathrm{T}}^{\mathrm{cut}}$), and $R = 0.6$ with $p_{\mathrm{T}}^{\mathrm{cut}} = 1$ GeV (large jets with small $p_{\mathrm{T}}^{\mathrm{cut}}$), respectively.

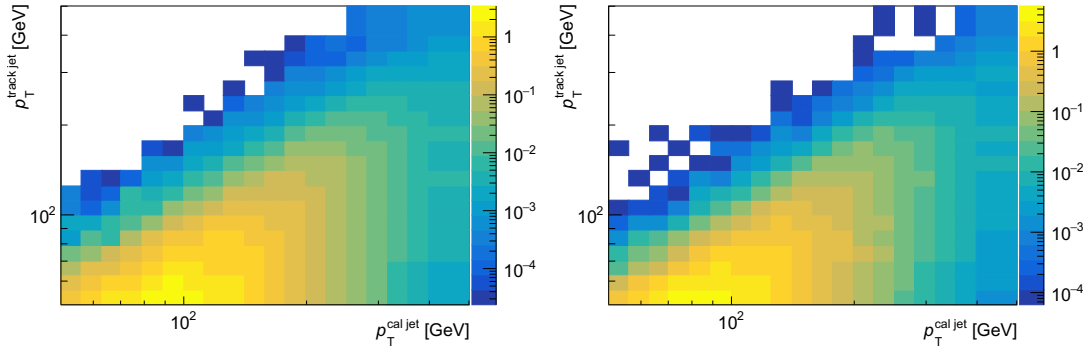

(a) PbPb 0 – 10%

(b) PbPb 20 – 30%

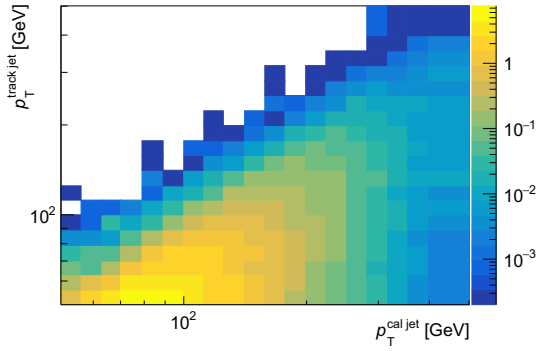

(c) PbPb 40 – 50%

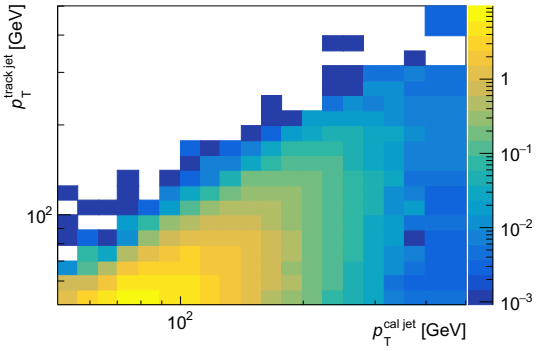

(d) PbPb 60 – 70%

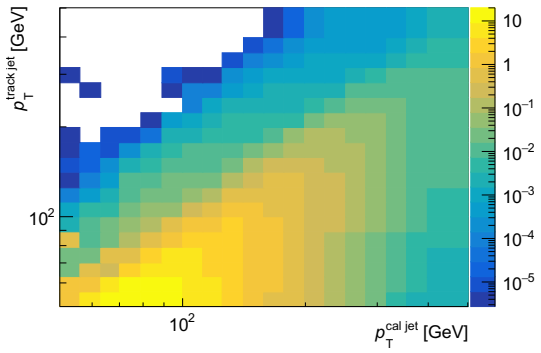

(e) pp

Figure 4.11: Correlation plots between the calorimetric and track-jet p_{T}, both reconstructed with anti-k_t algorithm and pseudorapidity $|\eta^{\mathrm{jet}}| < 1.9$. Calorimetric jets have $R = 0.4$, whereas the track jets have $R = 0.2$ and $p_{\mathrm{T}}^{\mathrm{cut}} = 6$ GeV. The plots in the first two rows correspond to PbPb collisions for various centrality bins, the bottom plot corresponds to pp collisions.

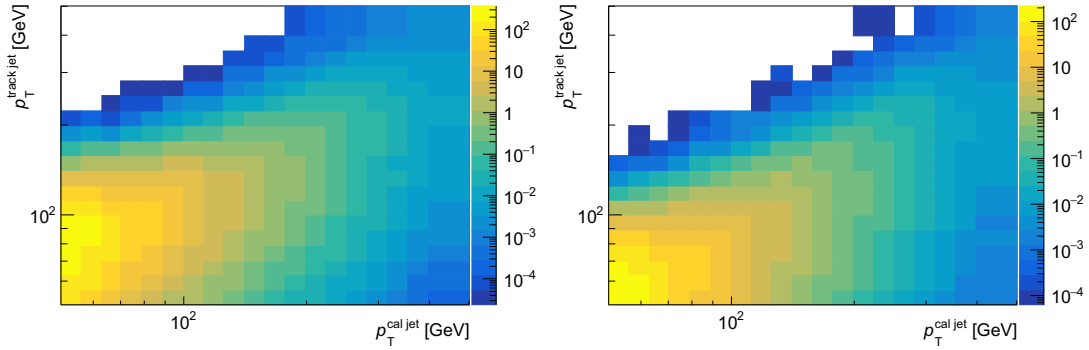

(a) PbPb 0 – 10%

(b) PbPb 20 – 30%

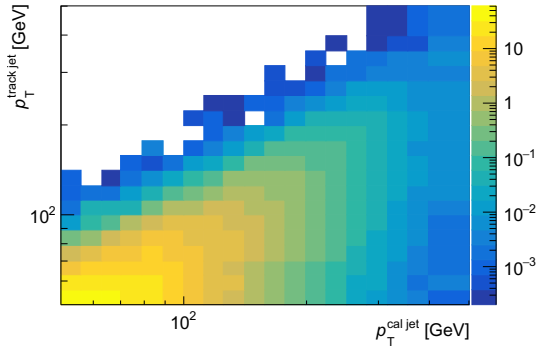

(c) PbPb 40 – 50%

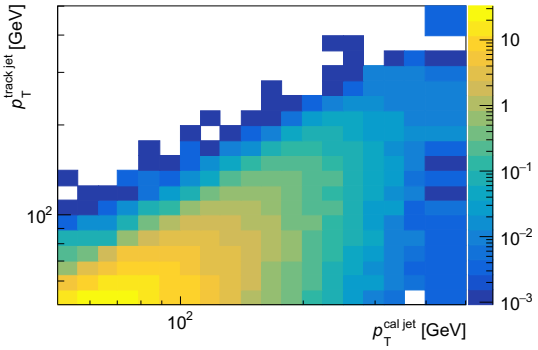

(d) PbPb 60 – 70%

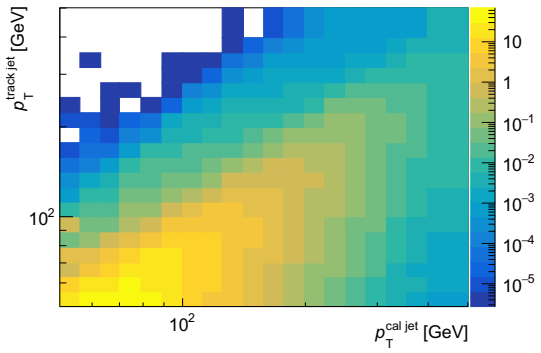

(e) pp

Figure 4.12: Correlation plots between the calorimetric and track-jet p_{T}, both reconstructed with anti-k_t algorithm and pseudorapidity $|\eta^{\mathrm{jet}}| < 1.9$. Calorimetric jets have $R = 0.4$, whereas the track jets have $R = 0.6$ and $p_{\mathrm{T}}^{\mathrm{cut}} = 1$ GeV. The plots in the first two rows correspond to PbPb collisions for various centrality bins, the bottom plot corresponds to pp collisions.

5. MC Data Processing

First of all, the data structure is discussed, similarly as in the introduction of Chap. 4. The observables are also organized in the tree. In addition to all the observables discussed in Chap. 4, the following observables for each event are also available:

- Kinematic quantities of truth tracks: transverse momentum $p_{\mathrm{T}}^{\mathrm{truth}}$, pseudo-rapidity η^{truth}, and azimuth angle ϕ^{truth}. The mass of the particles is set to 139.6 MeV (the mass of a charged pion).
- MC weight w_{MC} . As mentioned in Sec. 3.4, the data are divided into 5 JZ slices according to the transferred momentum in the collision. Each JZ slice has the unique value of MC weight, and it is the same for each event within a certain JZ slice.
- Total transverse energy deposited in the forward calorimeter FCal, denoted $E_{\mathrm{T}}^{\mathrm{FCal}}$. This value is used to get another weight, w_{FCal}. The w_{FCal} is obtained from the histogram in Fig. 5.1. If $E_{\mathrm{T}}^{\mathrm{FCal}} > 4.5$ TeV, then $w_{\mathrm{FCal}} = 1$. The resulting event weight is $w = w_{\mathrm{MC}} \times w_{\mathrm{FCal}}$.

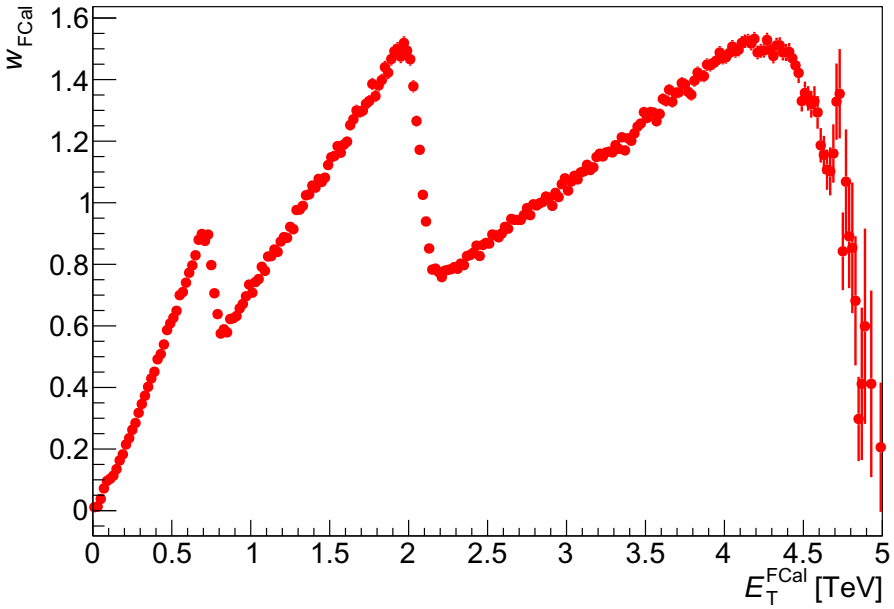

Figure 5.1: Dependence of w_{FCal} on the total transverse energy deposited in the FCal.

5.1 Track-jet Modification

From MC data, track-jet spectra are constructed using the anti-k_t algorithm in a similar way as in the case of experimental data (various centrality bins, various jet radii, and various values of $p_{\mathrm{T}}^{\mathrm{cut}}$ are considered). The spectra have a similar shape as those in Figures 4.3, 4.4, and 4.5. So instead of spectra, the corresponding R_{AA}

are rather displayed in Figures 5.2, 5.3, and 5.4. It is very important to mention that MC does not simulate jet quenching, so R_{AA} for truth track jets should be equal to one (in fact, the values slightly fluctuate around 1 due to statistics, see Fig. 5.5). Therefore, the centrality-dependent modification of MC reconstructed jet spectra in PbPb versus pp is caused by background and migration due to momentum resolution, and tracking efficiency. Of course, these effects are also present in experimental data, so it is useful to probe them within MC. Then it is possible to correct experimental jet spectra.

5.2 Track-jet Reconstruction Efficiency

Since we have information about truth tracks in MC, it is possible to use this information to determine the efficiency of track-jet reconstruction. It is determined as a ratio of matched truth-jet spectra to overall truth-jet spectra. The matching means that each truth jet is matched to a compatible reconstructed jet in the sense of minimal ΔR in the $\eta - \phi$ space within each event if such matching exists. The matching procedure is the same as it was in the case of matching the track jets to calorimetric jets in experimental data (see Sec. 4.3). There are displayed two plots of track-jet reconstruction efficiency in this thesis: the first one for jets with $R = 0.2$ and $p_{\mathrm{T}}^{\mathrm{cut}} = 6$ GeV, and the second one for jets with $R = 0.6$ and $p_{\mathrm{T}}^{\mathrm{cut}} = 1$ GeV (Fig. 5.6). In both cases, the efficiency is above 0.9 and it seems that it is generally higher for large jets with a small $p_{\mathrm{T}}^{\mathrm{cut}}$.

5.3 Migration Matrices

Jet migration due to momentum scale and resolution can be expressed via the so-called migration matrix. It is a 2D plot – correlation of reconstructed- vs truth-jet p_{T}. The reconstructed jets are again matched to truth jets in the same way as above. Again, the same two sets of plots of migration matrices are selected: the first one for jets with $R = 0.2$ and $p_{\mathrm{T}}^{\mathrm{cut}} = 6$ GeV (Fig. 5.7), and the second one for jets with $R = 0.6$ and $p_{\mathrm{T}}^{\mathrm{cut}} = 1$ GeV (Fig. 5.8). In the case of an ideal detector and no background, the migration matrices would be diagonal. However, in both sets of plots, one can see that jets migrate due to detector resolution, the presence of fake tracks, and tracking efficiency. In the case of large jets and small $p_{\mathrm{T}}^{\mathrm{cut}}$, there is also present a significant background, especially for central events (Fig. 5.8).

Another type of correlation between the reconstructed and truth jets can be expressed through momentum scale $p_{\mathrm{T}}^{\mathrm{reco}}/p_{\mathrm{T}}^{\mathrm{truth}}$ vs $p_{\mathrm{T}}^{\mathrm{truth}}$ (Figures 5.9 and 5.10). In the case of no background and an ideal detector, the momentum scale $p_{\mathrm{T}}^{\mathrm{reco}}/p_{\mathrm{T}}^{\mathrm{truth}}$ would be equal to 1 for all values of $p_{\mathrm{T}}^{\mathrm{truth}}$. In the Figures 5.9 and 5.10, one can see the effects of imperfect tracking efficiency, detector resolution, and the background. The momentum resolution is much worse in the case of large jets and small $p_{\mathrm{T}}^{\mathrm{cut}}$ than for small jets and large $p_{\mathrm{T}}^{\mathrm{cut}}$ due to the large background, especially in central PbPb collisions. In addition, for both cases, the mean value of the momentum scale $\left\langle p_{\mathrm{T}}^{\mathrm{reco}}/p_{\mathrm{T}}^{\mathrm{truth}} \right\rangle$ as a function of $p_{\mathrm{T}}^{\mathrm{truth}}$ was made (Fig. 5.11). However, for small jets and large $p_{\mathrm{T}}^{\mathrm{cut}}$, $\left\langle p_{\mathrm{T}}^{\mathrm{reco}}/p_{\mathrm{T}}^{\mathrm{truth}} \right\rangle$ is approximately 0.7 in PbPb collisions for all centralities and 0.9 in pp collisions (Fig. 5.11a). This is caused mainly by imperfect tracking efficiency. For large jets and small $p_{\mathrm{T}}^{\mathrm{cut}}$ (Fig. 5.11b),

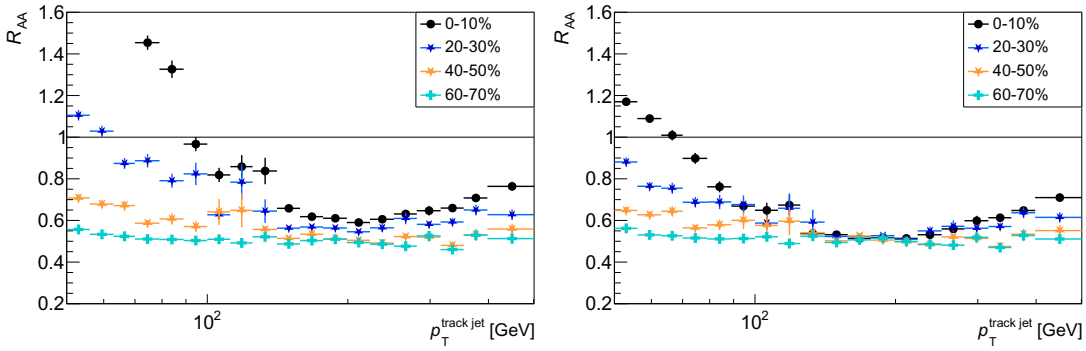

(a) $p_{\mathrm{T}}^{\mathrm{cut}} = 1$ GeV (b) $p_{\mathrm{T}}^{\mathrm{cut}} = 2$ GeV

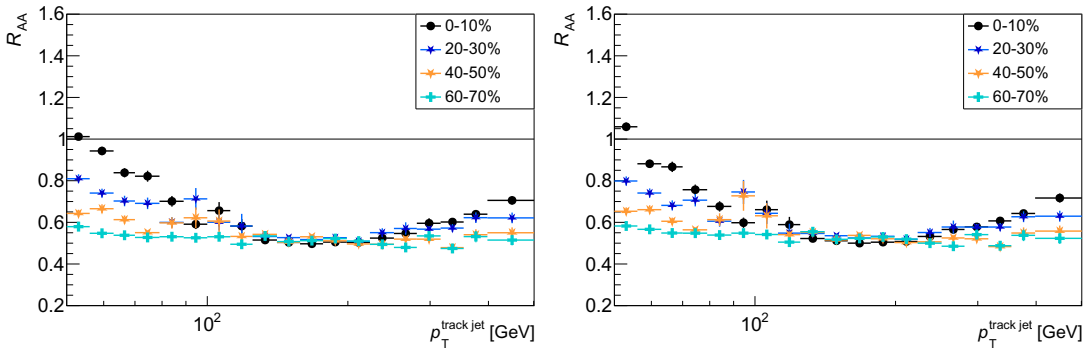

(c) $p_{\mathrm{T}}^{\mathrm{cut}} = 3$ GeV (d) $p_{\mathrm{T}}^{\mathrm{cut}} = 4$ GeV

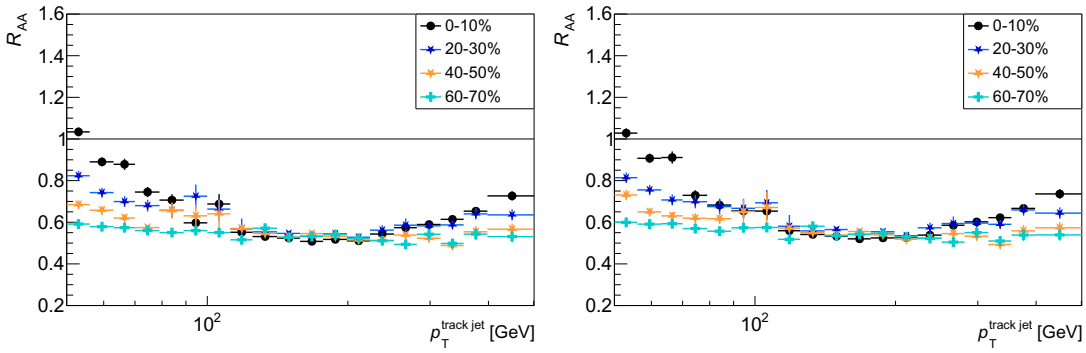

(e) $p_{\mathrm{T}}^{\mathrm{cut}} = 5$ GeV (f) $p_{\mathrm{T}}^{\mathrm{cut}} = 6$ GeV

Figure 5.2: R_{AA} of MC track jets with $|\eta^{\mathrm{jet}}| < 1.9$ and radius $R = 0.2$ for centrality bins 0 – 10%, 20 – 30%, 40 – 50%, and 60 – 70%. The individual subplots are made for various $p_{\mathrm{T}}^{\mathrm{cut}}$ on tracks. Only statistical errors are presented. The value of 1 is marked by a grey line.

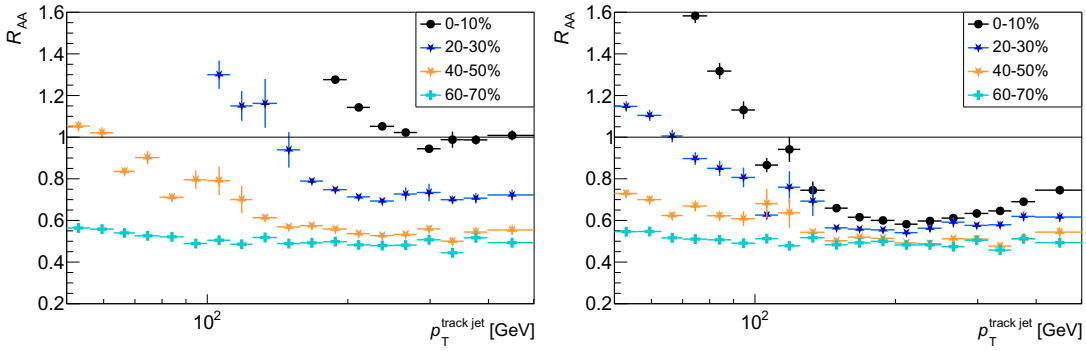

(a) $p_T^{cut} = 1$ GeV (b) $p_T^{cut} = 2$ GeV

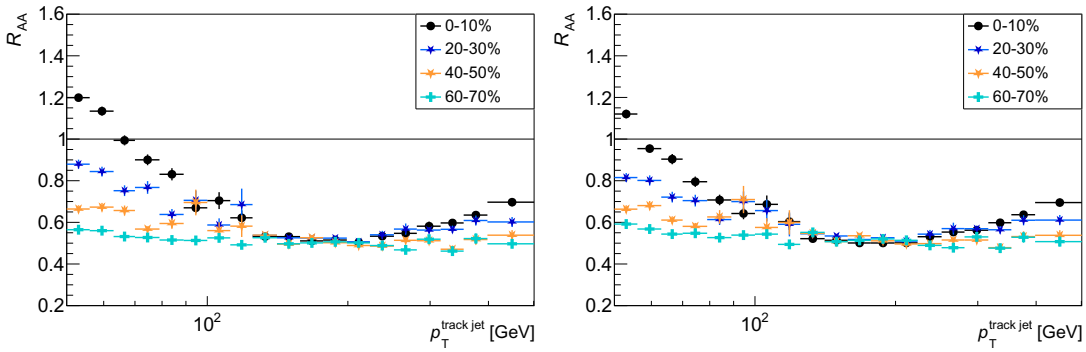

(c) $p_T^{cut} = 3$ GeV (d) $p_T^{cut} = 4$ GeV

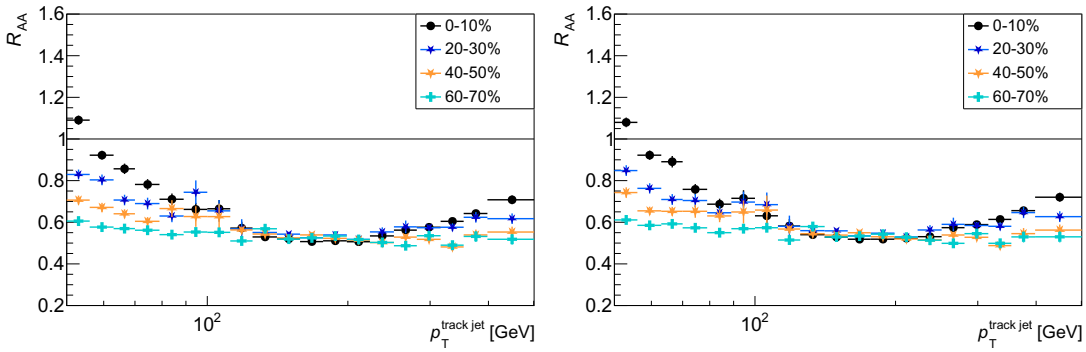

(e) $p_T^{cut} = 5$ GeV (f) $p_T^{cut} = 6$ GeV

Figure 5.3: R_{AA} of MC track jets with $|\eta^{jet}| < 1.9$ and radius $R = 0.4$ for centrality bins 0 – 10%, 20 – 30%, 40 – 50%, and 60 – 70%. The individual subplots are made for various p_T^{cut} on tracks. Only statistical errors are presented. The value of 1 is marked by a grey line.

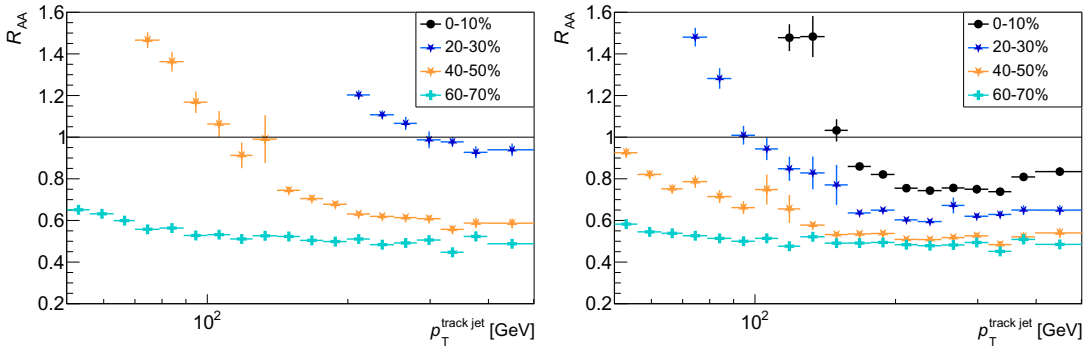

(a) $p_T^{cut} = 1$ GeV (b) $p_T^{cut} = 2$ GeV

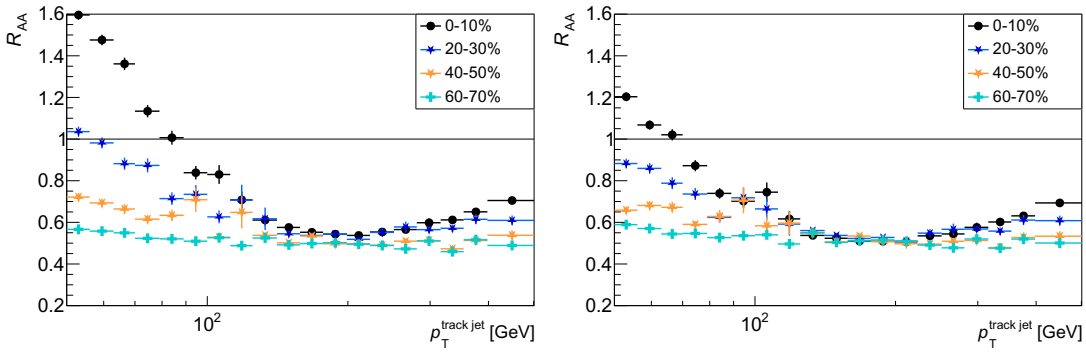

(c) $p_T^{cut} = 3$ GeV (d) $p_T^{cut} = 4$ GeV

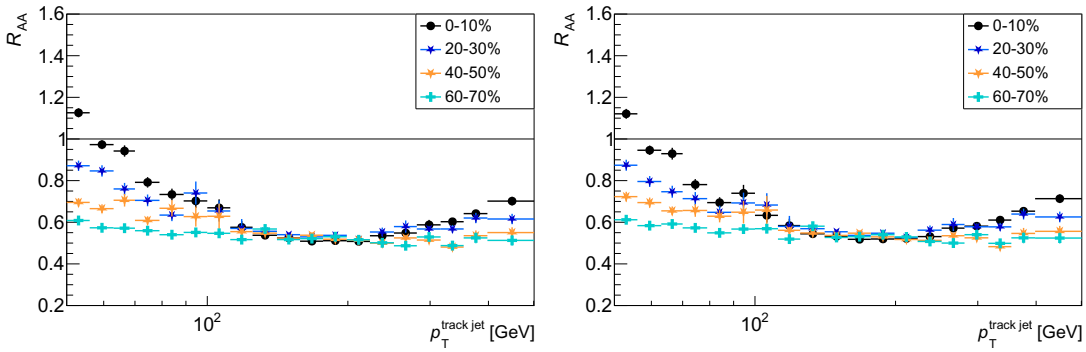

(e) $p_T^{cut} = 5$ GeV (f) $p_T^{cut} = 6$ GeV

Figure 5.4: R_{AA} of MC track jets with $|\eta^{jet}| < 1.9$ and radius $R = 0.6$ for centrality bins 0 – 10%, 20 – 30%, 40 – 50%, and 60 – 70%. The individual subplots are made for various p_T^{cut} on tracks. Only statistical errors are presented. The value of 1 is marked by a grey line.

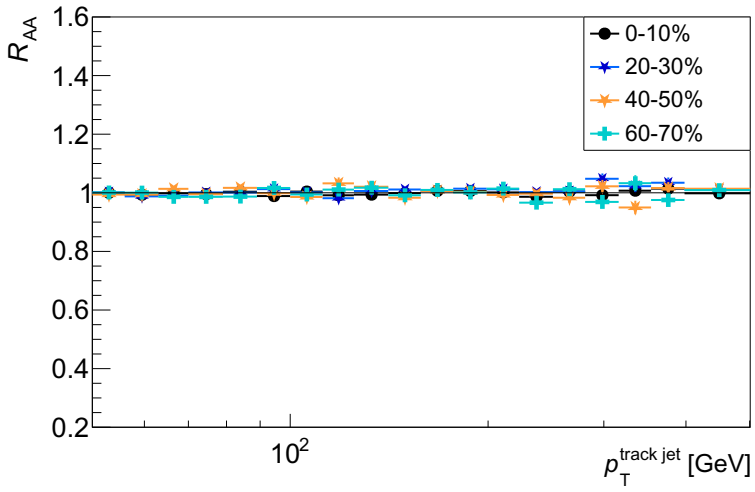

Figure 5.5: R_{AA} of MC true track jets with $|\eta^{jet}| < 1.9$, $R = 0.4$, and $p_T^{cut} = 4$ GeV for centrality bins 0 – 10%, 20 – 30%, 40 – 50%, and 60 – 70%. The value of 1 is marked by a grey line.

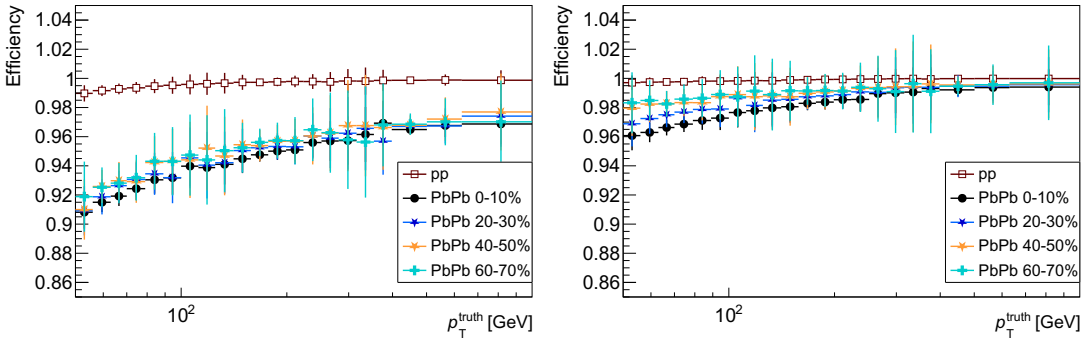

Figure 5.6: Track-jet reconstruction efficiency using MC track jets from pp and PbPb collisions with centrality bins 0 – 10%, 20 – 30%, 40 – 50%, and 60 – 70%. Left: $R = 0.2$ and $p_T^{cut} = 6$ GeV; right: $R = 0.6$ and $p_T^{cut} = 1$ GeV. Only statistical errors are presented. The value of 1 is marked by a grey line.

the values of $\left\langle p_T^{reco}/p_T^{truth} \right\rangle$ are increased due to the large background, especially for central PbPb collisions and low p_T^{jet}.

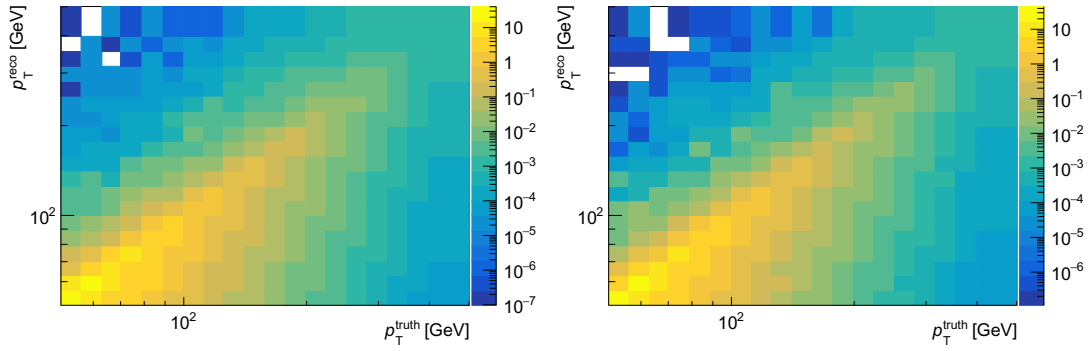

(a) PbPb 0 – 10%

(b) PbPb 20 – 30%

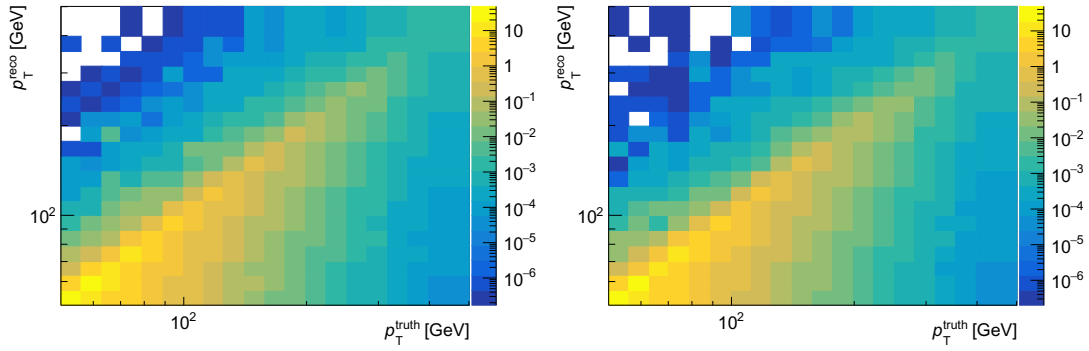

(c) PbPb 40 – 50%

(d) PbPb 60 – 70%

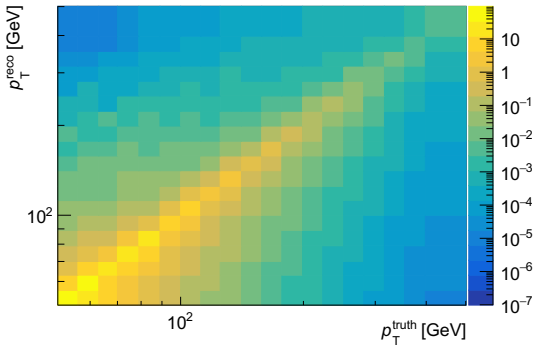

(e) pp

Figure 5.7: Migration matrices for MC track jets with $R = 0.2$, $p_{\mathrm{T}}^{\mathrm{cut}} = 6$ GeV, and pseudorapidity $|\eta^{\mathrm{jet}}| < 1.9$. The plots in the first two rows correspond to PbPb collisions for various centrality bins, the bottom plot corresponds to pp collisions.

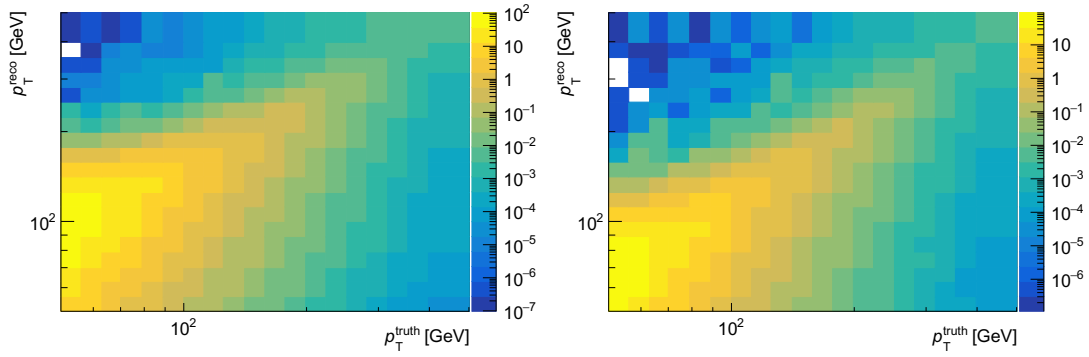

(a) PbPb 0 – 10%

(b) PbPb 20 – 30%

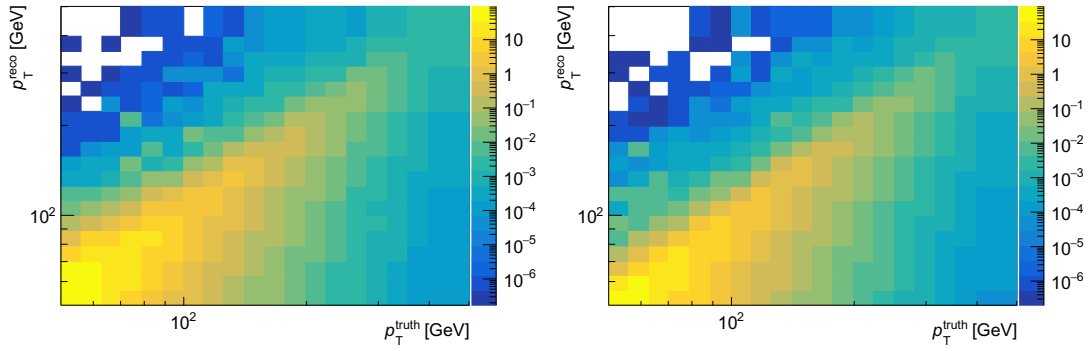

(c) PbPb 40 – 50%

(d) PbPb 60 – 70%

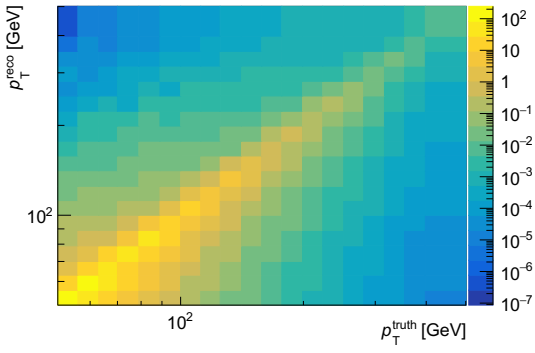

(e) pp

Figure 5.8: Migration matrices for MC track jets with $R = 0.6$, $p_{\mathrm{T}}^{\mathrm{cut}} = 1$ GeV, and pseudorapidity $|\eta^{\mathrm{jet}}| < 1.9$. The plots in the first two rows correspond to PbPb collisions for various centrality bins, the bottom plot corresponds to pp collisions.

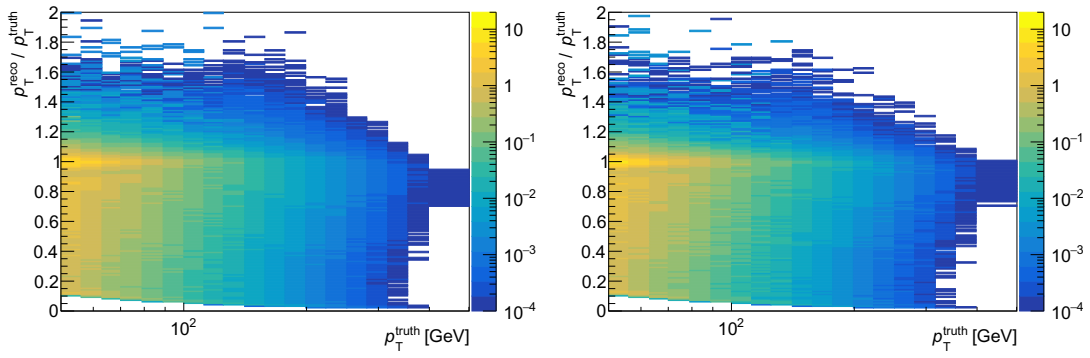

(a) PbPb 0 – 10%

(b) PbPb 20 – 30%

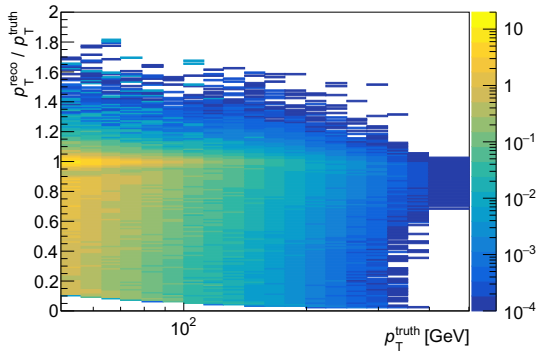

(c) PbPb 40 – 50%

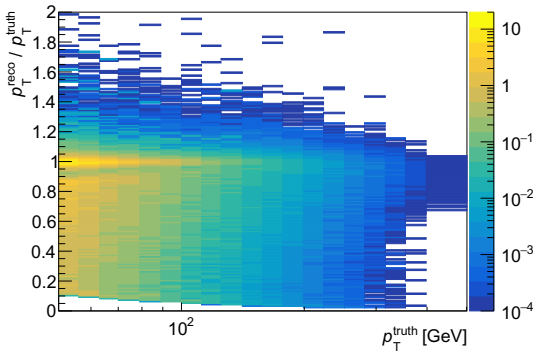

(d) PbPb 60 – 70%

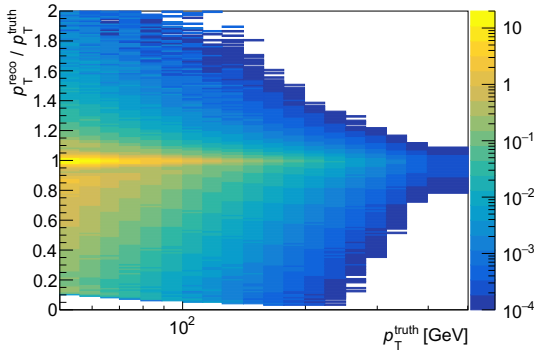

(e) pp

Figure 5.9: Correlation plots $p_{\mathrm{T}}^{\mathrm{reco}}/p_{\mathrm{T}}^{\mathrm{truth}}$ vs $p_{\mathrm{T}}^{\mathrm{truth}}$ of MC track jets with $R = 0.2$, $p_{\mathrm{T}}^{\mathrm{cut}} = 6$ GeV, and pseudorapidity $|\eta^{\mathrm{jet}}| < 1.9$. The plots in the first two rows correspond to PbPb collisions for various centrality bins, the bottom plot corresponds to pp collisions.

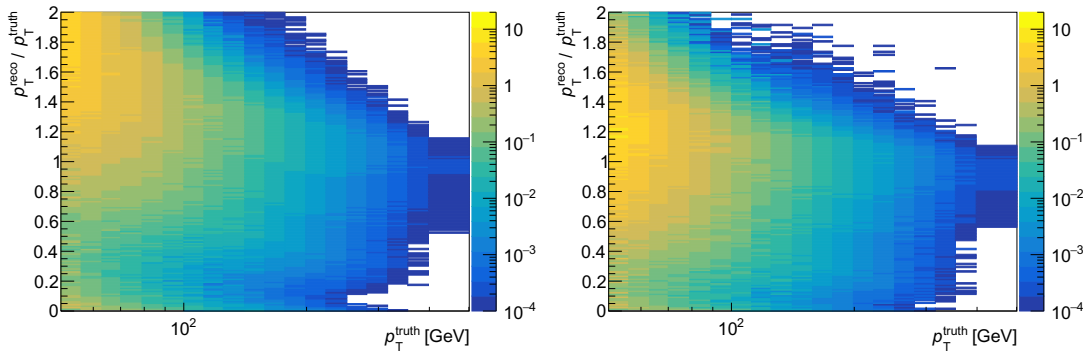

(a) PbPb 0 – 10%

(b) PbPb 20 – 30%

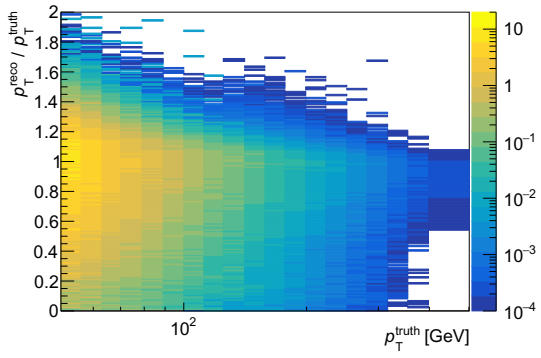

(c) PbPb 40 – 50%

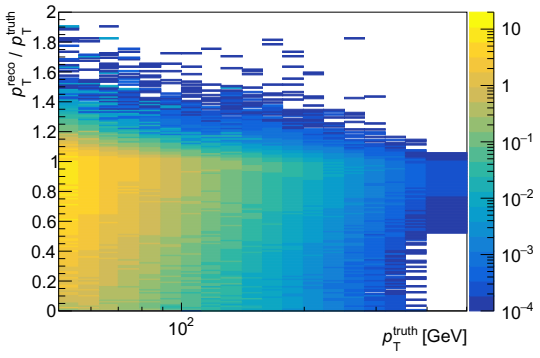

(d) PbPb 60 – 70%

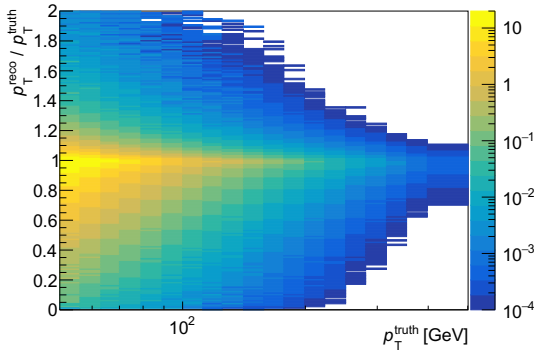

(e) pp

Figure 5.10: Correlation plots $p_{\mathrm{T}}^{\mathrm{reco}}/p_{\mathrm{T}}^{\mathrm{truth}}$ vs $p_{\mathrm{T}}^{\mathrm{truth}}$ of MC track jets with $R = 0.6$, $p_{\mathrm{T}}^{\mathrm{cut}} = 1$ GeV, and pseudorapidity $|\eta^{\mathrm{jet}}| < 1.9$. The plots in the first two rows correspond to PbPb collisions for various centrality bins, the bottom plot corresponds to pp collisions.

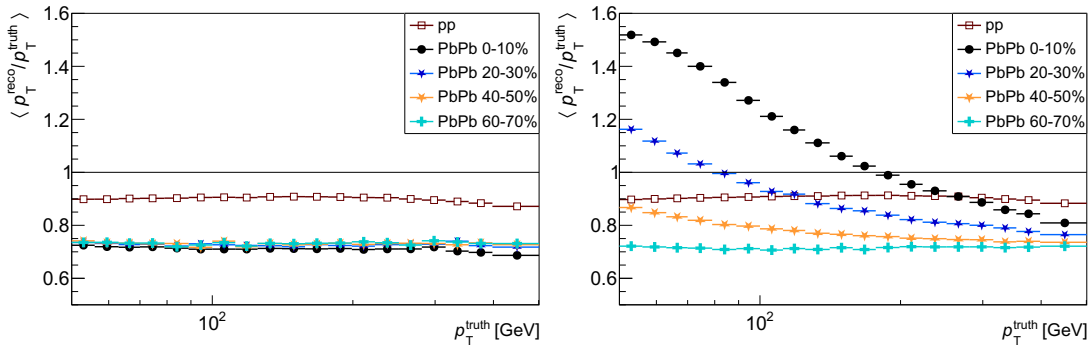

(a) $R = 0.2$, $p_{\mathrm{T}}^{\mathrm{cut}} = 6$ GeV (b) $R = 0.6$, $p_{\mathrm{T}}^{\mathrm{cut}} = 1$ GeV

Figure 5.11: $\left\langle p_{\mathrm{T}}^{\mathrm{reco}}/p_{\mathrm{T}}^{\mathrm{truth}} \right\rangle$ as a function of $p_{\mathrm{T}}^{\mathrm{truth}}$ using MC track jets for pp and PbPb collisions with centrality bins 0 – 10%, 20 – 30%, 40 – 50%, and 60 – 70%. Left: $R = 0.2$ and $p_{\mathrm{T}}^{\mathrm{cut}} = 6$ GeV; right: $R = 0.6$ and $p_{\mathrm{T}}^{\mathrm{cut}} = 1$ GeV. Only statistical errors are presented. The value of 1 is marked by a grey line.

6. Bin-by-bin Unfolding

MC simulations are useful not only for the investigation of jet migration but they can be used also for the correction of jet spectra constructed from experimental data. Within this thesis, a simple bin-by-bin unfolding of experimental data is performed. However, this is the very first attempt to correct experimental track-jet spectra which is not so precise. The more precise unfolding would be beyond the scope of the thesis.

The bin-by-bin unfolding is performed as follows. First of all, the ratios $N_{\mathrm{reco}}/N_{\mathrm{truth}}$ of the reconstructed track-jet spectra and the truth track-jet spectra within MC are made. In this case, the reconstructed jets are not matched to the truth ones. Two examples of such ratios are displayed (again with the same parameter selection as in the previous chapter) in Fig. 6.1. Then, the experimental track-jet spectra are divided by the ratios with compatible R and $p_{\mathrm{T}}^{\mathrm{cut}}$. Such correction accounts for the effects of momentum scale, resolution, UE contribution, fakes, and efficiency. Finally, the corrected R_{AA} (Fig. 6.2) and double R_{AA} ratios (Fig. 6.3) are made from the corrected track-jet spectra.

In this paragraph, the above-mentioned figures are discussed. It seems that the corrections are much larger for the spectra of jets with $R = 0.6$ and $p_{\mathrm{T}}^{\mathrm{cut}} = 1$ GeV than those with $R = 0.2$ and $p_{\mathrm{T}}^{\mathrm{cut}} = 6$ GeV, especially for central events (0–10% and 20–30%), where the values of $N_{\mathrm{reco}}/N_{\mathrm{truth}}$ are in the order of hundreds or thousands as a consequence of a significant background contribution to the spectra (Fig. 6.1). This is expected as all the effects mentioned above are more pronounced for larger jets and lower $p_{\mathrm{T}}^{\mathrm{cut}}$. As to R_{AA} (Fig. 6.2), the plots with corrected spectra do not differ so much from each other than those made from raw spectra. For $R = 0.6$ and $p_{\mathrm{T}}^{\mathrm{cut}} = 1$ GeV, the correction shifted R_{AA} to a reasonable order, and for $R = 0.2$ and $p_{\mathrm{T}}^{\mathrm{cut}} = 6$ GeV, the correction increased the differences in R_{AA} between the individual centralities. As to double R_{AA} ratios (Fig. 6.3), the correction again shifted the values for $p_{\mathrm{T}}^{\mathrm{cut}} = 1$ GeV and 2 GeV to the reasonable order (these dependencies are missing in the figures corresponding to raw spectra since the values would be in the order of hundreds), but their shapes seem to be also unphysical. As mentioned above, this simple bin-by-bin unfolding has very bound limits for corrections and the uncertainty of the result is significant.

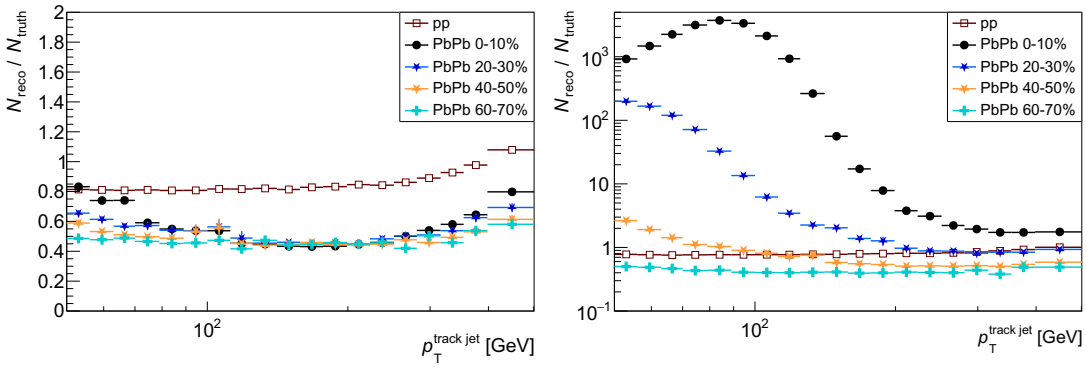

Figure 6.1: Ratios $N_{\mathrm{reco}}/N_{\mathrm{truth}}$ of MC track jets for pp and PbPb collisions with centrality bins 0 – 10%, 20 – 30%, 40 – 50%, and 60 – 70%. Left: $R = 0.2$ and $p_{\mathrm{T}}^{\mathrm{cut}} = 6$ GeV; right: $R = 0.6$ and $p_{\mathrm{T}}^{\mathrm{cut}} = 1$ GeV. Only statistical errors are presented.

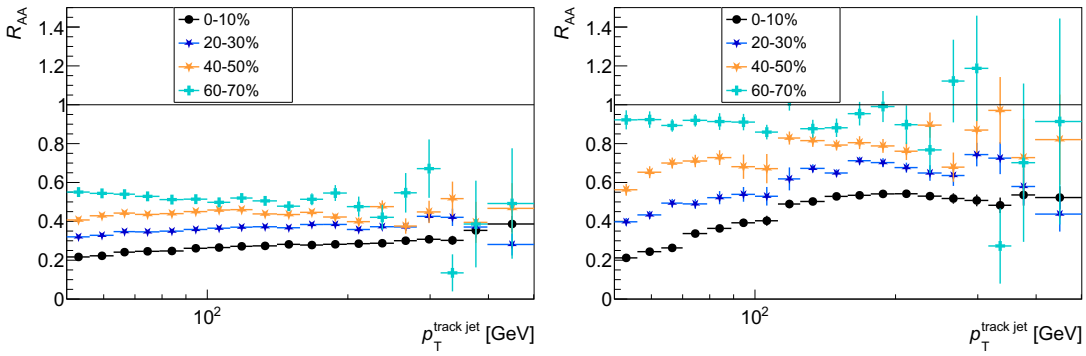

(a) raw, $R = 0.2$, $p_{\mathrm{T}}^{\mathrm{cut}} = 6$ GeV

(b) corrected, $R = 0.2$, $p_{\mathrm{T}}^{\mathrm{cut}} = 6$ GeV

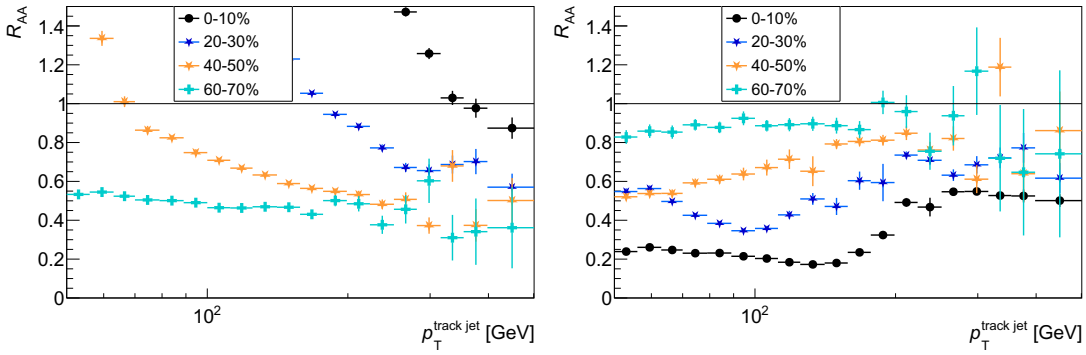

(c) raw, $R = 0.6$, $p_{\mathrm{T}}^{\mathrm{cut}} = 1$ GeV

(d) corrected, $R = 0.6$, $p_{\mathrm{T}}^{\mathrm{cut}} = 1$ GeV

Figure 6.2: Comparison of R_{AA} plots made from raw (first column) and corrected (second column) experimental-jet spectra with $|\eta^{\mathrm{jet}}| < 1.9$. The first row corresponds to jets with $R = 0.2$ and $p_{\mathrm{T}}^{\mathrm{cut}} = 6$ GeV, the second row corresponds to jets with $R = 0.6$ and $p_{\mathrm{T}}^{\mathrm{cut}} = 1$ GeV. Only statistical errors are presented. The value of 1 is marked by a grey line.

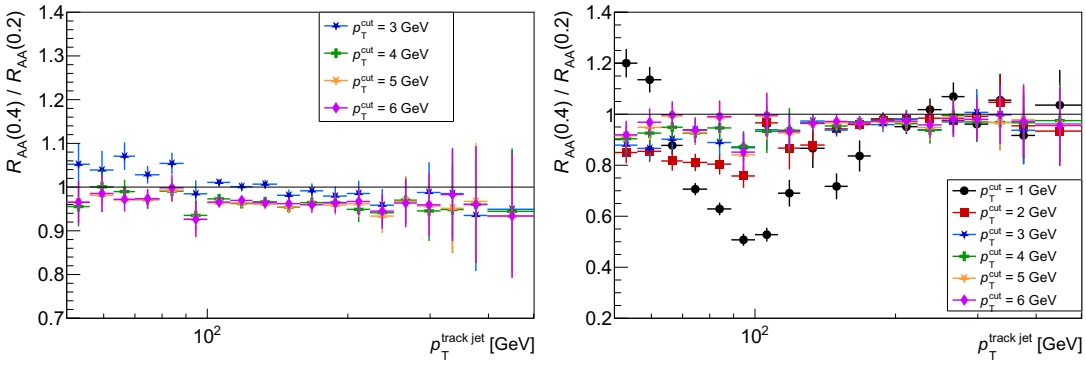

(a) raw, $R_{\mathrm{AA}}(0.4)/R_{\mathrm{AA}}(0.2)$

(b) corrected, $R_{\mathrm{AA}}(0.4)/R_{\mathrm{AA}}(0.2)$

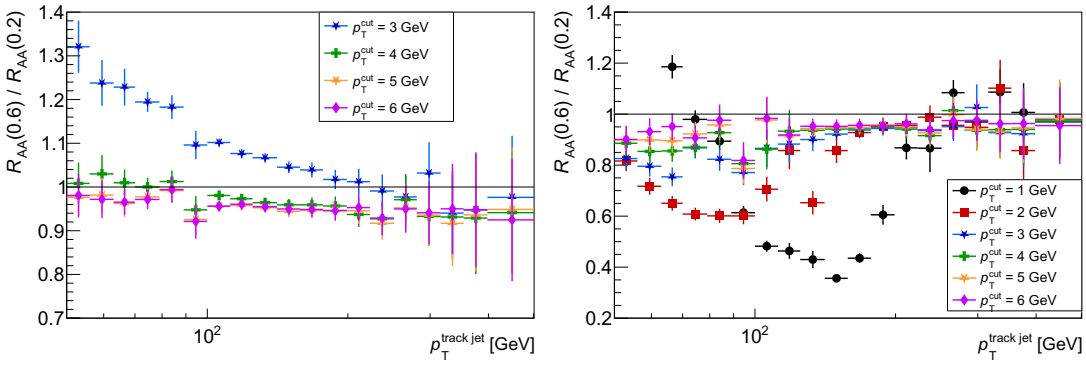

(c) raw, $R_{\mathrm{AA}}(0.6)/R_{\mathrm{AA}}(0.2)$

(d) corrected, $R_{\mathrm{AA}}(0.6)/R_{\mathrm{AA}}(0.2)$

Figure 6.3: Double R_{AA} ratios made from raw (first column) and corrected (second column) experimental-jet spectra from central PbPb collisions (0–10%) with $|\eta^{\mathrm{jet}}| < 1.9$ and various $p_{\mathrm{T}}^{\mathrm{cut}}$. Only statistical errors are presented. The value of 1 is marked by a grey line.

7. Iterative Constituent Subtraction

In the above analysis, the background was treated using a high $p_{\mathrm{T}}^{\mathrm{cut}}$. However, the signal tracks are removed along with the background. Therefore, a more appropriate choice is to use a method for background subtraction without or with a small $p_{\mathrm{T}}^{\mathrm{cut}}$. Within this thesis, the iterative constituent subtraction method (ICS) is used. The text in this chapter is inspired by [29].

7.1 Description of the ICS

The ICS method is based on the creation of so-called ghosts that correct p_{T} of particles before the clustering, and this should lead to background elimination. The ghosts are considered to be infinitely soft massless particles that cover uniformly the $y - \phi$ space within the detector acceptance ($|\eta| < 2.5$) with the density of background transverse momentum ρ. The background density ρ can be estimated using one of the methods described here [34]. In general, ρ can be a function of other variables, in most cases of rapidity y.

Before the iteration description, here is the list of free parameters:

- *Number of iterations* N_{iter}.
- *Ghost area* A_{g}. This is a fixed area that each ghost covers and is used to determine the ghost's transverse momentum $p_{\mathrm{T}}^{\mathrm{g}} = \rho A_{\mathrm{g}}$.
- *Maximal particle-ghost distance* ΔR_{max}. It controls a condition for the termination of the background removal procedure. ΔR_{max} can be different for each iteration.
- *Momentum weight* α. This parameter is included in the determination of the distance measure $D_{i,k}$ between the i-th particle and k-th ghost defined as

$$D_{i,k} = p_{\mathrm{T},i}^{\alpha} \Delta R_{i,k} \tag{7.1}$$

  where $\Delta R_{i,k} = \sqrt{(y_i - y_k^{\mathrm{g}})^2 + (\phi_i - \phi_k^{\mathrm{g}})^2}$
- *Ghost removal.* It can be either turned on or off. If turned on, the algorithm does not use ghosts in the following iterations that were not fully subtracted in the previous iteration.

The algorithm follows these steps:

1. Background momentum density ρ is calculated and ghosts with $p_{\mathrm{T}}^{\mathrm{g}}$ are created.

2. Event-wide CS correction is performed. This is an iterative procedure for background removal. First, a list of distance measures $D_{i,k}$ is created and sorted from the lowest to the highest values. The procedure starts with the particle-ghost pair with the lowest $D_{i,k}$ and the following manipulations are done:

$$\begin{aligned} \text{If } p_{\mathrm{T},i} > p^{\mathrm{g}}_{\mathrm{T},k}: \quad & p_{\mathrm{T},i} \to p_{\mathrm{T},i} - p^{\mathrm{g}}_{\mathrm{T},k}, \\ & p^{\mathrm{g}}_{\mathrm{T},k} \to 0; \\ \text{otherwise:} \quad & p_{\mathrm{T},i} \to 0, \\ & p^{\mathrm{g}}_{\mathrm{T},k} \to p^{\mathrm{g}}_{\mathrm{T},k} - p_{\mathrm{T},i}. \end{aligned} \tag{7.2}$$

   The procedure iterates as long as $\Delta R_{i,k} < \Delta R_{\mathrm{max}}$.

3. A scalar p_{T} sum of the input ghosts $p_{\mathrm{T}}^{\mathrm{input}}$ and of the output ghosts $p_{\mathrm{T}}^{\mathrm{output}}$ is calculated. The input ghosts are those present in the event before the CS correction, and the output ghosts are those remaining after the CS correction. The input ghosts are then updated by scaling their p_{T} by a factor $p_{\mathrm{T}}^{\mathrm{output}}/p_{\mathrm{T}}^{\mathrm{input}}$.

4. The next iteration is performed – the algorithm moves to step 2 with the updated ghosts and generally different values of ΔR_{max}. A number of iterations is given by N_{iter}.

An example of how the ICS method works is given in Fig. 7.1.

7.2 Parameter Discussion and Results

Within this thesis, the ICS is applied to MC data for an option $R = 0.6$ and $p_{\mathrm{T}}^{\mathrm{cut}} = 1$ GeV, since this is the case with the strongest background and for MC it is possible to construct migration matrices and correlation plots $p_{\mathrm{T}}^{\mathrm{reco}}/p_{\mathrm{T}}^{\mathrm{truth}}$ vs $p_{\mathrm{T}}^{\mathrm{truth}}$.

A challenging task is to set free parameters of the ICS (listed in Sec. 7.1). Optimization of the parameters for data from pp collisions is discussed in [29], which can be of course different for the case of PbPb collisions since the nature of the background is different. Despite this fact, the setting of the parameters was inspired by [29]. The number of iterations N_{iter} is recommended to be set to 2 since more iterations do not bring significant improvement.

In general, ghost area A_{g} should be $A_{\mathrm{g}} \leq 0.01$. Ghost area determines the density of ghosts, so with decreasing A_{g} the density of ghosts increases and the resolution is better, but the computational time is much larger.

The parameter ΔR_{max} determines the maximal distance between particles and ghosts that can be combined. By setting finite ΔR_{max} one avoids combining particles with ghosts far from each other. An optimal value of ΔR_{max} can depend on the jet definition and the detector granularity. As mentioned in Sec. 7.1, ΔR_{max} can be different for each iteration (ΔR_{max1}, ΔR_{max2}).

As to parameter α, it can be beneficial to set $\alpha > 0$, since the particle-ghost pairs with lower p_{T} of particles (background is formed by soft particles) are

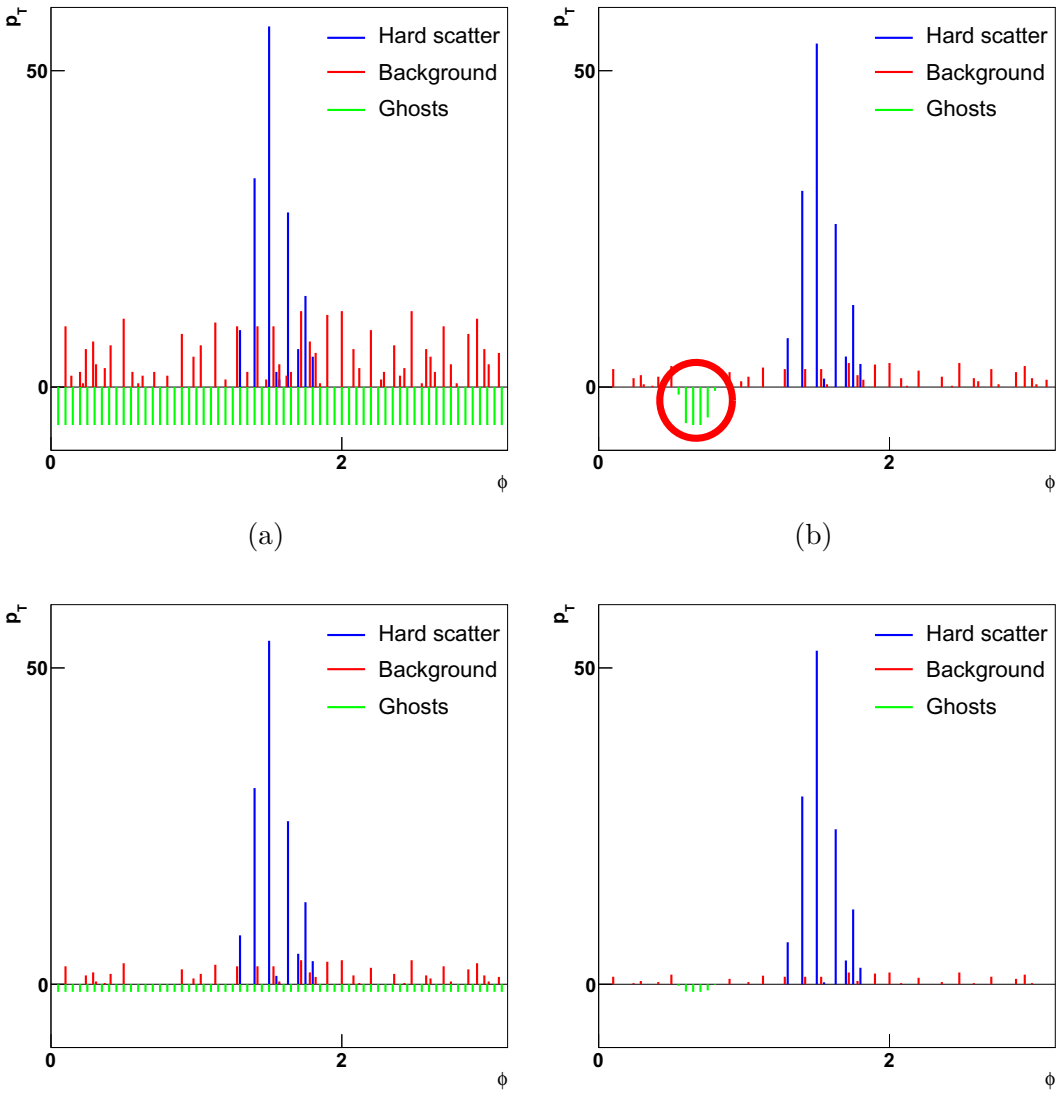

Figure 7.1: An example of 2-iterative ICS correction. Subfigure (a) illustrates an event before the first iteration with hard scatters, background, and ghosts. After the first iteration, some ghosts can remain in the event (subfigure (b)), and their total p_{T} is then redistributed uniformly in the $y - \phi$ space (subfigure (c)). Subfigure (d) shows a background-corrected event after the second iteration. Taken from [29].

prioritized (see 7.2). An optimal value of α depends on ΔR_{max}, $p_{\text{T}}^{\text{cut}}$, jet radius R, and granularity of the detector.

The last free parameter is ghost removal. It affects subtraction in the cases when $\Delta R_{\text{max1}} > \Delta R_{\text{max2}}$. The impact of ghost removal can depend on the background properties. When ρ is correlated/anti-correlated in close-by regions in the $y - \phi$ space, then it may be useful to turn the ghost removal on/off, respectively.

Within this thesis, four configurations of parameters are used, which are listed in Tab. 7.1. The varied parameters are just α and ghost removal. R_{AA} of MC track jets for the various parameter configurations is shown in Fig. 7.2. Indeed, it seems that the ICS works since the divergencies at small p_{T} are reduced (compare with Fig. 5.4a). It seems that the configuration #4 ($\alpha = 0$ and ghost removal on) reduces the divergencies mostly. However, it is difficult to say which configuration is optimal. Furthermore, the other parameters can be also varied.

In PbPb collisions, it is needed to take into account the effects of flow on the UE. The flow originates from the azimuthal anisotropy of the spatial overlap of the colliding nuclei, which results in the azimuthal momentum anisotropy of particle emission. It can be expanded to the Fourier series [35]. Within the ICS, we take into account just coefficients v_2 and v_3.

Consequently, the migration matrices and correlation plots $p_{\text{T}}^{\text{reco}}/p_{\text{T}}^{\text{truth}}$ vs $p_{\text{T}}^{\text{truth}}$ were constructed for all the configurations. Since there are almost no visible differences in the migration matrices and the correlation plots between different configurations, just one set of plots (config. #4) is presented in the thesis (Figures 7.3 and 7.4). The migration matrices (Fig. 7.3) look more physical than in the case of no subtraction (Fig. 5.8). The jet momentum scale (Fig. 7.5) looks similar for all the configurations and the average value is about 0.7 in PbPb collisions and 0.9 in pp collisions (similar as in Fig. 5.11a), which is the result of imperfect tracking efficiency.

Config.	N_{iter}	A_{g}	ΔR_{max1}	ΔR_{max2}	α	Ghost removal
#1	2	0.01	0.2	0.1	1	OFF
#2	2	0.01	0.2	0.1	1	ON
#3	2	0.01	0.2	0.1	0	OFF
#4	2	0.01	0.2	0.1	0	ON

Table 7.1: Table of parameter configurations within the ICS method.

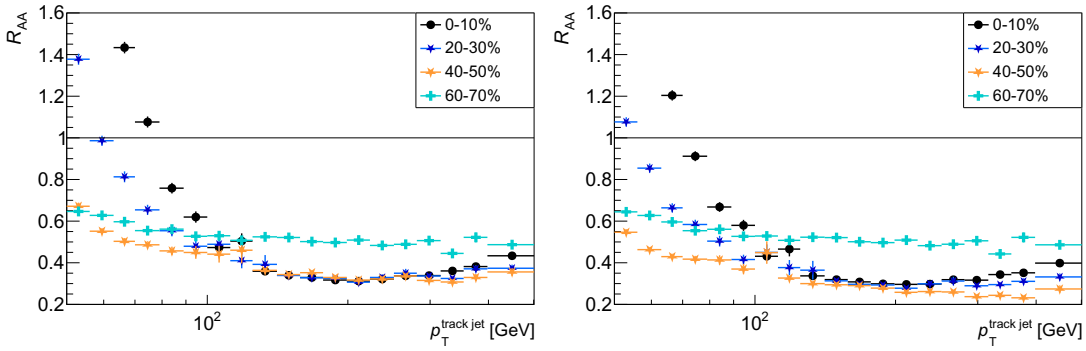

(a) Config. #1

(b) Config. #2

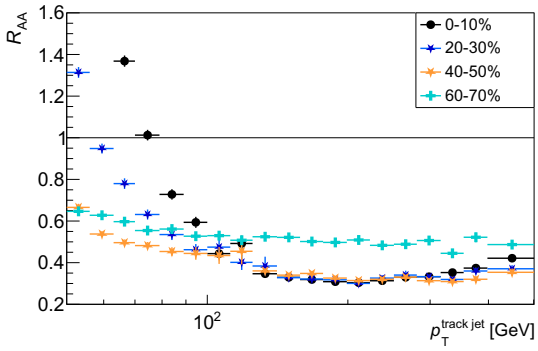

(c) Config. #3

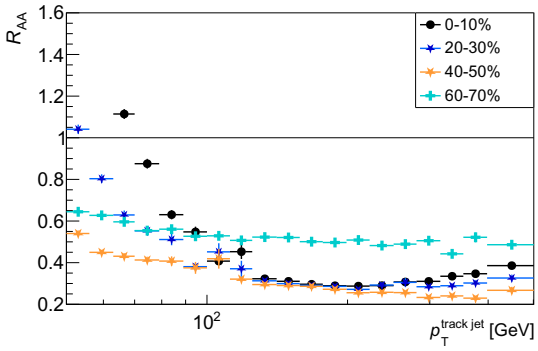

(d) Config. #4

Figure 7.2: R_{AA} of MC track jets in PbPb collisions with centrality bins 0 – 10%, 20 – 30%, 40 – 50%, and 60 – 70% after the ICS application for 4 various parameter configurations. Jet radius is $R = 0.6$, $p_{\mathrm{T}}^{\mathrm{cut}} = 1$ GeV, and pseudorapidity $|\eta^{\mathrm{jet}}| < 1.9$. Only statistical errors are presented. The value of 1 is marked by a grey line.

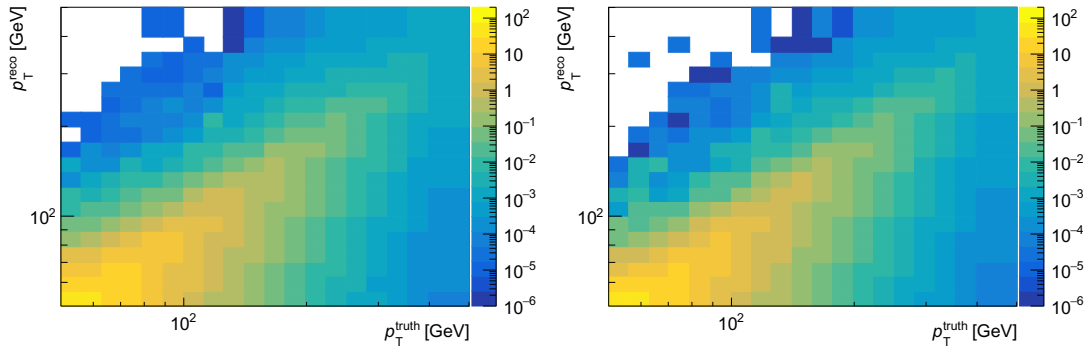

(a) PbPb 0 – 10%

(b) PbPb 20 – 30%

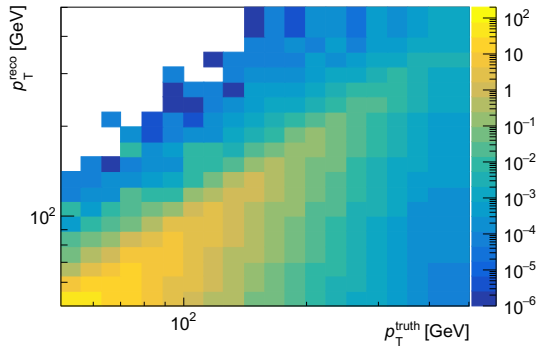

(c) PbPb 40 – 50%

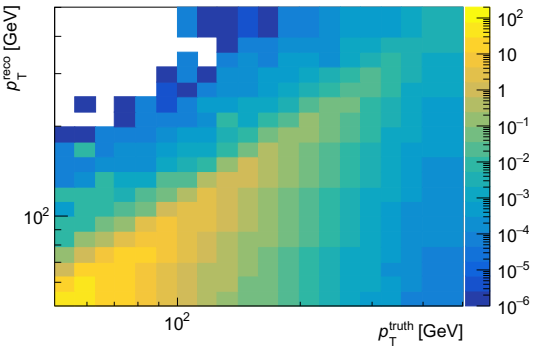

(d) PbPb 60 – 70%

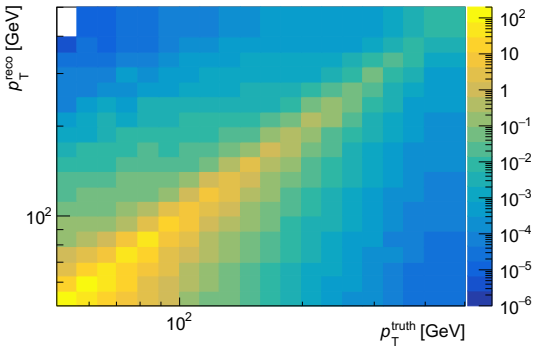

(e) pp

Figure 7.3: Migration matrices for MC track jets with $R = 0.6$, $p_{\mathrm{T}}^{\mathrm{cut}} = 1$ GeV, and pseudorapidity $|\eta^{\mathrm{jet}}| < 1.9$. The plots in the first two rows correspond to PbPb collisions for various centrality bins after the ICS application with configuration #4, the bottom plot corresponds to pp collisions (without the ICS).

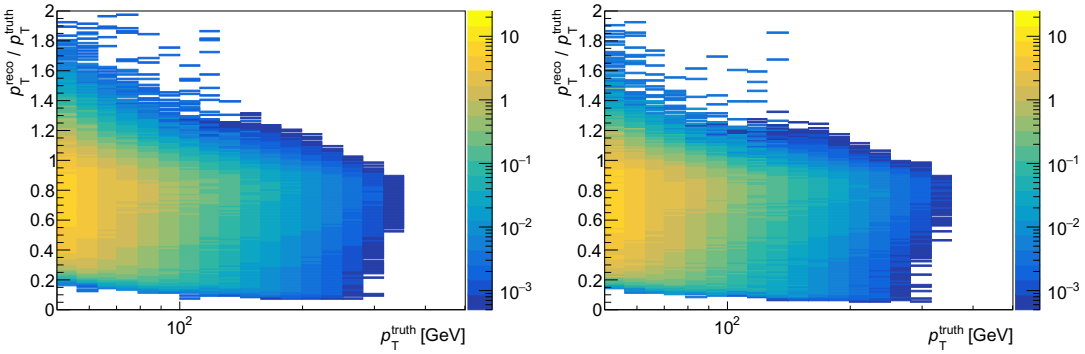

(a) PbPb 0 – 10%

(b) PbPb 20 – 30%

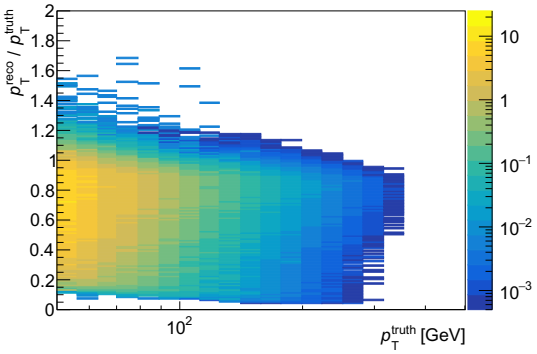

(c) PbPb 40 – 50%

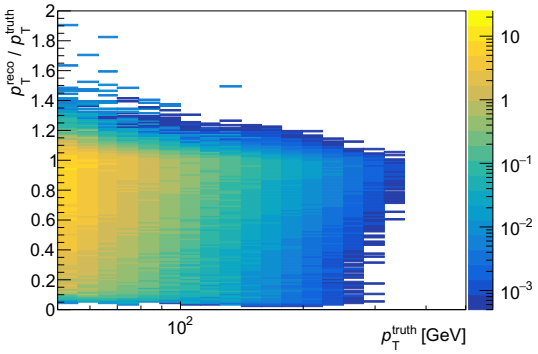

(d) PbPb 60 – 70%

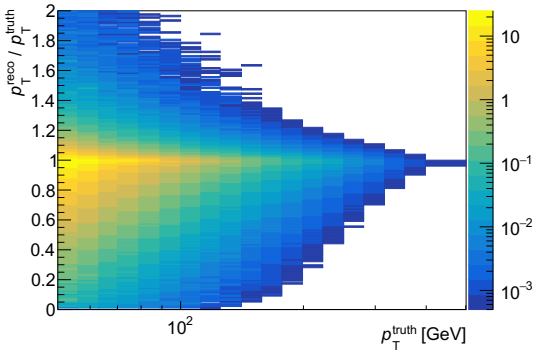

(e) pp

Figure 7.4: Correlation plots $p_{\mathrm{T}}^{\mathrm{reco}}/p_{\mathrm{T}}^{\mathrm{truth}}$ vs $p_{\mathrm{T}}^{\mathrm{truth}}$ of MC track jets with $R = 0.6$, $p_{\mathrm{T}}^{\mathrm{cut}} = 1$ GeV, and pseudorapidity $|\eta^{\mathrm{jet}}| < 1.9$. The plots in the first two rows correspond to PbPb collisions for various centrality bins after the ICS application with configuration #4, the bottom plot corresponds to pp collisions (without the ICS).

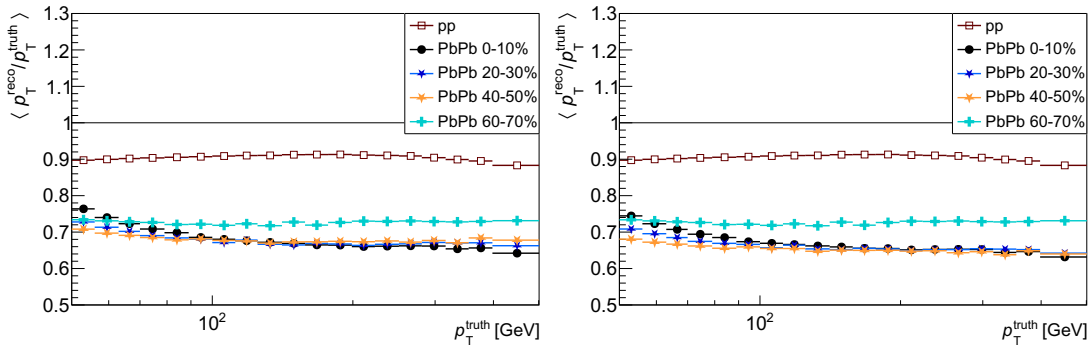

(a) Config. #1

(b) Config. #2

(c) Config. #3

(d) Config. #4

Figure 7.5: $\left\langle p_{\mathrm{T}}^{\mathrm{reco}}/p_{\mathrm{T}}^{\mathrm{truth}} \right\rangle$ as a function of $p_{\mathrm{T}}^{\mathrm{truth}}$ using MC track jets for pp and PbPb collisions with centrality bins 0 – 10%, 20 – 30%, 40 – 50%, and 60 – 70% after the ICS application for various parameter configurations. Jet radius is $R = 0.6$, $p_{\mathrm{T}}^{\mathrm{cut}} = 1$ GeV, and pseudorapidity $|\eta^{\mathrm{jet}}| < 1.9$. Only statistical errors are presented. The value of 1 is marked by a grey line.

Conclusion

The motivation for the thesis was the inconsistency between the results from the jet-suppression measurement in dependence on jet radius R between the experiments ATLAS, ALICE, and CMS. A crucial difference between the measurements was that ALICE analyzed track jets, while the other experiments analyzed calorimetric jets. For this reason, we constructed and analyzed track jets from ATLAS data to mitigate this difference. It was the first time that track jets were analyzed in detail within the ATLAS experiment in PbPb collisions.

We investigated the dependence of track-jet R_{AA} on jet radius R and the minimum transverse momentum of the clustered tracks $p_{\mathrm{T}}^{\mathrm{cut}}$. Setting a higher value of $p_{\mathrm{T}}^{\mathrm{cut}}$ eliminated the majority of the background dominated by soft particles. On the other hand, low-p_{T} signals were also discarded, and therefore, physics was biased. In general, the higher R and smaller $p_{\mathrm{T}}^{\mathrm{cut}}$, the more the background is clustered. For raw data and $p_{\mathrm{T}}^{\mathrm{cut}} \geq 4$ GeV, the values of double R_{AA} ratios $R_{\mathrm{AA}}(0.4)/R_{\mathrm{AA}}(0.2)$ and $R_{\mathrm{AA}}(0.6)/R_{\mathrm{AA}}(0.2)$ in central events are approximately equal to 1. If $p_{\mathrm{T}}^{\mathrm{cut}} = 3$ GeV, the background starts to be clustered, especially for $R = 0.6$, and the values of $R_{\mathrm{AA}}(0.6)/R_{\mathrm{AA}}(0.2)$ increase with decreasing $p_{\mathrm{T}}^{\mathrm{jet}}$ and are slightly above 1. For lower values of $p_{\mathrm{T}}^{\mathrm{cut}}$, the values of double R_{AA} ratios diverge at small $p_{\mathrm{T}}^{\mathrm{jet}}$.

MC simulations were analyzed to investigate jet performance as a consequence of imperfect tracking efficiency, momentum resolution of the detector, and background. Subsequently, the raw experimental data were corrected for these effects by performing a simple bin-by-bin unfolding. However, this unfolding is very limited since it corrects spectra for a lot of effects simultaneously. As a result, the unfolding shifted the values of double R_{AA} ratios for $p_{\mathrm{T}}^{\mathrm{cut}} = 1$ GeV and 2 GeV to a reasonable order, but the shapes seem to be still affected by various effects.

Additionally, the ICS method was used to remove the background and improve jet reconstruction performance. It was applied to MC track jets with $R = 0.6$ and $p_{\mathrm{T}}^{\mathrm{cut}} = 1$ GeV. In this configuration, the background is the most significant. The ICS was performed for four parameter configurations (free parameters within the ICS) and it seems that the method reduced the UE significantly. However, finding an optimal parameter configuration is a challenging task and would require additional investigation.

To conclude, the results from this thesis are not sufficient to clarify the inconsistency between the results from the experiments, but they provide a certain degree of understanding of track-jet suppression in the QGP. Further analysis should include better unfolding and parameter tuning within the ICS.

Bibliography

[1] Leticia Cunqueiro and Anne M. Sickles. Studying the QGP with Jets at the LHC and RHIC. *Progress in Particle and Nuclear Physics*, 124:103940, 2022.

[2] ATLAS Collaboration. Measurement of the jet radius and transverse momentum dependence of inclusive jet suppression in lead-lead collisions at $\sqrt{s_{\mathrm{NN}}} = 2.76\,\mathrm{TeV}$ with the ATLAS detector. *Physics Letters B*, 719(4–5):220–241, February 2013.

[3] ATLAS Collaboration. Measurement of suppression of large-radius jets and its dependence on substructure in Pb+Pb collisions at $\sqrt{s_{\mathrm{NN}}} = 5.02\,\mathrm{TeV}$ with the ATLAS detector. *Phys. Rev. Lett.*, 131(2023):172301, November 2023.

[4] ALICE Collaboration. Measurement of the radius dependence of charged-particle jet suppression in Pb-Pb collisions at $\sqrt{s_{\mathrm{NN}}} = 5.02\,\mathrm{TeV}$. *Phys. Rev. Lett.*, 849(2024):138412, January 2024.

[5] CMS Collaboration. First measurement of large area jet transverse momentum spectra in heavy-ion collisions. *JHEP*, 05(2021):284, February 2021.

[6] Lyndon Evans and Philip Bryant. LHC Machine. *Journal of Instrumentation*, 3(08):S08001, August 2008.

[7] Map of the cern accelerator complex, May 2011. Available at: https://commons.wikimedia.org/wiki/File:Cern-accelerator-complex-fr.svg. Accessed on 25. 02. 2024.

[8] ATLAS Collaboration. The ATLAS Experiment. Available at: https://atlas.cern/about. Accessed on 25. 02. 2024.

[9] Izaak Neutelings. CMS coordinate system. Available at: https://tikz.net/axis3d_cms/. Accessed on 25. 02. 2024.

[10] ATLAS Collaboration. Detector & Technology. Available at: https://atlas.cern/Discover/Detector. Accessed on 01. 03. 2024.

[11] ATLAS Collaboration. Trigger Menu in 2018. Technical report, CERN, Geneva, October 2019. Available at: https://cds.cern.ch/record/2693402.

[12] Jiří Chýla. Quarks, partons and Quantum Chromodynamics. Available at: https://www.fzu.cz/~chyla/lectures/text.pdf, 2004.

[13] Michael L. Miller, Klaus Reygers, Stephen J. Sanders and Peter Steinberg. Glauber Modeling in High-Energy Nuclear Collisions. *Annual Review of Nuclear and Particle Science*, 57:205–243, November 2007.

[14] LHCb collaboration. Centrality determination in heavy-ion collisions with the LHCb detector. *JINST*, 17(05):P05009, 2022.

[15] ATLAS Collaboration. Measurement of the azimuthal anisotropy of charged particles produced in $\sqrt{s_{\mathrm{NN}}} = 5.02\,\mathrm{TeV}$ Pb+Pb collisions with the ATLAS detector. *The European Physical Journal C*, 78(12), December 2018.

[16] Maxim Chernodub. Background magnetic field stabilizes QCD string against breaking. January 2010.

[17] Ryan Atkin. Review of jet reconstruction algorithms. *Journal of Physics: Conference Series*, 645(1):012008, September 2015.

[18] Matteo Cacciari, Gavin P. Salam, and Gregory Soyez. The anti-k_t jet clustering algorithm. *Journal of High Energy Physics*, 2008(04):063–063, April 2008.

[19] Dominik Soliman. *Hunting the ppK-: A kinematic refit for the exclusive analysis of the reaction* $pp \to pK + \Lambda$. PhD thesis, May 2012.

[20] CERN. Heavy ions and quark-gluon plasma. Available at: `https://home.cern/science/physics/heavy-ions-and-quark-gluon-plasma`. Accessed on 01. 03. 2024.

[21] Martin Rybář. *Study of jets in p+p and Pb+Pb collisions at LHC*. PhD thesis, Charles Universuty, Prague, 2015.

[22] ATLAS Collaboration. Measurement of angular and momentum distributions of charged particles within and around jets in PbPb and pp collisions at $\sqrt{s_{\mathrm{NN}}} = 5.02\,\mathrm{TeV}$ with the ATLAS detector. *Physical Review C*, 100(6), December 2019.

[23] Daniel Pablos. Jet Suppression From a Small to Intermediate to Large Radius. *Phys. Rev. Lett.*, 124:052301, February 2020.

[24] Yayun He, Shanshan Cao, Wei Chen, Tan Luo, Long-Gang Pang, and Xin-Nian Wang. Interplaying mechanisms behind single inclusive jet suppression in heavy-ion collisions. *Phys. Rev. C*, 99:054911, May 2019.

[25] Björn Schenke, Charles Gale, and Sangyong Jeon. MARTINI: An event generator for relativistic heavy-ion collisions. *Phys. Rev. C*, 80:054913, November 2009.

[26] ATLAS Collaboration. Measurement of the nuclear modification factor for inclusive jets in Pb+Pb collisions at $\sqrt{s_{\mathrm{NN}}} = 5.02\,\mathrm{TeV}$ with the ATLAS detector. *Physics Letters B*, 790:108–128, March 2019.

[27] ATLAS Collaboration. Measurement of jet fragmentation in Pb+Pb and pp collisions at $\sqrt{s_{\mathrm{NN}}} = 5.02\,\mathrm{TeV}$ with the ATLAS detector. *Physical Review C*, 98(2), August 2018.

[28] CMS Collaboration. Modification of jet shapes in PbPb collisions at $\sqrt{s_{\mathrm{NN}}} = 2.76\,\mathrm{TeV}$. *Physics Letters B*, 730:243–263, March 2014.

[29] P. Berta, L. Masetti, D.W. Miller, and M. Spousta. Pileup and underlying event mitigation with iterative constituent subtraction. *Journal of High Energy Physics*, 2019(8), August 2019.

[30] Tanner Mengel, Patrick Steffanic, Charles Hughes, Antonio Carlos Oliveira da Silva, and Christine Nattrass. Interpretable machine learning methods applied to jet background subtraction in heavy-ion collisions. *Physical Review C*, 108(2), August 2023.

[31] Matteo Cacciari, Gavin P Salam, and Gregory Soyez. The catchment area of jets. *Journal of High Energy Physics*, 2008(04):005–005, April 2008.

[32] Rüdiger Haake and Constantin Loizides. Machine-learning-based jet momentum reconstruction in heavy-ion collisions. *Physical Review C*, 99(6), June 2019.

[33] Torbjörn Sjöstrand, Stephen Mrenna, and Peter Skands. PYTHIA 6.4 physics and manual. *Journal of High Energy Physics*, 2006(05):026–026, May 2006.

[34] Matteo Cacciari, Gavin P. Salam, and Gregory Soyez. FastJet user manual: (for version 3.0.2). *The European Physical Journal C*, 72(3), March 2012.

[35] Raimond Snellings. Elliptic flow: a brief review. *New Journal of Physics*, 13(5):055008, May 2011.

A. Appendix

A.1 Run Numbers of ATLAS Data

- 2017 pp data: 341184, 341123, 341027, 340973, 340925, 340910, 340850, 340849, 340814, 340718, 340697, 340683, 340644
- 2018 PbPb data: 365502, 365512, 365573, 365602, 365627, 365678, 365681, 365709, 365752, 365834, 365914, 365932, 366011, 366029, 366092, 366142, 366268, 366337, 366383, 366413, 366476, 366526, 366528, 366627, 366691, 366754, 366805, 366860, 366878, 366919, 366931, 366994, 367023, 367099, 367134, 367165, 367170, 367233, 367273, 367318, 367321, 367363, 367364, 367365, 367384